

Atlantic water inflow into the Arctic Ocean: studies of pathways, transport and mixing processes using observations from ships and autonomous underwater vehicles

Eivind Hugaas Kolås

Thesis for the degree of Philosophiae Doctor (PhD)
University of Bergen, Norway
2024

UNIVERSITY OF BERGEN



Atlantic water inflow into the Arctic Ocean: studies of pathways, transport and mixing processes using observations from ships and autonomous underwater vehicles

Eivind Hugaas Kolås



Thesis for the degree of Philosophiae Doctor (PhD)
at the University of Bergen

Date of defense: 23.01.2024

© Copyright Eivind Hugaas Kolås

The material in this publication is covered by the provisions of the Copyright Act.

Year: 2024

Title: Atlantic water inflow into the Arctic Ocean: studies of pathways, transport and mixing processes using observations from ships and autonomous underwater vehicles

Name: Eivind Hugaas Kolås

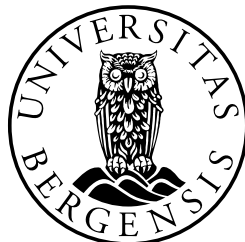
Print: Skipnes Kommunikasjon / University of Bergen

Scientific environment

This study was carried out at the Geophysical Institute, University of Bergen (UiB), where I have been part of the Physical Oceanography group. The research contributed to the activities at the Bjerknes Centre for Climate Research, where I was affiliated with the Polar Research group. My participation in the Research School on Changing Climates in the Coupled Earth System (CHESS) provided access to a multitude of valuable courses. Over the course of my doctoral studies, I embarked on numerous scientific expeditions to the Arctic region around Svalbard. During these expeditions, I collaborated closely with fellow researchers in gathering the data presented herein.

My PhD research is an integral component of the Nansen Legacy project, which generously facilitated research visits at the University Centre at Svalbard, NTNU in Trondheim, and the University of Tromsø. Furthermore, the Nansen Legacy project offered financial support for attending various scientific conferences in Europe and the USA. During my time at GFI, I had the privilege of serving as a teaching assistant for the Polar Oceanography course throughout my PhD journey. Additionally, I occasionally contributed to the Ocean Turbulence course. I also received training and actively participated in the ocean glider piloting team within the Norwegian National Facility for Ocean Gliders (NorGliders), consistently striving to ensure the safe return of our autonomous underwater vehicles. Lastly, I participated in various outreach activities: I have given various lectures and presented my research on behalf of the Centre for Science Education at UiB, I have written a popular science article published at forskersonen.no, and I competed at the annual Forsker Grand Prix during fall 2022 on communicating my PhD research.

the
Nansen
LEGACY



Research school on changing climates in the coupled earth system

Acknowledgements

Embarking on this academic journey has been a transformative experience, and I am deeply grateful to the many individuals and institutions that have supported and enriched my pursuit of knowledge.

First and foremost, I extend my sincere appreciation to my main supervisor, Ilker Fer. Your unwavering, direct guidance, thorough feedback at any time of day (or night), scholarly insight, enthusiasm and encouragement have guided me through the most intricate work I have ever done. Your mentorship has been invaluable, shaping both my academic and personal growth. The opportunities you have provided me with have been nothing short of an amazing adventure. Thank you!

Furthermore, I thank my co-supervisors Frank Nilsen, Martin Ludvigsen and Zoe Koenig. Thank you, Frank, for always being inclusive and making collaboration and conversation easy. Thank you for hosting a workshop at UNIS and thank you for all the time spent together on research cruises in the Arctic. Your easygoing nature has made our collaboration a joy. Thank you, Martin, for your expertise with AUVs. Thank you for hosting a workshop at NTNU where I got to know *Harald*. The time spent with *Harald* has been invaluable in my research (and I'm sorry for participating in almost breaking him). Thank you, Zoe, for your support, and for being my office mate, colleague and friend. Your dedication to science and knowledge in the field has been inspiring and helpful, and I have very much appreciated collaborating with you!

I also extend my gratitude to my office mate and friend, Till Baumann, who convinced me to get a motorcycle. Thank you for all our talks about biking, motorcycling, hiking, non-science related stuff, and science related stuff. Thank you for all our laughs and how you never pass on an opportunity to joke on my behalf!

A special acknowledgment goes to my fellow PhD students Kjersti Kalhagen and Tore Mo-Bjørkelund, both of whom have been invaluable collaborators. Thank you for all the time we spent together on Nansen Legacy cruises and meetings. Thank you for the collective confusion when things have gone awry, the laughs when that is all we can do, and the surprised laughs when things worked as planned after all. Our collaboration has been a constant source of inspiration.

I extend my gratitude to UiB and GFI for laying the necessary framework of this PhD, and for supporting me in my work. A special thanks to the Oceanography group at GFI for valuable discussions and feedback, and to the glider piloting team for keeping the instruments safe and the data coming. Speaking of instrument safety, a special thanks to our technician Helge Bryhni who always have a solution! I would also like to thank the Nansen Legacy project as a whole. Being part of such a grand project has been an incredible experience. I truly feel quite privileged that I got to be part of this project, collaborate with all the remarkable people from different institutes and

participate in many scientific cruises to the Arctic Ocean.

Finally, I extend my sincere gratitude, appreciation and love to my family. To my wife, Margrete Kolås, and my kids Jakob and Matilde, your unwavering support has been the bedrock of my journey. Your encouragement, understanding, and love sustained me during the peaks and valleys of this endeavor. I am profoundly thankful for the sacrifices you made and the encouragement you provided.

This thesis represents a collective achievement, reflecting the collaborative efforts of a diverse and supportive community. I am truly fortunate to have had the privilege of working alongside such remarkable individuals and institutions.

Eivind Hugaas Kolås
Bergen, 01.12.23

"Ja, nå må De skynde Dem, ellers blir det for sent."

Fredrik Hjalmar Johansen

Abstract

The Arctic Ocean plays an important role in the global climate system. Dense water production and sea ice freezing in the Arctic contribute to the functioning of the Atlantic Meridional Overturning Circulation and can affect atmospheric circulation patterns as far south as mid-latitudes. The Atlantic Water (AW) inflow through Fram Strait and Barents Sea into the Arctic Ocean regulates both the dense water production and the sea-ice extent, thus has a key role in the Arctic Ocean and the global climate system as a whole. The transport of AW into the Arctic is the major heat and salt source to the Arctic Ocean, and influences the onset of freezing and the functioning of marine ecosystems. This research contributes to the understanding of the inflow of AW into the Arctic Ocean through Fram Strait and the Barents Sea. The study describes the pathways of the AW inflow, as well as the underlying mechanisms controlling the inflow, processes of heat loss, and mixing with the surrounding waters north of Svalbard and in the northwestern Barents Sea. Essential to this study is data collected by means of autonomous underwater vehicles (AUVs) in challenging Arctic conditions. Data collected from five scientific cruises and 11 AUV missions between 2018 and 2022, resulting in more than 15,000 hydrographic profiles, are collated and presented in the form of four research papers. All data are collected as part of the Nansen Legacy project.

Using detailed observations in the region along the continental slope north of Svalbard between 12°E and 24°E, we describe the hydrographic structure, volume transport, and circulation patterns of the warm AW boundary current. The AW volume transport reaches a maximum of 3.0 ± 0.2 Sv in October, with an intraseasonal variability of 1 Sv ($1 \text{ Sv} = 10^6 \text{ m}^3 \text{ s}^{-1}$). The strength of the AW boundary current is sensitive to the wind stress curl, doubling its volume transport in less than a week when the wind stress curl averaged over the region transitioned from strongly negative to strongly positive values. A previously unknown, deep bottom-intensified current is observed to flow parallel to the boundary current, between the 1,500 and 2,000 m isobaths. Historical data in the region support the presence of the bottom-intensified current.

Taking advantage of the relatively favorable logistical and environmental conditions in the Barents Sea, the follow-up studies concentrated on the northwestern Barents Sea. Targeted measurements from AUVs offer a step change in the spatial and temporal coverage of observations. To exploit the technology, particularly for turbulence measurements, we explored the potential of a thruster-propelled AUV. We instrumented the AUV with a turbulence sensor package, and using this novel setup, we report on the data quality and discuss the limitations of turbulence dissipation rate estimates from shear probes. The AUV mission in the Barents Sea in winter lasted for 5 h, operating at a typical horizontal speed of 1.1 m s^{-1} . The AUV was programmed to find and cross

the maximum along-path thermal gradient at 10, 20 and 30 m depths along 4 km transects. Although the AUV vibrations contaminate the shear probe records, the noise is mitigated by removing vibration-induced components from shear spectra using the accelerometer signal. Dissipation estimates from the AUV show good agreement with nearby vertical microstructure profiles obtained from ship, indicating that the turbulence measurements from the AUV are reliable for this relatively turbulent environment. However, the lowest reliable dissipation rates are limited to $5 \times 10^{-8} \text{ W kg}^{-1}$, making this setup unfit for use in quiescent environments.

Circulation pathways, hydrography and volume transports of Atlantic- and Arctic-origin waters on the northwestern Barents Sea are explored using data from three cruises and nine glider missions conducted between 2019 and 2022, as well as historical data collected between 1950 and 2009. In particular, we focus on the exchange and dynamics across the thermohaline polar front (PF) region. Our observations show that $0.9 \pm 0.1 \text{ Sv}$ of Atlantic-origin water reaches the PF region before splitting into several branches and eventually subducting beneath Polar Water (PW). The amount of Atlantic-origin water stored in the basin north of the PF is controlled by the density difference between AW and PW, and reached a maximum in the 90s when PW was particularly fresh. In the recent period from 2019 to 2022, the inflow of AW into the Barents Sea freshened by up to 0.1 g kg^{-1} compared to previous decades. This led to an increased temperature gradient across the PF and a reduced poleward transport of warm water.

Using data targeted to resolve the dynamics and variability of the PF, we describe the structure of the front, its variability and associated mixing. Ocean stratification, currents, and turbulence data were obtained during seven ship transects across the PF near 77°N , 30°E in fall and winter conditions. These transects are complemented by nine glider missions using ocean gliders, one of which was equipped with microstructure sensors to measure turbulence. Across the front, we observe warm and salty AW intruding below the colder and fresher PW, setting up a baroclinic front and geostrophic currents reaching 25 cm s^{-1} , with estimated eastward transport of $0.3 \pm 0.2 \text{ Sv}$. Short-term variability below the surface mixed layer arises from tidal currents and mesoscale eddies. While the effects of tidal currents are mainly confined to the bottom boundary layer, eddies induce significant shifts in the position of the front, and alter the isopycnal slopes and the available potential energy of the front. Substantial water mass transformation is observed across the front, likely a result of eddy-driven isopycnal mixing. Despite the seasonal changes in the upper layers of the front (0–100 m) influenced by atmospheric forcing, sea ice formation, and brine rejection, the position of the front beneath 100 m depth remained relatively unperturbed.

Collectively, the papers in this thesis have advanced our knowledge about the AW inflow into the Arctic Ocean, its pathways and mechanisms controlling the mixing and distribution of heat from AW to the surrounding Arctic waters. This work represents an important step towards comprehending the influence of AW on the Arctic Ocean, essential for sustainable management and predicting the future of Arctic marine ecosystems.

Abstract in Norwegian

Nordishavet spiller en viktig rolle i det globale klimasystemet. Produksjon av kaldt vann med høy tetthet, samt frysing av sjøis i Arktis, bidrar til å drive den Atlantiske meridionale omveltningssirkulasjonen og kan påvirke atmosfærens sirkulasjonsmønstre så langt sør som til midlere breddegrader. Atlanterhavsvann som strømmer gjennom Framstredet og Barentshavet, inn i Arktis, regulerer både produksjonen av vann med høy tetthet og utstrekningen av sjøis. Dermed har Atlanterhavsvann en nøkkelrolle i Arktis og det globale klimasystemet som helhet. Denne studien beskriver innstrømningsveiene til Atlanterhavsvann, samt de underliggende mekanismene som styrer innstrømningen, prosessene for varmetap og blanding med de Arktiske vannmassene nord for Svalbard og i det nordvestlige Barentshavet. Data samlet inn ved hjelp av autonome undervannsfartøy (AUV-er) er sentrale i denne studien. Mer enn 15 000 hydrografiske profiler er samlet inn i løpet av fem tokt og elleve AUV-opdrag mellom 2018 og 2022, og er presentert i form av fire artikler. Data er samlet inn som en del av prosjektet Arven etter Nansen. Ved bruk av observasjoner langs kontinentalskråningen nord for Svalbard, mellom 12°Ø og 24°Ø , beskriver vi hydrografisk struktur, volumtransport og sirkulasjonsmønstre til Atlanterhavsgrensestrømmen. Volumtransporten til grensestrømmen når et maksimum på $3.0 \pm 0.2 \text{ Sv}$ i oktober, men styrken til grensestrømmen er følsom for vindstress, og dobler volumtransporten sin på mindre enn en uke når gjennomsnittlig vindstress over regionen endrer seg. En tidligere ukjent bunnintensivert vannstrøm observeres å strømme parallelt med grensestrømmen mellom 1500 og 2000 meter dybdekonturene. Historiske data i regionen støtter tilstedeværelsen av den bunnintensiverte vannstrømmen.

På grunn av gunstige logistiske og miljømessige forhold i Barentshavet, konsentrerte oppfølgingsstudiene seg om det nordvestlige Barentshavet. Måltrettede målinger ved bruk av AUV-er gir en stor forbedring i romlig og tidsmessig dekning av observasjoner. For å utnytte teknologien, spesielt ved målinger av turbulens, utforsket vi potensialet til en propelldrevet AUV. Vi utstyrte AUV-en med en turbulenspakke og rapporterer datakvaliteten, samt diskuterer begrensningene av dissipasjonsestimater fra skjærsensorene. Det propelldrevne AUV-opdraget i Barentshavet, vinteren 2021, varte i 5 timer, og AUV-en hadde en typisk horisontal hastighet på 1.1 m s^{-1} . AUV-en ble programmert for å finne og krysse maksimal temperaturgradient på 10, 20 og 30 m dyp langs 4 km strekk. Selv om AUV-vibrasjonene, på grunn av propellen, forstyrrer målingene med skjærsensorene, filtreres støyen bort ved å fjerne vibrasjonsinduserte komponenter fra skjær-spekter ved bruk av akselerometersignal. Dissipasjonsestimater fra AUV-en viser god overensstemmelse med nærliggende vertikale mikrostrukturprofiler fra skip, noe som indikerer at turbulensmålingene fra oppsettet er pålitelige for dette relativt turbulente miljøet. Imidlertid er de laveste pålitelige dissipasjonsratene

begrenset til $5 \times 10^{-8} \text{ W kg}^{-1}$, noe som gjør dette oppsettet uegnet for bruk i hav hvor det er lite turbulens.

Sirkulasjonsveier, hydrografi og volumtransport av Atlanterhavsvann og Arktiske vann i det nordvestlige Barentshavet utforskes ved hjelp av data fra tre tokt og ni glideroppdrag gjennomført mellom 2019 og 2022, samt historiske data samlet mellom 1950 og 2009. Vi setter søkelys på utveksling og dynamikk på tvers av Polarfronten og nærliggende område. Observasjonene våre viser at $0.9 \pm 0.1 \text{ Sv}$ av Atlanterhavsvann når Polarfront-regionen før vannet sprer seg langs flere forgreninger og til slutt dykker under Arktiske vannmasser. Mengden Atlanterhavsvann som lagres nord for Polarfronten kontrolleres av tetthetsforskjellen mellom Atlanterhavsvannet og det Arktiske vannet, og nådde et maksimum på 90-tallet da det Arktiske vannet nord for fronten var spesielt ferskt. I nyere tid (2019 til 2022) ble Atlanterhavsvannet som strømmer inn i Barentshavet opptil 0.1 g kg^{-1} ferskere sammenlignet med tidligere tiår. Dette førte til en økt temperaturgradient på tvers av Polarfronten og en redusert transport av varmt vann nordover på tvers av fronten.

Ved bruk av data fra to tokt og fire glideroppdrag, spesifikt samlet for å undersøke dynamikken og variabiliteten til Polarfronten, beskriver vi strukturen til fronten, dens variasjon og forekomsten av blanding av vannmasser. Vi observerer at varmt og salt Atlanterhavsvann trenger inn under kaldere og ferskere Arktisk vann, noe som setter opp en baroklin front og en geostrofisk strøm med hastigheter opp mot 25 cm s^{-1} . Den estimerte østlige transporten fra den geostrofiske strømmen er $0.3 \pm 0.2 \text{ Sv}$. Korttidsvariasjoner i dypet, under øvre grenselag, skyldes tidevannsstrømmer og mesoskala virvler. Effektene av tidevannsstrømmer er hovedsakelig begrenset til bunnsjiktet, mens virvlene betydelig påvirker posisjonen til fronten og endrer helningen til tetthetslinjene og følgelig den tilgjengelige potensielle energien i fronten. Betydelig transformasjon av vannmasser observeres på tvers av fronten, noe som sannsynligvis skyldes virvelindusert blanding langs tetthetskonturene. Til tross for sesongendringer i de øvre grenselag på tvers av fronten (0-100 m), forble posisjonen til fronten under 100 m dybde relativt uforstyrret.

Samlet sett har artiklene i denne avhandlingen bidratt til å øke vår kunnskap om innstrømmingen av Atlanterhavsvann i Nordishavet, dens veier og mekanismer som kontrollerer blandingen og distribusjonen av varme fra Atlanterhavsvannet til de omkringliggende Arktiske vannmassene. Dette arbeidet representerer et viktig skritt i retning av å forstå Atlanterhavsvannet sin innflytelse på Nordishavet, noe som er avgjørende for bærekraftig forvaltning og for å forutsi fremtiden til de Arktiske økosystemene.

Outline

This thesis consists of an introductory part and four scientific research papers. The introductory part is the first 5 chapters. Chapter 1 gives an introduction to the motivation and objective of this study, and Chapter 2 gives an overview of the scientific background relevant for the results presented. Data and methods are described in Chapter 3, followed by a summary of the scientific results in Chapter 4. Concluding remarks and future perspectives are presented in Chapter 5. The four research papers included in this thesis are presented in Chapter 6, and listed below. In addition to the four research articles forming the body of my dissertation, I contributed to 7 research articles published or in review for publication in scientific journals, and 12 data sets that are quality-controlled and made openly accessible.

List of papers

- I. **Kolås, E. H.**, Koenig, Z., Fer, I., Nilsen, F., Marnela, M. (2020). *Structure and Transport of Atlantic Water North of Svalbard From Observations in Summer and Fall 2018*. Journal of Geophysical Research: Oceans, 125(9), e2020JC016174.
- II. **Kolås, E. H.**, Mo-Bjørkelund, T., Fer, I. (2022). *Technical note: Turbulence measurements from a light autonomous underwater vehicle*. Ocean Science, 18(2), 389-400.
- III. **Kolås, E. H.**, Baumann, T. M., Skogseth, R., Koenig, Z., Fer, I. (2023). *Circulation and hydrography in the northwestern Barents Sea: insights from recent observations and historical data (1950–2022)* Journal of Geophysical Research: Oceans, in review.
- IV. **Kolås, E. H.**, Fer, I., Baumann, T. M. (2023) *The Polar Front in the northwestern Barents Sea: structure, variability and mixing*. Submitted to Ocean Science.

Additional paper contributions

- A. **Kolås, E. H.**, Fer, I. (2018). *Hydrography, transport and mixing of the West Spitsbergen Current: the Svalbard Branch in summer 2015*. Ocean Science, 14(6), 1603-1618, <https://doi.org/10.5194/os-14-1603-2018>.
- B. Koenig, Z., Fer, I., **Kolås, E. H.**, Fossum, T. O., Norgren, P., Ludvigsen, M. (2020). *Observations of Turbulence at a Near-Surface Temperature Front in the Arctic Ocean*. Journal of Geophysical Research: Oceans, 125(4), e2019JC015526, <https://doi.org/10.1029/2019JC015526>.

- C. Fer, I., Koenig, Z., Kozlov, I. E., Ostrowski, M., Rippeth, T. P., Padman, L., Bosse, A., **Kolås, E. H.** (2020). *Tidally Forced Lee Waves Drive Turbulent Mixing Along the Arctic Ocean Margins*. *Geophysical Research Letters*, 47(16), e2020GL088083, <https://doi.org/10.1029/2020GL088083>.
- D. Koenig, Z., **Kolås, E. H.**, Fer, I. (2021). *Structure and drivers of ocean mixing north of Svalbard in summer and fall 2018*. *Ocean Science*, 17(1), 365-381, <https://doi.org/10.5194/os-17-365-2021>.
- E. Koenig, Z., Kalhagen, K., **Kolås, E. H.**, Fer, I., Nilsen, F., Cottier, F. (2022). *Atlantic Water Properties, Transport and Heat Loss From Mooring Observations North of Svalbard*. *Journal of Geophysical Research: Oceans*, 127(8), e2022JC018568, <https://doi.org/10.1029/2022JC018568>.
- F. Koenig, Z., Fer, I., Chierici, M., Fransson, A., Jones, E., **Kolås, E. H.** (2023). *Diffusive and advective fluxes of inorganic nutrients and dissolved inorganic carbon in the Barents Sea in autumn*. *Progress in Oceanography*, 219, 103161, <https://doi.org/10.1016/j.pocean.2023.103161>.
- G. Mo-Bjørkelund, T. **Kolås, E. H.**, Fer, I. (in review at *Journal of Field Robotics*). *Adaptive tracking of the Barents Sea polar front using an autonomous underwater vehicle*.

Data set contributions

- a. Fer, I. et al. (2019). *Physical oceanography data from the cruise KH 2018709 with R.V. Kronprins Haakon, 12-24 September 2018*. NMDC [data set], <https://doi.org/10.21335/NMDC-2039932526>.
- b. **Kolås, E. H.**, Fer, I. (2020). *Physical oceanography data from a Seaglider mission north of Svalbard, late fall 2018*. NMDC [data set], <https://doi.org/10.21335/NMDC-1841837601>.
- c. Fer, I., Koenig, Z., Bosse, A., Falck, E., **Kolås, E. H.**, Nilsen, F. (2020). *Physical oceanography data from the cruise KB 2018616 with R.V. Kristine Bonnevie*. NMDC [data set], <https://doi.org/10.21335/NMDC-2047975397>.
- d. Fer, I., Mo-Bjørkelund, T., **Kolås, E. H.** (2021). *Dissipation measurements from AUV transects across a surface temperature front in the Barents Sea*. NMDC [data set], <https://doi.org/10.21335/NMDC-1821443450>.
- e. **Kolås, E. H.**, Fer, I., Peterson, A. Brakstad, A., Elliott, F. (2022). *Physical oceanography data from gliders in the Barents Sea, August 2019 - February 2021*. NMDC [data set], <https://doi.org/10.21335/NMDC-381060465>.
- f. Fer, I. et al. (2023). *Ocean hydrography and current profiles from the Nansen Legacy cruise to the northern Barents Sea, GOS2020113, October 2020*. NMDC [data set], <https://doi.org/10.21335/NMDC-1752779505>.
- g. Fer, I. et al. (2023). *Ocean hydrography and current profiles from the Nansen Legacy Winter Process Cruise to the northern Barents Sea, KH2021702, February 2021*. NMDC [data set], <https://doi.org/10.21335/NMDC-1544015310>.

-
- h. Fer, I. et al. (2023). *Ocean hydrography and current profiles from the Nansen Legacy Process Cruise to the Barents Sea, KB2022625, October 2022*. NMDC [data set], <https://doi.org/10.21335/NMDC-943526062>.
 - i. Fer, I., Baumann, T., Elliott, F., **Kolås, E. H.** (2023). *Ocean microstructure measurements using an MSS profiler during the Nansen Legacy cruise, GOS2020113, October 2020*. NMDC [data set], <https://doi.org/10.21335/NMDC-239170563>.
 - j. Fer, I., Baumann, T., Kalhagen, K., Koenig, Z., **Kolås, E. H.** (2023). *Ocean microstructure measurements using an MSS profiler during the Nansen Legacy cruise, KH2021702, February 2021*. NMDC [data set], <https://doi.org/10.21335/NMDC-1939445412>.
 - k. Fer, I. et al. (2023). *Ocean microstructure measurements using an MSS profiler during the Nansen Legacy cruise, KB2022625, October 2022*. NMDC [data set], <https://doi.org/10.21335/NMDC-1169583367>.
 - l. Fer, I., **Kolås, E. H.**, Elliott, F. (2023). *Dissipation measurements from a Slocum glider at the Barents Sea Polar Front, October 2020*. NMDC [data set], <https://doi.org/10.21335/NMDC-1033548414>.

Contents

Scientific environment	iii
Acknowledgements	v
Abstract	vii
Abstract in Norwegian	ix
Outline	xi
1 Introduction	1
1.1 Motivation	1
1.2 The Nansen LEGACY project	3
1.3 Objectives	4
2 Scientific background	7
2.1 Atlantic Water inflow through Fram Strait and across the Yermak Plateau	7
2.2 Atlantic water inflow into the Barents Sea	11
2.3 The Barents Sea Polar Front	13
3 Data and Methods	17
3.1 Data	17
3.1.1 Data acquired from autonomous underwater vehicles	17
3.1.2 Turbulence Package on AUVs	25
3.1.3 Turbulence measurements from ship	26
3.1.4 Hydrographic Measurements From the Nansen Legacy Cruises	27
3.1.5 Current Profiles From Cruises	27
3.1.6 Historical data	28
3.1.7 NORA10	28
3.2 Methods	29
3.2.1 Water masses	29
3.2.2 Detiding current measurements	29
3.2.3 Objective interpolation of depth average currents	30
3.2.4 Synoptic and Composite sections	31
3.2.5 Objectively interpolated horizontal layers	32
3.2.6 Along-path rate of change of heat content	32
3.2.7 Barents Sea Polar Front position	33
3.2.8 Turbulence measurements	33

4	Summary of the scientific results	35
5	Conclusions	43
5.1	Main takeaways	43
5.2	Outlook and future perspective	44
6	Papers	47
	Bibliography	159

Chapter 1

Introduction

1.1 Motivation

The Arctic Ocean plays an indispensable role within the intricate framework of the global climate system (Timmermans and Marshall, 2020). Cold and briny dense water in the Arctic Ocean is formed through heat loss to the atmosphere and sea ice freezing. The dense water contributes to the functioning of the Atlantic Meridional Overturning Circulation (AMOC), thereby facilitating the distribution of heat and nutrients worldwide (Aagaard et al., 1985). Furthermore, alterations in the expanse of sea ice in the Arctic Ocean exert influence over atmospheric circulation patterns, not solely confined to the Arctic region, but potentially reaching as far as mid-latitudes (Honda et al., 1996; Grassi et al., 2013; Cassano et al., 2014; Mori et al., 2014). Central to the regulation of both the production of dense water in the Arctic Ocean and the extent of sea ice is the inflow of Atlantic water (AW) into the Arctic basin. While the ocean currents are rarely coherent, laminar streams of flows, they can be conceptualized as circulation paths transporting specific water masses. Analogous to the arteries within the human body, the inflow of AW into the Arctic Ocean serves as a conduit for delivering heat, salt, and nutrients.

The inflow of AW, characterized by its relatively elevated temperature and salinity compared to the surrounding Arctic waters, undergoes a cooling process upon entering the shallow shelf seas of the Arctic Ocean (Helland-Hansen and Nansen, 1909). This cooling process contributes to the production of saline cold waters, contributing to the intermediate and deep waters in the Arctic basin (Midttun, 1985; Årthun et al., 2011). Subsequently, these deep waters eventually exit the Arctic region as a deep-water overflow, contributing to the perpetuation of the AMOC (Meincke et al., 1997; Brakstad et al., 2023). Notably, the precise location of deep-water formation, linked with the position of the Arctic Ocean sea ice edge, is likely important in determining the strength of the AMOC (Bretones et al., 2022).

The inflow of AW exerts a direct influence over the dynamics, volume, and variability of sea ice within the Arctic Ocean (Carmack et al., 2015; Polyakov et al., 2017, 2023). The presence of warmer AW contributes significantly to the process of sea ice melting, thereby

shaping the extent and thickness of the ice cover (Årthun et al., 2012; Polyakov et al., 2023). Temporal records of AW inflow reveal a discernible rise in its temperature over recent decades (Skagseth et al., 2008; Beszczynska-Möller et al., 2012), leading to a larger fraction of the Arctic Ocean being occupied by AW (Oziel et al., 2016; Polyakov et al., 2023). Consequently, this phenomenon has induced a corresponding reduction in sea ice coverage, resulting in the emergence of new ice-free regions that persist throughout the year (Onarheim et al., 2014; Onarheim and Årthun, 2017; Mohamed et al., 2022). The progressive retreat of sea ice has considerable ramifications for the Arctic ecosystems.

Central to the AW inflow and its importance for the Arctic ecosystem are the seas around the Svalbard Archipelago. AW enters the Arctic Ocean through the shallow Barents Sea and along the continental slope west of Svalbard. Here AW cools through interaction with the atmosphere and surrounding water masses (Boyd and D'Asaro, 1994; Gerland et al., 2023). Northwest of Svalbard, the AW passes around and across the shallow Yermak Plateau (Gascard et al., 1995; Cokelet et al., 2008; Koenig et al., 2017; Fer et al., 2023f), before continuing as a boundary current along the continental slope north of Svalbard (Cokelet et al., 2008; Pérez-Hernández et al., 2017, 2019; Kolås et al., 2020). The Yermak Plateau and the continental shelf break north of Svalbard is a highly dynamic region where mixing induced by velocity shear, energetic internal waves, and eddies are common (Fer et al., 2010; Våge et al., 2016; Hattermann et al., 2016; Pérez-Hernández et al., 2017; Kolås and Fer, 2018; von Appen et al., 2022; Baumann and Fer, 2023). In the Barents Sea, AW spreads out through a series of shallow troughs, being continuously modified by the atmosphere (Smedsrud et al., 2010; Årthun et al., 2011; Gerland et al., 2023). Eventually, cooled AW subducts under fresher Arctic water masses, and a frontal region is established (Loeng, 1991; Loeng et al., 1997; Gawarkiewicz and Plueddemann, 1995). Mixing of cooled AW with brine rejection from winter sea ice formation in the frontal regions produces some of the densest waters in the Arctic (Midttun, 1985; Quadfasel et al., 1988).

The marginal ice zone, which marks the transition between the ice-free and ice-covered regions, is a vital area for primary production (Reigstad et al., 2002) and home to rich commercial fish stocks (Johannesen et al., 2012). These ecosystems are essential for the overall biodiversity and functioning of the Arctic region. However, the retreat of the sea-ice edge has led to increased production and northward expansion of boreal species, with unknown consequences for the future Arctic ecosystem (Ingvaldsen et al., 2021).

Comprehending and monitoring the inflow of AW into the Arctic Ocean is vital for predicting and managing the effects of climate change, protecting the Arctic ecosystem, and understanding the broader impacts on the Earth's climate system. However, gathering data in the Arctic is challenging and expensive. Furthermore, traditional measurement campaigns using ships have a high carbon footprint and often provide patchy observations with limited spatial and temporal resolution.

Autonomous underwater vehicles (AUVs) can potentially increase the number of mea-

surements by an order of magnitude at a relatively low cost compared to ship-based operations (Frajka-Williams et al., 2022). Additionally, AUVs may reach regions where the ship cannot access, such as under sea ice and beneath ice shelves (McPhail et al., 2019; Graham et al., 2022). The most established underwater vehicles are the ocean gliders (Eriksen et al., 2001; Schofield et al., 2007). The gliders are buoyancy-driven vehicles which makes them very energy efficient and an environmentally friendly way of collecting data, having a low carbon footprint and minimal impact on vulnerable ecosystems such as in the Arctic region. They are well suited to resolve meso- and submesoscale processes in the ocean (Testor et al., 2019) as well as turbulence (Fer et al., 2014; Frajka-Williams et al., 2022). Another type of AUVs are propeller-driven vehicles which generally provide more maneuverability, but at the cost of mission duration. Such AUV missions usually only last for a few days, but can offer high-resolution data within confined spaces and regions where a ship cannot access. Particularly in high-latitude regions where the Rossby deformation radius is only a few kilometers, these high-resolution measurements are important in order to resolve mesoscale and fine-scale processes.



Figure 1.1: Arctic sea ice. Photographer: Eivind Hugaas Kolås

1.2 The Nansen LEGACY project

This study is an integral part of the Nansen LEGACY project. The Nansen LEGACY project is an interdisciplinary Arctic research project where ten major Norwegian research institutions collaborate by sharing competence and resources. The goal is to provide knowledge on the Arctic ecosystems and physical and biogeochemical processes in light of climate change, thus

improving the basis for sustainable management of the Arctic Ocean. The project has five main research foci areas; physical drivers, human impact, the living Barents Sea, the future Barents Sea, and technology and method development.

This study is part of the physical drivers and the technology and method development areas. The physical drivers task force endeavour to learn how the physical processes in the Barents Sea control distribution of energy and matter. Understanding the local physical control is pivotal in understanding the environmental conditions, particularly for the local ecosystem, but also regarding the distribution of pollutants. The technology and method task force endeavours to develop autonomous platforms capable of handling the extreme Arctic marine environment. By utilizing autonomy, traditional ship time may be reduced and human impact on the region may be minimized.

By integrating the physical drivers and the technology and method development areas, this study utilizes and relies on autonomous vehicles to collect hydrographic, current and microstructure data in the Arctic region. The AUVs are deployed in both Arctic summer and Arctic winter conditions. Here, they sometimes operate near and under sea ice, often without any means of quick recovery, relying solely on their own autonomy.

1.3 Objectives

The focus of this research is the inflow of AW into the Arctic Ocean through Fram Strait and the Barents Sea (see Figure 2.1). The study aims to understand the intricate pathways of the AW inflow, as well as the underlying mechanisms controlling the inflow, heat loss, and mixing with the surrounding waters north of Svalbard and in the northwestern Barents Sea. Particularly the thermohaline front between the Arctic-origin waters and Atlantic-origin waters in the northwestern Barents Sea (the Barents Sea Polar Front) is studied. Crucial to this research are data collected by AUVs equipped with conductivity-temperature-depth (CTD) sensors and microstructure sensors. The term AUV in this study includes buoyancy-driven ocean gliders and a propeller-driven light-AUV. A technical objective is to integrate and use microstructure sensors on AUVs and, particularly for the propeller-driven AUV, describe its limitations for turbulence measurements. High-resolution measurements obtained by the AUVs crossing the AW inflow region and the Polar Front are used to examine the variability of the AW pathways and the Polar Front, on scales from mesoscale eddies to small-scale turbulence and mixing. This analysis sheds light on crucial aspects such as slope-basin exchanges, the dynamics of fronts, and the influence of atmospheric forces on the AW inflow. Collating 5 years of data collected from ships and AUVs since 2018, we map the circulation patterns and water properties in the region and contrast them to past decades.

The scientific results are presented in four scientific papers (Papers I-IV). Papers I and II are published, Paper III is in review and Paper IV has been submitted. The main objectives of the

papers are as follows.

- Paper I: We obtained and analyzed observations from research cruises and an autonomous underwater glider mission in summer and fall 2018. The research questions we address in this paper are: How is the structure of the AW inflow along the boundary slope north of Svalbard? What is the short-term and intraseasonal variability of the AW boundary current, and what is forcing this variability? Here we describe the hydrographic structure, volume transport, and circulation patterns of the warm AW boundary current between 12°E and 24°E north of Svalbard.
- Paper II: A technical note on measuring small-scale turbulence across a temperature front using a turbulence instrument mounted to a light AUV. The research questions we address in this paper are: Can a propeller-driven lightweight AUV carry turbulence probes, serving as a low-noise platform that does not contaminate the microstructure measurements? If so, what dissipation levels can this setup resolve? Can it operate in the open sea within Arctic waters? To address these questions we describe this novel setup and discuss the quality of the data collected.
- Paper III: The research questions we address in this paper are: What is the volume transport and structure of the different AW branches in the northwestern Barents Sea? How much AW reaches the Polar Front and how much Atlantic-origin water is able to cross the front? How do the AW properties in the northwestern Barents Sea between 2018 and 2022 compare to historical observations? We obtained and analyzed observations from research cruises and several autonomous underwater glider missions during fall and winter between 2018 and 2022. Here we describe the hydrographic structure, volume transport, and circulation patterns of the warm AW inflow into the northwestern Barents Sea near the Barents Sea Polar Front.
- Paper IV: The research questions we address in this paper are: How is the Polar Front structure on the sill between the Hopen Trench and Olga Basin in the northwestern Barents Sea, and how does this structure compare to the Polar Front elsewhere in the western Barents Sea? What is the short term and seasonal variability of the frontal structure at this location, and what are the drivers of this variability? What are the main mixing processes occurring across the front at this location? To address these questions we collected detailed observations across the northwestern Barents Sea Polar Front from research cruises and several autonomous underwater glider missions during fall and winter between 2019 and 2021. We describe the structure of the Polar Front, mixing and transformation of water masses, and the dynamics controlling the Polar Front variability.

Chapter 2

Scientific background

The Arctic Ocean's connection to the global oceanic circulation system is facilitated through exchanges through Fram Strait and the Barents Sea. AW is carried by the Norwegian Atlantic Front and Slope Currents off the western coast of Norway (Orvik and Niiler, 2002; Fer et al., 2020a; Orvik, 2022). At approximately 72°N, north of Norway, the slope current bifurcates into two main branches: one proceeds northward through Fram Strait (Beszczynska-Möller et al., 2012), constituting the West Spitsbergen Current (WSC), while the other flows into the Barents Sea through the Barents Sea Opening (BSO, Figure 2.1b). The inflow of AW is the primary source of oceanic heat and salt to the Arctic Ocean (Aagaard et al., 1985; Rudels et al., 2015). Changes in the characteristics of the AW inflow significantly influence Arctic conditions (Polyakov et al., 2017, 2023). As the AW flows toward the Arctic Ocean, its temperature and salinity properties undergo modifications due to interactions with the atmosphere, sea ice, and mixing processes with the surrounding waters (Boyd and D'Asaro, 1994; Carmack et al., 2015; Vihma et al., 2014). However, the relative role of the different cooling processes such as interactions with the atmosphere and sea ice, vertical mixing and eddy-driven mixing along isopycnals is not clear. Next, an introduction to the scientific background of the AW inflow through Fram Strait and the Barents Sea is provided separately, followed by the scientific background on the Barents Sea Polar Front.

2.1 Atlantic Water inflow through Fram Strait and across the Yermak Plateau

Pathways and circulation branches

The distribution and circulation patterns of AW within Fram Strait are complex, with multiple branches and recirculation pathways (Manley, 1995; Beszczynska-Möller et al., 2012; Marnela et al., 2013; Hattermann et al., 2016; von Appen et al., 2016; Hofmann et al., 2021). Flowing at an average velocity of approximately 0.25 m s^{-1} along the 1000-m isobath, the West Spits-

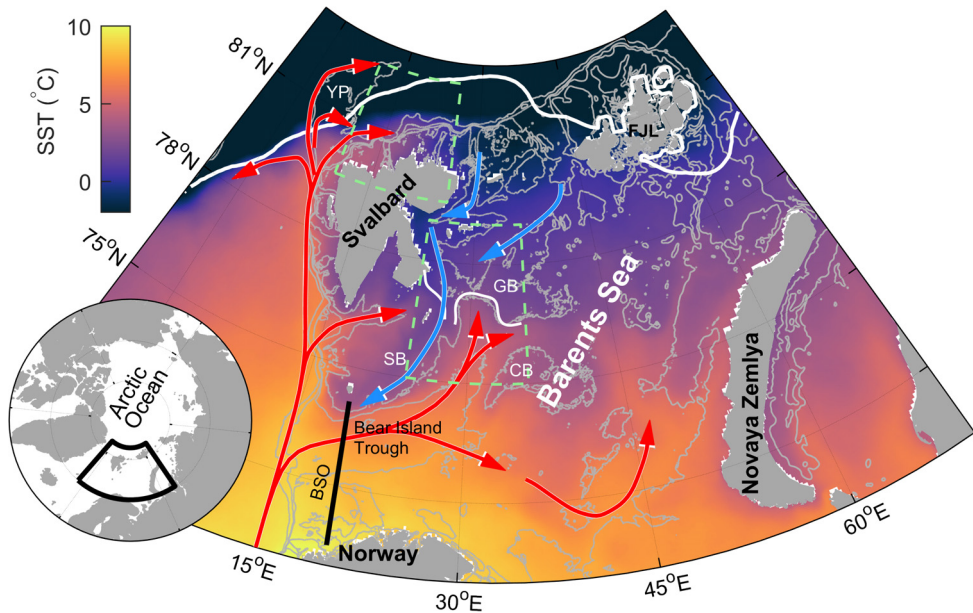


Figure 2.1: Overview map of the Barents Sea. Focus areas north of Svalbard and in the central Barents Sea are enclosed in green dashed boxes. Red arrows indicate the AW pathways. Blue arrows indicate the PW pathways. Solid white line north of Svalbard is the ice edge. Sea surface temperature (SST) and ice edge is the September-October mean between 2018 and 2022. White line in the northwestern Barents Sea marks the location of the northwestern Barents Sea polar front. Gray isobaths are drawn at 200, 350, 500 and 1000 m. Abbreviations: BSO - Barents Sea Opening, SB - Spitsbergen Bank, GB - Great Bank, CB - Central Bank, YP - Yermak Plateau, FJL - Franz Josef Land.

bergen Current (WSC) extends from Bear Island at $74^{\circ}30'N$ to the southern periphery of the Yermak Plateau (YP) situated at $79^{\circ}30'N$ (Boyd and D'Asaro, 1994; Saloranta and Haugan, 2004; Walczowski, 2013). Observations show that the WSC undergoes a bifurcation into two distinct branches where the isobaths diverge near the southern edge of the YP. This division is characterized by an outer branch, following the 1000-m isobath, and an inner branch named the Svalbard branch, tracing the 400-m isobath (Aagaard et al., 1987; Farrelly et al., 1985; Cokelet et al., 2008; Beszczynska-Möller et al., 2012).

The Svalbard branch primarily manifests as a barotropic flow, adhering to the f/H contours as it circumnavigates Svalbard, where f is the Coriolis parameter and H is water depth (Aagaard et al., 1987; Perkin and Lewis, 1984). Conversely, the outer branch exhibits a more pronounced vertical shear and a less stringent adherence to the 1000-m isobath (Aagaard et al., 1987; Fer et al., 2023f).

Analysis of observations and numerical models shows that the outer branch of the WSC undergoes a division into three distinct branches. A part of the flow detaches from the 1000-m isobath, flowing westwards and resulting in a recirculation within Fram Strait. This recirculation contributes warm and saline waters to the southward flow along the Greenland slope

(Aagaard et al., 1987; Farrelly et al., 1985; Beszczynska-Möller et al., 2012; Hattermann et al., 2016; von Appen et al., 2016; Marnela et al., 2013; Hofmann et al., 2021). Geostrophic calculations from summer hydrography show that the recirculation was strongest close to 79°N (Marnela et al., 2013). Subsequent findings from an eddy-resolving regional ocean model suggest that this recirculation contains relatively cold AW and is primarily related to the eastern rim of the Greenland Sea gyre (Hattermann et al., 2016). The recirculation of the warmest AW occurs north of 80°N, facilitated by eddies (Hattermann et al., 2016). Additionally, the recirculation branches exhibit seasonal variability with augmented transport during the winter and spring periods, related to winter storms and heightened eddy activity in these periods (von Appen et al., 2016). Two-year-long observations from moorings at this latitude show that the recirculation occurs in the form of passing eddies, which are most intense during late autumn and winter, and absent during summer (Hofmann et al., 2021), consistent with model results

The remaining segment of the outer branch is termed the Yermak branch. This branch flows along the outer peripheries of the Yermak Plateau, along the 1000-m isobath (Perkin and Lewis, 1984; Cokelet et al., 2008; Meyer et al., 2017b; Fer et al., 2023f). However, a fraction of the Yermak branch follows a more direct trajectory across the Yermak Plateau via a topographic passage situated at 80°45'N and 6°E, first detected by acoustically-tracked subsurface floats (Gascard et al., 1995). This particular flow, aptly referred to as the Yermak Pass branch, is substantiated by numerical modeling results that illustrate the progression of AW along the 700-800-m isobaths across the Yermak Plateau before subsequently rejoining the Svalbard branch (Koenig et al., 2017). Recent mooring data collected between 2017 and 2020 affirm the presence of the Yermak Pass branch and underscore a heightened volume transport magnitude during winter as compared to summer (Artana et al., 2022).

The triad of branches that enter the Arctic Ocean through Fram Strait; the Svalbard branch, the Yermak branch, and the Yermak Pass branch are hypothesized to combine north of Svalbard, continuing as a topographically steered boundary current. The Yermak Pass branch and the Svalbard branch probably merge between 10 and 15°E north of Svalbard (Menze et al., 2019; Koenig et al., 2017). However, the path of the Yermak branch and where it merges with the other two branches remain less definitive. Historical observations suggested that segments of the Yermak branch departed from the northeastern tip of the Yermak Plateau, traversing the basin before reuniting with the boundary current (Perkin and Lewis, 1984). Nonetheless, computational simulations indicate that at least portions of the Yermak branch adhere to the slope surrounding the plateau, tracing its contours and eventually converging with the other branches between 12 to 18°E, north of Svalbard (Koenig et al., 2017; Crews et al., 2018; Athanase et al., 2021). This model-derived trajectory is supported by observations from drifting ice stations during winter and spring 2015 (Meyer et al., 2017b). Further east along the continental slope, the AW flows as a boundary current with a well-developed core as well as energetic mesoscale activity (Våge et al., 2016; Pérez-Hernández et al., 2017, 2019; Koenig et al., 2022).

Volume transport and variability

The AW volume transport through Fram Strait has been monitored by a mooring array consistently maintained across Fram Strait at 79°N since 1997. The long-term average northward transport of waters with potential temperature greater than 2°C within the WSC is 3 Sv ($1 \text{ Sv} = 1 \times 10^6 \text{ m}^3 \text{ s}^{-1}$) (Beszczynska-Möller et al., 2012). Nevertheless, the precise partition of AW that enters the Arctic Ocean versus that recirculates westward to merge with the East Greenland current remains uncertain. It is estimated that up to 50 % of the AW entering Fram Strait recirculates (Manley, 1995; Marnela et al., 2013).

Traditionally, the Svalbard branch has been deemed the main conduit for AW inflow into the Arctic Ocean (Perkin and Lewis, 1984; Aagaard et al., 1987; Croke et al., 2008). This pathway exhibits an annual average AW volume transport of 1.1 Sv (Nilsen et al., 2021). Nevertheless, contemporary numerical simulations propose that the AW volume transport through the Yermak Pass branch potentially surpasses that of the Svalbard branch (Crews et al., 2019; Koenig et al., 2017; Athanase et al., 2021). Estimates of volume transport stemming from a year-long mooring array positioned at the southern edge of the Yermak Plateau disclose that a substantial proportion, as much as 1.4 Sv, of AW is directed along the Yermak Plateau during winter (Fer et al., 2023f). This is comparable to the average winter volume transport quantified through model simulations for the Yermak Pass branch (Athanase et al., 2021). Nonetheless, additional in-situ observations are required to accurately quantify the relative contributions and variations attributed to each branch.

The variability in volume transport, across interannual, seasonal, and short-term scales within the WSC is notable. The peak-to-peak variability amounts to 4 Sv for the Svalbard branch (Nilsen et al., 2021), 6 Sv for the Yermak Pass branch (Artana et al., 2022) and 3 Sv for the Yermak Branch (Fer et al., 2023f). Notably, the volume transport variability within the Svalbard branch is predominantly driven by wind patterns, responding nearly instantaneously to shifts in wind stress and wind stress curl over the Yermak Plateau (Nilsen et al., 2021). In addition, wind stress curl and coastal upwelling have been shown to drive divergence in the water on the Yermak Plateau, causing the surface AW inflow to switch between the Yermak and Svalbard branches (Fer et al., 2023f).

East of the YP, north of Svalbard, the estimates of AW volume transport span a range from 0.5 to 3.4 Sv. The variability in these estimates hinges on factors such as the location and timing of observations, as well as the specific definition of AW used (Croke et al., 2008; Våge et al., 2016; Pérez-Hernández et al., 2017; Kolås and Fer, 2018; Koenig et al., 2022). These transport estimates likely encompass the cumulative contributions originating from the Svalbard branch, the Yermak Pass branch, and the Yermak branch.

Through a year-long mooring array, Pérez-Hernández et al. (2019) ascertained that the average AW volume transport along the continental slope north of Svalbard at 30°E measured $2.1 \pm 0.2 \text{ Sv}$. This finding closely aligns with the results presented by Koenig et al. (2022), who

reported an average AW volume transport of 2.2 ± 0.2 Sv during the autumn and 1.1 ± 0.2 Sv during the winter, situated at approximately 18°E north of Svalbard. Note that Pérez-Hernández et al. (2019) defined AW as water with a potential temperature exceeding 1°C , whereas Koenig et al. (2022) defined AW as water with conservative temperature exceeding 2°C .

Along-path transformations

As the AW advances towards the Arctic, its hydrographic characteristics undergo transformations due to interactions with sea ice, the influence of colder and fresher water masses, and atmospheric forcing (Boyd and D'Asaro, 1994; Rudels et al., 2000; Onarheim et al., 2014). Over regions of abrupt topography, the presence of strong vertical shear and vigorous mixing, coupled with lateral exchange processes, serves to intensify the pace of cooling and freshening. At latitudes encompassing the YP, the along-path cooling and freshening of AW is estimated to be approximately 0.2°C per 100 km and 0.01 g kg^{-1} per 100 km, respectively, corresponding to a surface heat flux between 400 to 500 W m^{-2} (Boyd and D'Asaro, 1994; Saloranta and Haugan, 2004; Cokelet et al., 2008; Kolås and Fer, 2018). Notably, these heat flux magnitudes substantially surpass the turbulent heat fluxes typically observed near the YP. Typical heat fluxes observed on and near the plateau are $\mathcal{O}(10) \text{ W m}^{-2}$, with episodic events occasionally reaching $\mathcal{O}(100) \text{ W m}^{-2}$ (Sirevaag and Fer, 2009; Meyer et al., 2017a; Fer et al., 2010). Further east, along the continental slope north of Svalbard, mixing events induced by tidally-driven nonlinear internal waves, winds, and frontal instabilities have been observed and the turbulent heat fluxes are reported being at the order of $\mathcal{O}(1)$ - $\mathcal{O}(10) \text{ W m}^{-2}$ (Fer et al., 2020b; Koenig et al., 2020, 2021). It is not clear which processes can sustain the observed along-path cooling rates; nonetheless, eddies are thought to play a major role in this heat loss (Våge et al., 2016; Kolås and Fer, 2018; Crews et al., 2019). Eastward of the 20°E meridian, observations tend to suggest considerably diminished along-path cooling rates compared to the region around the YP (Pérez-Hernández et al., 2017).

2.2 Atlantic water inflow into the Barents Sea

The Barents Sea stands witness to the ingress of AW through the BSO, a process characterized by a range of flow dynamics and volumetric variations. The current state of knowledge of the physical, chemical and biological systems in the Barents Sea is reviewed in Gerland et al. (2023). The average annual influx of AW through the BSO is 2 Sv, when defined as water with temperatures above 3°C , with a peak of 2.8 Sv in January and a minimum of 1.3 Sv observed in April (Skagseth et al., 2008; Smedsrud et al., 2010). The observed AW transport estimates agree well with model simulations showing an average AW inflow of 2.3 ± 0.4 Sv through the BSO (Årthun et al., 2012). The total average inflow through the BSO is about 3.2 Sv, regardless

of water mass, of which 1.2 Sv is thought to recirculate within the Bear Island Trough (Loeng et al., 1997; Skagseth, 2008; Smedsrud et al., 2010).

The AW that enters the Barents Sea largely follows the region's topography as it moves up the Bear Island Trough (Loeng, 1991). Once it reaches the Central Bank, this inflowing AW divides into two primary branches; one continuing its journey eastward tracing a path south of the Central Bank, and a second branch heading northward, following the Hopen Trench (Loeng, 1991; Årthun et al., 2012; Oziel et al., 2016).

The AW branch that flows eastward south of the Central Bank occupies the southern half of the Barents Sea as it progresses further (Oziel et al., 2016; Barton et al., 2018). However, the specific distribution of AW between the eastern path south of the Central Bank and the northern route into the Hopen Trench remains uncertain due to a lack of transport estimates. The Hopen Trench branch continues its northward course, reaching the Great Bank where another split occurs. One branch turns eastward into the Persey Trench, while the other continues its journey along the Hopen Trench (Loeng, 1991).

Despite the significance of these AW branches in the inflow dynamics of the Barents Sea, comprehensive documentation of their characteristics, such as volume transport, heat content, predominant routes, and properties as they reach the northern expanses of the Barents Sea, is limited.

On the southeastern slope of the Spitsbergen Bank, reported results diverge regarding the direction of AW flow. Some studies assert the presence of a warm-core jet of AW that progresses northeastward along the 300 m isobath (Loeng, 1991; Li and McClimans, 1998). In contrast, alternative observations have documented a westward AW flow on the southern flank of the Spitsbergen Bank, encompassing the region between the 260 m and 400 m isobaths (Parsons et al., 1996; Gawarkiewicz and Plueddemann, 1995). The westward AW flow is attributed to recirculating AW within the Bear Island Trough (Skagseth, 2008). Barton et al. (2018) propose that AW situated northeast of the recirculating branch follows a clockwise trajectory around the Hopen Trench due to potential vorticity constraints, as would be the case where the outflow depth in the northern basin is shallower than the inflow. However, the circulation in the southeastern vicinity of the Spitsbergen Bank, spanning the Hopen Trench and Persey Trench, is complex and the underlying dynamics are affected by sea level variations, tidal flows, and wind patterns (Våge et al., 2014).

Long-term observations of AW inflow through the BSO offer compelling insights into the changing dynamics of this critical region. Over the span of four decades, from 1965 to 2006, the temperature of the AW core increased by 1°C, coinciding with a volume flux rise of 0.1 Sv per year between 1997 and 2006 (Skagseth et al., 2008). These findings agree with more recent studies showing that the fraction of AW in the Barents Sea surged from around 10% in 1980 to approximately 30% by 2011 (Oziel et al., 2016). This notable shift, referred to as "atlantification," has profound implications. It has facilitated an enhanced productivity and northward expansion of boreal species in the Barents Sea (Ingvaldsen et al., 2021). Atlantifi-

cation is strongly correlated with the gradual retreat of the sea ice edge in the Barents Sea, where the sea ice area reduced by 50% between 1998 and 2008 (Årthun et al., 2012). Furthermore, the sea ice concentration over the ice-covered expanse in the Barents Sea declined by nearly 7% per decade from 1982 to 2020 (Mohamed et al., 2022). These trends, reflecting the diminishing sea ice presence, are inherently intertwined with the ongoing "atlantification" process and signify the complex interplay between ocean and atmospheric changes in the Barents Sea.

2.3 The Barents Sea Polar Front

The northwestern sector of the Barents Sea is primarily occupied by Polar Water (PW) entering from the north, characterized by its low temperatures ($\Theta < 0^{\circ}\text{C}$) and relatively low density ($\sigma_0 < 27.97 \text{ kg m}^{-3}$) (Loeng, 1991; Lien et al., 2017). The region where the PW meets the warmer and saltier AW is designated as the Barents Sea Polar Front (PF) (Loeng, 1991; Våge et al., 2014; Oziel et al., 2016). The PF is an integral component of the North Polar Frontal Zone encompassing the Nordic Seas (Rodionov, 1992). The frontal zone in the Nordic Seas has substantial thermohaline variability, and is a highly dynamic region where features such as structures shaped by local wind patterns, precipitation effects, internal waves, isolated eddies, meandering fronts, and advective intrusions span spatial scales from a few to hundreds of kilometers (Rodionov, 1992).

In the Barents Sea, the PF stands as an important site for water mass transformation, influencing local biogeochemistry and ecological systems (Descôteaux et al., 2021), as well as larger-scale dynamics of the Arctic Ocean's overturning circulation and ventilation (Årthun et al., 2011; Våge et al., 2014). In the western reaches of the Barents Sea, the PF maintains a relatively stable position, closely tracing the 200-250 m isobath from Bear Island along the Spitsbergen Bank to the Great Bank (Johannessen and Foster, 1978; Gawarkiewicz and Plueddemann, 1995; Oziel et al., 2016; Barton et al., 2018). Nonetheless, the climate of the Barents Sea has been shown to affect the position of the front south of Bear Island. Warmer periods characterized by stronger winds have led to an upslope shift of the PF compared to colder periods (Ingvaldsen, 2005). These findings hold implications for the future behavior of the Polar Front as the Barents Sea enters a phase of warmer inflowing AW and amplified volume flux (Skagseth et al., 2020). Around the Central Bank, and in the eastern Barents Sea, the PF is not as stationary, covering a broader zone of mixing (Oziel et al., 2016).

While comprehensive investigations into the frontal structure of the Barents Sea are relatively scarce, pioneering efforts were undertaken on the southern flank of the Spitsbergen Bank during the Barents Sea Polar Front Experiment in the summer of 1992 (Gawarkiewicz and Plueddemann, 1995; Parsons et al., 1996). This experiment shed light on the intricate dynamics of the PF, offering crucial insights into its structure and behavior.

At the surface of the PF, typically within the upper 20-40 meters, a distinct horizontal

salinity gradient delineates the boundary between Arctic meltwater in the northern region and Atlantic surface water in the southern region. Here, the horizontal temperature gradient is weak, and the manifestation of the surface front occurs as a density front, with maximum density difference across the front of about 0.8 kg m^{-3} (Parsons et al., 1996). Beneath the surface front, the deeper front is characterized by a horizontal temperature gradient, supporting the bulk of fine-scale structures associated with the front (Parsons et al., 1996). However, the gradients weaken below 100 meters, likely influenced by bottom boundary mixing, leading to a broader frontal zone. Notably, below 100 meters, the horizontal temperature and salinity gradients are density compensating, yielding a barotropic front defined by horizontal density lines (Gawarkiewicz and Plueddemann, 1995; Parsons et al., 1996). While other observations such as those by Johannessen and Foster (1978), Fer and Drinkwater (2014) and Våge et al. (2014) agree on the overall structure of the PF, the circulation and interaction of AW and PW across the front is still unclear.

Direct measurements of turbulent mixing along the PF suggest that diapycnal mixing is mainly confined to the boundary layers during strong tidal currents and/or strong wind events (Sundfjord et al., 2007; Fer and Drinkwater, 2014). Using detailed measurements of ocean turbulence, hydrography, currents, and nutrients from the PF across Spitsbergen Bank near Hopen in May 2008, Fer and Drinkwater (2014) observed enhanced biological activity between a density compensated thermohaline front near the 150-m isobath and a tidal front on the cold side of the PF. Tidal currents along the slope of the Spitsbergen Bank can have a peak-to-peak variability of 1 m s^{-1} , and bottom boundary dissipation rates have been estimated to be as high as $10^{-6} \text{ W kg}^{-1}$ (Fer and Drinkwater, 2014). However, on the warm side of the PF, away from the boundary layers, waters are in general quiescent and mixing mainly occurs along isopycnals with interleaving layers of AW and PW (Fer and Drinkwater, 2014; Våge et al., 2014). Fer and Drinkwater (2014) propose a mechanism where water mass properties on the warm side of the front are transported along isopycnals onto the bank where tidal currents effectively mix these properties upward.

Another source for mixing along the front can be mesoscale eddies. Eddies detaching from a mean flow diffuse properties along isopycnal surfaces, redistributing heat, salt, and nutrients (McWilliams, 2008). Eddies are known to play a key role in distributing AW heat in the Arctic Ocean, particularly along the AW inflow west and north of Svalbard (von Appen et al., 2016; Hattermann et al., 2016; Crews et al., 2018; Våge et al., 2016). In the Barents Sea, satellite radar images from 2007 and 2011 indicated that eddies were frequently generated near the PF southwest of Svalbard (Atadzhanova et al., 2018). However, the role of these eddies in distributing and mixing AW in the Barents Sea is not clear. Porter et al. (2020) observed a cold-core surface eddy south of the PF in the Hopen Trench, and traced its origin back to north of the PF using satellite derived sea surface height. Combining their observations with that of Atadzhanova et al. (2018), they estimated that the annual southward transport of cold and fresh water by eddies forming in the PF region was $1.1 \times 10^{13} \text{ m}^3$. In addition, Porter et al.

(2020) state that this transport is likely an underestimate as eddies in the Barents Sea PF region tend to be masked from satellite derived sea surface temperature observations due to thermal capping. The role of Eddy-driven along-isopycnal mixing of AW across the PF in the Barents Sea is not clear and requires further investigation.

Chapter 3

Data and Methods

3.1 Data

Ocean temperature, salinity, horizontal current and microstructure profiles were collected from 2018 to 2022, in the study regions north of Svalbard and in the northwestern Barents Sea (Figure 2.1b and 3.2). The observations include measurements from five scientific cruises and eleven autonomous underwater vehicle (AUV) missions, collected during a combined period of 571 days as part of the Nansen Legacy project. Research cruises were conducted onboard the Research Vessels (RV) *G.O. SARS*, *Kronprins Haakon* and *Kristine Bonnevie*. In total, the hydrographic data consists of 15,878 conductivity-temperature-depth (CTD) profiles, with 93% from AUVs. Additional data include shipboard acoustic Doppler current profiler data from five other Legacy cruises spanning the same period, historical CTD data from the UNIS hydrographic database, and satellite and model-derived products. Further information about the platforms and products used is provided in the subsequent subsections. An illustration of the data collection timeline is shown in Figure 3.1. Detailed metadata for the cruises and AUV missions are listed in Table 3.1.

3.1.1 Data acquired from autonomous underwater vehicles

In this study, we utilized three different AUVs, namely the Light AUV (LAUV) from Ocean-Scan and two types of ocean gliders. In the following, sg560, sg561, sg562 and sg564 are Seagliders, *Odin* and *Durin* are Slocum gliders, and *Harald* is the LAUV. The distinct characteristics of each AUV are outlined below.

Ocean Glider Data

An ocean glider (referred to as a glider hereafter) is a buoyancy-driven, remotely-piloted underwater vehicle (Figures 3.3, 3.4 and 3.5). Positive buoyancy is generated by pumping oil into an external bladder, while negative buoyancy is generated by bleeding oil out of the blad-

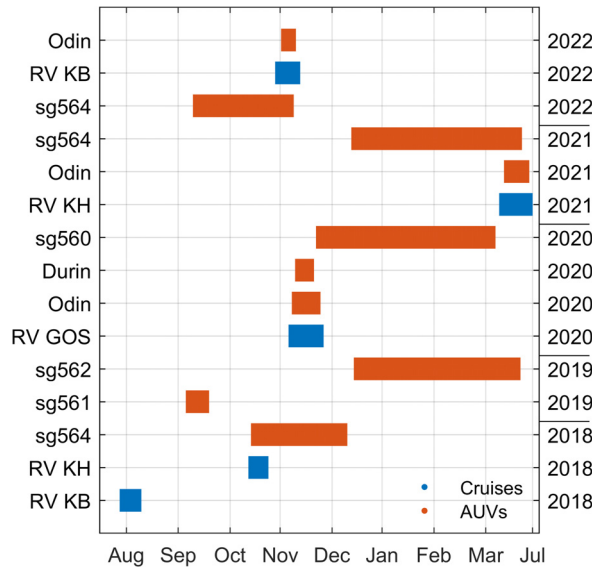


Figure 3.1: Temporal coverage of the different cruises and AUV missions presented in this study. The bottom three show the data collection north of Svalbard. Note that the AUV Harald conducted a 12 hour mission during the cruise with the RV Kronprins Haakon in February 2021 (not shown). KB: Kristine Bonnevie, KH: Kronprins Haakon, GOS: G. O. Sars.

Table 3.1: AUV and cruise metadata. The number of CTD profiles from the cruises in the Barents Sea is the sum of shipboard CTD and MSS profiles. Regions referred to are north of Svalbard (N. Svalbard), northwestern Barents Sea (NW. BS), and northwestern Barents Sea Polar Front (W. BS PF). Note that also the Harald mission collected CTD data, but it was not used in this study.

Vessel	Start - End	Region	# of CTD profiles
RV KB	27 June 2018 - 10 July 2018	N. Svalbard	150
RV KH	12 September 2018 - 24 September 2018	N. Svalbard	160
sg564	17 September 2018 - 11 November 2018	N. Svalbard	754
sg561	7 August 2019 - 19 August 2019	NW. BS	308
sg562	15 November 2019 - 1 March 2020	NW. BS	2,568
RV GOS	6 October 2020 - 27 October 2020	NW. BS	269
Odin	8 October 2020 - 24 October 2020	NW. BS PF	800
Durin	10 October 2020 - 20 October 2020	NW. BS	678
sg560	22 October 2020 - 11 February 2021	NW. BS	2,534
RV KH	9 February 2021 - 1 March 2021	NW. BS	261
Harald	26 February 2021, 5 hours	NW. BS	n/a
Odin	12 February 2021 - 25 February 2021	NW. BS	748
sg564	12 November 2021 - 22 February 2022	NW. BS	3,426
sg564	9 August 2022 - 9 October 2022	NW. BS	2,492
RV KB	28 September 2022 - 13 October 2022	NW. BS	328
Odin	2 October 2022 - 9 October 2022	NW. BS PF	402

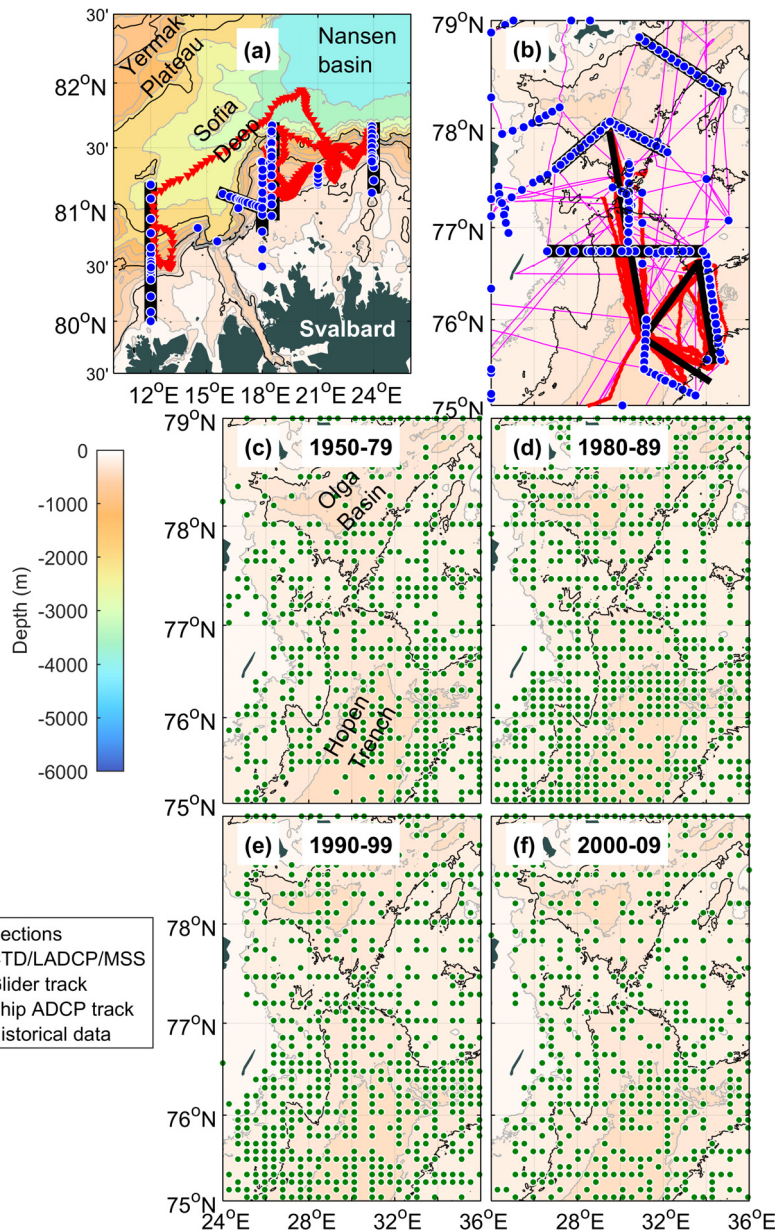


Figure 3.2: Overview of data collection locations for the data used in this study (a) Data collected north of Svalbard. (b) Data collected in the northwestern Barents Sea. The regions in (a) and (b) correspond to the regions north and southeast of Svalbard marked by the dashed green boxes in Figure 2.1. (c-f) Historical data coverage averaged over 10 km by 10 km bins in the northwestern Barents Sea for the years indicated in the figures. Black isobaths show the 200, 800 and 1500 m isobaths.

der. Forward propulsion is generated by the wings, while dive angle (pitch) and turning (roll) is determined by the positioning of the internal battery. Between each dive, the glider calls in through a two-way Iridium communication satellite, transferring data from the latest dive and receiving updates. For this study, a total of six Kongsberg Seaglider missions and four Teledyne G3 Slocum glider missions were conducted between 2018 and 2022 (Kolås and Fer, 2020; Kolås et al., 2022a). Specifics about each mission can be found in Table 3.1. The primary objective was to chart the distribution and circulation of AW in the study regions (Figure 2.1), as well as to gather detailed observations on the interactions between AW and surrounding waters. Across these missions, a comprehensive dataset of 14,710 profiles was collected and subsequently analyzed. The typical horizontal separation between consecutive surfacing locations ranged from 1 km to 5 km, dependent on the dive's depth. The gliders operated within the range of the surface to a maximum depth of 1000 m, measuring CTD parameters during descents and ascents. Both types of gliders are equipped with acoustic altimeters to detect the seabed, and when the seafloor depth was shallower than 1000 m, the gliders executed turns between 0-20 m above the seafloor. For each dive, a depth-averaged current (DAC) was computed based on the deviation between the actual surfacing location and the projected surfacing location derived from a hydrodynamic glider flight model.

Seagliders

Each Seaglider (Figure 3.3) was equipped with a Kistler strain-gauge pressure sensor, an SBE CT Sail, and an Aanderaa dissolved oxygen sensor. The Seagliders operated with a vertical velocity of approximately 8 cm s^{-1} , and the sampling rates were typically set to acquire conductivity and temperature readings at every meter, while oxygen measurements were taken at 5 m intervals. The Seaglider data sets were processed using the University of East Anglia Seaglider toolbox, based on the methods described by Garau et al. (2011) and Frajka-Williams et al. (2011). Obvious outliers in the salinity and temperature profiles were manually flagged before applying a hydrodynamic flight regression Frajka-Williams et al. (2011) to obtain improved estimates of flow past the CT Sail. The flow past the CT Sail is important for improved salinity and temperature calculations from the unpumped CT sensor. Using the improved salinity and temperature profiles, we applied the thermal lag correction of salinity data Garau et al. (2011), before doing a detailed manual quality control of the salinity and temperature profiles. The processed values of Absolute Salinity, S_A , and Conservative Temperature, Θ , are accurate to 0.01 g kg^{-1} and 0.001°C , respectively, while the depth-averaged current (DAC) is accurate to 0.01 m s^{-1} (Seaglider, 2012, p. 9).

During post-processing, each profile was despiked by flagging values exceeding twice the root mean square (rms) value of $(x - x_s)$, where x is the profile data and x_s is a 5-point median filter. In addition, at each pressure level, standard deviation is calculated over all profiles of that mission, and outliers exceeding three standard deviations from a 2D smoothed field of the data were excluded. Post-processing unveiled noisy data with overturns, frequently encoun-



Figure 3.3: Deployment of a Kongsberg Seaglider. Photographer: Rudi Jozef Maria Caeyers

tered in the pycnocline and at the apogee of dives, as well as sporadically throughout profiles. This noise can be attributed to changes in the flow past the conductivity-temperature sensor, often associated with shifts in pitch or vertical velocity. Such variations can lead to erroneous salinity estimates due to a misalignment of conductivity and temperature measurements. To address this uncertainty in salinity estimates, we removed instances where the absolute difference between the density profile and the sorted-density profile exceeded 0.02 kg m^{-3} . The number of data points removed accounted for less than 1% of the total data, and overall, these exclusions did not impact the averaged and objectively mapped fields utilized in our analysis. Finally, salinity and temperature offset corrections were implemented after comparing the deep portions of Seaglider dives to nearby CTD profiles collected from research vessels, typically within a proximity of 3 days and 5 km from the glider profile location.

The Seagliders were operated with an ice-avoidance algorithm to prevent instrument loss in icy conditions. This algorithm employs acoustics to detect ice keels and utilizes temperature measurements to identify freezing temperatures near the surface. Upon detecting sea ice or near-freezing conditions (see Figure 3.4), a new dive would commence without surfacing. On certain occasions, northerly winds pushed sea ice over the gliders in the Barents Sea, preventing them from surfacing and obtaining a GPS fix. These events were typically short-lived, spanning only a few dives. However, in some instances, the glider remained beneath the

ice for more than 24 hours, leading to the activation of an escape mode. During this mode, the glider would turn toward a predetermined point and move away from the ice. The longest period without a GPS fix endured for 34 dives or roughly 44 hours. In situations without GPS fixes, the estimation of DAC becomes unattainable.

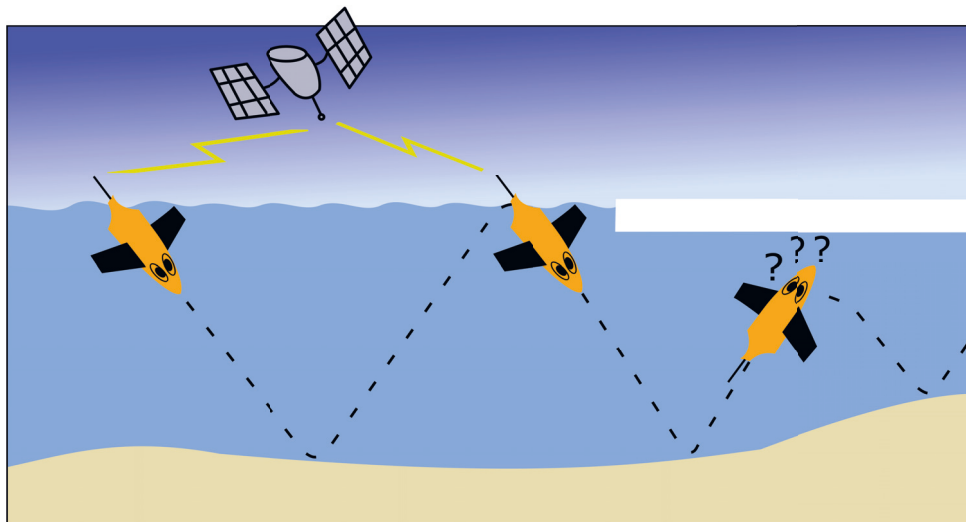


Figure 3.4: Illustration of glider near and under sea ice.

For each dive carried out without a GPS fix, the longitude and latitude coordinates along the dive tracks were interpolated linearly between the two available GPS fixes, under the assumption that the glider continued moving in a straight line. In instances where the glider shifted southward during escape mode while under sea ice, the northernmost position was extrapolated. This extrapolation was based on the most recent horizontal velocity estimate, the compass heading, and the seabed depth.

Slocums

Two electric 1000-m G3 Slocum gliders, named *Odin* and *Durin*, were deployed within the Barents Sea study area. These gliders were equipped with pumped SBE CTD sensors (CTD41CP). Operating at a sampling frequency of 0.25 Hz, the gliders maintained a typical vertical velocity of 15 cm s^{-1} . The gliders were configured to ascend to within 15 m of the seabed. The collected data underwent processing using the quality control procedures outlined in the Balearic Islands Coastal Observing and Forecasting System (SOCIB) data processing toolbox (Troupin et al., 2015). The resulting profiles have a horizontal along-track spacing of approximately 0.5 km and a vertical spacing of 1 m between data points. During post-processing, each profile underwent despiking by flagging values exceeding twice the root mean square (rms) value of $(x - x_s)$, where x is the profile data and x_s is a 5-point median filter. Furthermore, outliers that exceeded three standard deviations across all profiles at each

pressure level were excluded.

Odin was additionally equipped with a turbulence package designed to measure small-scale shear across the Polar Front, as detailed in Section 3.1.2 (Figure 3.5). Special attention was given to minimizing vibration noise within the glider to ensure that turbulence measurements remained uncontaminated. The glider's battery was configured in fixed mode, preventing the pitch motor from operating during gliding. To maintain symmetry in the profiles, autoballast control was employed, dictating pump volumes for both diving and climbing maneuvers. The depth that initiates the surfacing behavior was set to 0 m to prevent any contamination arising from the air bladder and ballast pump, which automatically activates during surfacing.



Figure 3.5: Slocum glider *Odin* with *MicroRider* ready for deployment

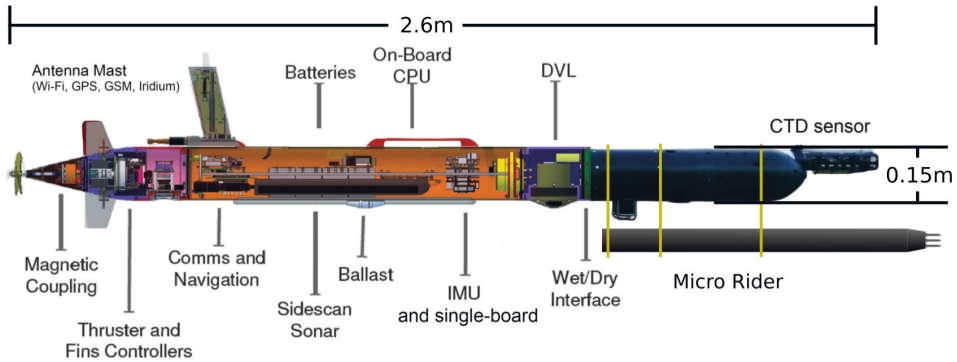


Figure 3.6: Sketch showing the LAUV used on this mission, with instruments and hardware as indicated. This sketch is published in Kolås et al. (2022b), and is a modified version of a figure in Fossum et al. (2021).

Light autonomous underwater vehicle

The Light AUV (LAUV) used in this study, named *Harald*, was developed at the Underwater Systems and Technology Laboratory at the University of Porto (Sousa et al., 2012) and is commercially produced by OceanScan Marine Systems and Technology Lda. Our LAUV, an extended version of the standard Light AUV, is rated for pressures up to 100 m and is equipped with several instruments (sketch shown in Figure 3.6).

It features a pumped CTD (SBE-49 FastCAT), a Nortek Doppler Velocity Log (DVL1000), an attitude sensor (Lord Microstrain 3DM-GX4-25), an acoustic modem, a Fluorescence sensor, and a dissolved oxygen optode. The accuracy of the LAUV measurements is approximately $\pm 0.002^\circ\text{C}$ for temperature, $\pm 0.0003 \text{ S m}^{-1}$ for conductivity, 0.3% rms of the measured value for horizontal flow speed past the instrument (measured by DVL1000), $\pm 8.5^\circ$ for yaw at the observation latitude, and $\pm 2.0^\circ$ for pitch and roll. Given the operating depth of about 250 m, the DVL1000 did not track the seafloor during this mission.

The LAUV's trajectory was determined solely by inertial navigation, with an expected drift of approximately 15% of the distance traveled. Controlled by the on-board software DUNE Unified Navigation Environment, the LAUV is configurable both in terms of hardware and software. Its mission duration typically spans a few hours to 48 hours, contingent on the operating speed. While the maximum speed can exceed 2 m s^{-1} , a normal operating speed is around 1.5 m s^{-1} . The LAUV maintains communication via satellite (Iridium), WiFi, and acoustics. Remote control within a WiFi range of about 200 m is feasible and beneficial during deployment and recovery procedures.

In this study, the LAUV was equipped with a turbulence package designed to measure small-scale shear across temperature fronts (Figures 3.6 and 3.7). The turbulence package was mounted beneath the LAUV using custom-made brackets and was connected to the AUV through a bulkhead connector and a custom-made cable. Due to the additional drag intro-

duced by the turbulence package, the operating speed during our mission was approximately 1.1 ms^{-1} .

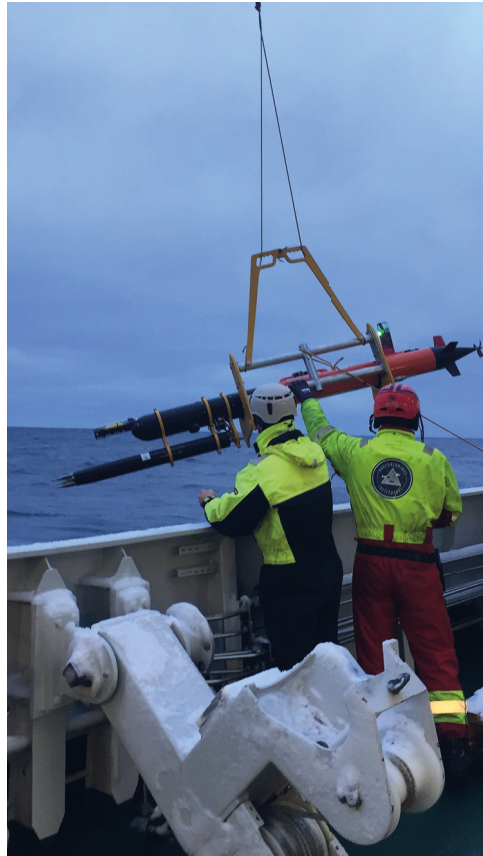


Figure 3.7: Deployment of MicroRider-1000LP mounted below the light AUV in the Barents Sea, February 2021. From left: Tore Mo-Bjørkelund and Svein Are Simonsen. Photographer: Frank Nilsen, University Centre in Svalbard.

3.1.2 Turbulence Package on AUVs

The two turbulence packages carried by the Slocum glider, *Odin*, and the LAUV, *Harald*, were integrated MicroRider-1000LPs (MRs, 1000-m rated and low power) from Rockland Scientific, Canada. Each MR was equipped with two airfoil velocity shear probes (SPM-38), a pressure transducer, a two-axis vibration sensor (consisting of a pair of piezo-accelerometers), and a high-accuracy dual-axis inclinometer. It is worth noting that the MR on *Odin* featured two fast-response thermistors (FP07), while the MR on *Harald* was equipped with only one.

The MR operates by sampling the signal along with its signal derivatives on the thermistor and pressure transducer, and additionally, the derivative for shear signals, thereby enabling

high-resolution measurements. Although both MRs are the same type of instrument, their setup differed between *Odin* and *Harald*.

The MR carried by *Odin* was affixed to the top of the glider, following a setup akin to that elucidated by Fer et al. (2014). It drew power from the glider's internal battery, rendering it capable of remote activation and deactivation. The sensors within the MR operated at a sampling rate of 512 Hz for the vibration, shear, and temperature measurements, while pitch, roll, and pressure were sampled at 64 Hz. The accuracy of the measurements was within 0.1% for pressure, 2% for the piezo-accelerometers, and 5% for the shear probes.

The MR carried by *Harald* was affixed beneath the AUV, as depicted in Figure 3.6. This MR underwent modification to align with the Tidal Energy (TE) configuration, previously employed in high-flow tidal energy channels. The TE configuration involved elevating the sampling rate to 1024 Hz for fast channels (in contrast to the usual 512 Hz), replacing the analog bus connector on the analog (ASTP) circuit board components with an anti-aliasing filter of 196 Hz (up from the standard 98 Hz), and reducing the shear channel's gain by a factor of 10, from around 1 second to 0.1 seconds. These adaptations facilitated the capturing of high wavenumbers, enabling the resolution of the shear spectrum (achieving 130 cycles per minute at 1.5 m s^{-1} with a 196 Hz anti-aliasing filter). The reduction in gain compensated for the amplified signals generated by the LAUV's relatively swift movement through the water, as the shear sensor signal intensifies in proportion to the square of speed. Power for the MR on *Harald* was sourced from a dedicated 4S1P (14.8V) Lithium-Ion battery integrated into the vehicle, with its control managed through a relay linked to the main power board within the AUV. This arrangement aimed to provide a clean power supply.

Data from both MRs were internally stored on compact flash memory cards. The turbulence sensors extended approximately 25 cm from the nose of the carrier platform (AUV), referred to as the "hotel", in order to measure turbulence outside the deformed flow field resulting from the platform's movement through the water.

The MR data underwent processing and publication in accordance with the recommendations of the ATOMIX working group (https://wiki.app.uib.no/atomix/index.php/Main_Page). The methodology is detailed in section 3.2.8.

3.1.3 Turbulence measurements from ship

During the cruises in the Barents Sea, ocean microstructure measurements were made using the long version of the Microstructure Sensor Profiler, MSS90L from Sea&Sun Technology, Germany, referred to as MSS hereafter. The MSS is a loosely-tethered free-fall instrument equipped with two airfoil probes, a fast-tip thermistor (FP07), an acceleration sensor and conventional CTD sensors for precision measurements. The sensors point downward when the instrument profiles vertically, and all sample at a rate of 1024 Hz. The instrument is ballasted for a typical fall speed of $0.6 - 0.7 \text{ m s}^{-1}$ and is decoupled from operation-induced tension

by paying out cable at sufficient speed to keep it slack. Data are transmitted in real-time to a ship-board data acquisition system. Casts were made down to about 5–15 m height above the bottom. Occasionally the profiler landed at the bottom, however, it was equipped with a sensor protection guard at the leading end.

The MSS data was processed and published following the guidelines of the ATOMIX working group. The method is outlined in section 3.2.8. MSS data from the different cruises are accessible from Fer et al. (2023a), Fer et al. (2023c) and Fer et al. (2023b).

3.1.4 Hydrographic Measurements From the Nansen Legacy Cruises

Research cruises were conducted aboard the Research Vessels (RV) *G.O. SARS*, *Kronprins Haakon*, and *Kristine Bonnevie*. CTD profiles were collected during all cruises using a Sea-Bird Scientific SBE 911plus system. The calibration of CTD salinity was performed using water samples taken at all stations at the deepest profile depth. CTD profiles, along with the current profiles (Section 3.1.5), can be accessed from Fer et al. (2023g,e,d). The accuracy of pressure, temperature, and practical salinity data is within ± 0.5 dbar, $\pm 2 \times 10^{-3}$ °C, and $\pm 3 \times 10^{-3}$, respectively. Standard SBE Data Processing software was used for the processing of CTD data.

Apart from the shipboard SBE CTD system, CYD profiles in the Barents Sea were acquired using the MSS profiler (section 3.1.3). The inclusion of CTD profiles from the MSS enriched the hydrographic measurements conducted during the cruises. Post-processing of the MSS CTD profiles involved correction against the ship CTD by applying relevant offsets when necessary. The most significant salinity offset applied was 0.018. These profiles can be accessed through Fer et al. (2023a,c,b).

Conservative Temperature, Θ , and Absolute Salinity, S_A , were calculated using the thermodynamic equation of seawater (IOC et al., 2010), and the Gibbs SeaWater Oceanographic Toolbox (McDougall and Barker, 2011).

3.1.5 Current Profiles From Cruises

Current profiles were obtained using acoustic Doppler current profilers (ADCPs) in two distinct configurations: ship-mounted ADCP (SADCP) for continuous measurements and ADCP systems integrated into the CTD frames (lowered-ADCP, LADCP) for station-based measurements. The CTD frames on all vessels were outfitted with a pair of 300 kHz Teledyne RD Instruments (RDI) Sentinel Workhorses, with one oriented downward and the other upward. The LADCPs were synchronized and configured to provide vertically averaged data in 8 m bins. Compasses were duly calibrated, resulting in errors of less than 5°. The LADCP data underwent processing using the LDEO software version IX-13 (Visbeck, 2002). The LADCP

profiles were constrained using navigation data, bottom-tracking by the downward pointing ADCP, and the current profiles extracted from the SADCPS.

All research vessels were equipped with Teledyne RDI Ocean Surveyor SADCPS, which operated at different acoustic frequencies. RV *Kronprins Haakon* was equipped with four SADCPS – two operating at 38 kHz acoustic frequency and two at 150 kHz. One of each frequency was mounted on a drop keel, while the other two were flush-mounted in the hull to ensure protection when navigating through ice. From RV *Kristine Bonnevie*, we utilized the current profiles obtained by the 150 kHz SADCPS, while from RV G. O. SARS, we utilized the 75 kHz SADCPS. The 150 kHz SADCPS collected profiles with a bin size of 4 m, utilizing the narrowband mode for optimal range. The 75 kHz and 38 kHz SADCPS measured profiles with an 8 m bin size. The SADCPS data were collected using either the onboard VmDAS software or the University of Hawaii data acquisition software, depending on the specific vessel. Subsequently, post-processing was conducted using the University of Hawaii CODAS software, with an uncertainty level of 2–3 cm s⁻¹ (Firing and Ranada, 1995).

In addition to the current measurements collected during the cruises described in this study, we have integrated SADCPS data from 5 additional cruises conducted in the Barents Sea region during the fall and winter seasons (August to February) between 2018 and 2020. For more comprehensive information regarding the SADCPS data acquired from these supplementary cruises, readers are directed to Cannaby et al. (2022).

3.1.6 Historical data

Historical data in the study regions were obtained from the UNIS hydrographic database (UNIS HD; (Skogseth et al., 2019)). This dataset is a collection of temperature and salinity profiles from the area spanning 0-34°E and 75-83°N. Prior to analysis, duplicate data points and outliers were removed. Note that UNIS HD also encompasses data extracted from various other data sources. For more information regarding the primary data contributors to UNIS HD, readers are referred to Skogseth et al. (2019).

3.1.7 NORA10

Wind speed and direction at a height of 10 meters above sea level were extracted at hourly intervals from the area north of Svalbard (0 - 35°E, 79°N - 83°N) using data from the Norwegian Reanalysis Archive (NORA10; Reistad et al. (2011)). NORA10 is a regional high-resolution dataset (with a resolution of 10-11 km) obtained through atmospheric downscaling of ERA-40 (Uppala et al., 2005) and ECMWF IFS (European Center for Medium-Range Weather Forecasts Integrated Forecasting System) operational analyses (after 2002). It covers the northern North Atlantic and the Barents Sea. This dynamic atmospheric downscaling involves a series of short prognostic runs using the High-Resolution Limited Area Model. These runs are ini-

tialized from a blend of ERA-40 and the previous prognostic run, which aims to preserve the fine-scale surface features from the high-resolution model while maintaining the large-scale synoptic field from ERA-40. We calculated both the wind stress components, using the parameterization proposed by Large and Pond (1981), and the wind stress curl over the specified region.

3.2 Methods

3.2.1 Water masses

The water masses considered in this study differ between the Barents Sea region and the region north of Svalbard. The specific water masses used are outlined in Table 3.2. For the area north of Svalbard, we utilize Atlantic Water (AW) as defined by Swift and Aagaard (1981). Additionally, we consider Arctic Intermediate Water, Cold Norwegian Sea Deep Water, and Eurasian Basin Deep Water following the classification by Schlichtholz and Houssais (2002).

Regarding the Barents Sea region, our classification is largely consistent with that proposed by Sundfjord et al. (2020). The definitions we adopt from Sundfjord et al. (2020) are based on established water mass classifications from previous literature, including sources such as Lind et al. (2018); Loeng (1991); Rudels et al. (2005). We have made a slight adjustment to the definition of warm Polar Water (wPW). Specifically, we consider only waters with a potential density anomaly (σ_0) greater than 27.8 kg m^{-3} for inclusion in the wPW category. This modification is intended to capture wPW as a mixture of AW and PW, while excluding surface waters that are more influenced by seasonal processes such as atmospheric heating and ice melting. Instead, we name the wPW with $\sigma_0 < 27.8 \text{ kg m}^{-3}$ as Surface Water (SW).

3.2.2 Detiding current measurements

Current profile measurements from LADCPs and SADCPs, and DAC from the gliders were detided. Barotropic tidal currents, at the time and location of the LADCP and SADCP measurement were obtained using the 2018 version of the Arctic Ocean Inverse Tidal Model on a 5 km grid (Arc5km2018) (Padman and Erofeeva, 2004). The barotropic tidal components were subtracted from the measured currents.

Detiding of the DAC measured by the Seaglider needs care because one dive-climb cycle may take several hours depending on the vertical velocity of the glider and the depth of the dive. For the glider mission north of Svalbard, we estimated the average tidal current during the dive-climb cycle. Based on the Seaglider flight model, latitude, longitude and time stamps were estimated for every decibar during the dive-climb cycle. These values were used as input to predict the barotropic tidal transport at a given time and location at each depth level. We calculated the average tidal current during profiling and subtracted it from the Seaglider's

Table 3.2: Water mass definitions used in the region north of Svalbard and in the Barents Sea following Swift and Aagaard (1981); Schlichholz and Houssais (2002); Sundfjord et al. (2020), using Conservative Temperature, Θ , Absolute Salinity, S_A , and potential density anomaly, σ_0 . Note that our definition of the warm Polar Water, only includes waters with $\sigma_0 > 27.8 \text{ kg m}^{-3}$ in order to separate Surface Water from the wPW.

Water mass	Θ ($^{\circ}\text{C}$)	S_A (g kg^{-1})	σ_0 (kg m^{-3})
North of Svalbard			
Atlantic Water (AW)	$\Theta \geq 2$	$S_A \geq 35.05$	
Arctic Intermediate Water (AIW)	$-0.8 \leq \Theta < 0$	$35.06 < S_A < 35.09$	
cold Norwegian Sea Deep Water	$-1.1 \leq \Theta < -0.8$	$35.06 < S_A < 35.09$	
Eurasian Basin Deep Water	$-1.1 \leq \Theta < -0.8$	$S_A > 35.09$	
Barents Sea			
Atlantic Water (AW)	$\Theta \geq 2$	$S_A \geq 35.06$	
Polar Water (PW)	$\Theta < 0$		$\sigma_0 < 27.97$
warm Polar Water (wPW)	$\Theta \geq 0$	$S_A < 35.06$	$\sigma_0 \geq 27.8$
Surface Water (SW)	$\Theta \geq 0$	$S_A < 35.06$	$\sigma_0 < 27.8$
modified Atlantic Water (mAW)	$0 \leq \Theta < 2$	$S_A \geq 35.06$	
Intermediate Water (IW)	$-1.1 \leq \Theta < 0$		$\sigma_0 \geq 27.97$
cold Barents Sea Dense Water	$\Theta < -1.1$		$\sigma_0 \geq 27.97$

depth average current.

On the other hand, a typical glider dive in the Barents Sea lasted for about an hour and covered about 1 km horizontal distance. To remove the barotropic tide from DAC in the Barents Sea, we interpolated the DAC time series to hourly intervals and used a 24 h low pass filter.

3.2.3 Objective interpolation of depth average currents

Glider DAC and depth-averaged currents from the SADCP and LADCP were bin-averaged in 3 km by 3 km and 10 km by 10 km horizontal bins for the region north of Svalbard and in the Barents Sea, respectively. The reason for using a different bin size north of Svalbard vs. in the Barents Sea is that the boundary current north of Svalbard is more strictly confined to the continental slope. In the Barents Sea, where the topography is relatively flat, the currents meander more.

Care must be taken to avoid unrealistic diverging or converging flows in the objectively interpolated fields of depth-averaged ocean currents. In the Barents Sea we constrained the interpolated fields to be divergence-free and applied a horizontal correlation length scale of 50 km, obtained from variogram analysis of the depth average currents. Variogram analysis calculates the variance in the difference between data points as a function of the distance between the data points. The correlation length scale is then set at the distance where the variance ceases to increase. More details on variogram analysis are given in the appendix of Kolås et al. (2020). In the region north of Svalbard, we did not constrain the fields to be divergence

free, instead we used a covariance function depending on the spatial distance between binned observations and the fractional distance to largescale barotropic potential vorticity (f/H) contours. That is, we assume the along-isobath variability (following the current) is less than the across-isobath variability.

3.2.4 Synoptic and Composite sections

As the gliders do not necessarily follow a straight line, producing synoptic sections across currents is not trivial. For the boundary current following the continental slope north of Svalbard, we defined target sections along a line normal to the 800 m isobath close to the profile locations. Using ocean depth obtained from the International Bathymetric Chart of the Arctic Ocean (IBCAO) (Jakobsson et al., 2020), we moved each profile along isobaths onto the corresponding section, thus assuming topographic steering. The current vectors u , v (east, north) were rotated to obtain along isobath velocity u_r (> 0 eastward) and across isobath velocity v_r (> 0 toward deep water), relative to the local 800 m isobath's orientation at the corresponding section. Seaglider data were horizontally averaged in 2 km bins before interpolating onto a $2 \text{ m} \times 1 \text{ km}$ grid (vertical \times horizontal). We used a Laplacian spline interpolation method with tension, choosing a 15 km search radius and no smoothing (Smith and Wessel, 1990; Pickart and Smethie, 1998). Finally, all sections were smoothed using a $20 \text{ m} \times 20 \text{ km}$ moving average window to remove small-scale variability.

Similarly, composite sections across the boundary current north of Svalbard were compiled by moving all profiles (shipboard and glider data) along isobaths onto an average bathymetry representative of the study region across the continental slope. The average seafloor profile is produced as described in Appendix A in Kolås et al. (2020).

In the Barents Sea, composite sections were generated for predefined target sections along which we have focused our data sampling. For every data point (all Θ and S_A profiles, and SADCP and glider DAC), an incrementally increasing search radius of 5, 10, 20 and 30 km was used to look for predefined grid points along the target section. When two or more grid points were within the search radius of a data point, the data point was moved along isobaths onto the section, again assuming topographic steering. Θ and S_A profiles along the section were bin-averaged over 5 km horizontal and 10 m vertical bins before objectively mapping onto a 1 km by 5 m grid (horizontal by vertical). Historical CTD profiles (station data) were averaged over 5 km horizontal and 20 m vertical bins before objectively mapping onto a 1 km by 5 m grid.

Relative geostrophic velocity was obtained for each of the synoptic and composite sections using the dynamic height anomaly referenced to the surface pressure from Gibbs SeaWater Oceanographic Toolbox (McDougall and Barker, 2011). Absolute geostrophic velocities were obtained by vertically integrating the geostrophic shear and constraining its depth average by the across-section (typically along isobath) component of the observed depth-averaged current.

3.2.5 Objectively interpolated horizontal layers

Objectively mapped horizontal fields of Θ and S_A for different depth-layers and different time periods were produced for the Barents Sea region using the recent and historical CTD profiles. Individual profiles were vertically averaged over the desired layer depth, before bin-averaging over 10 km by 10 km horizontal bins. To ensure that the vertically averaged values were representative of the layer, thresholds were set on the minimum amount of data points averaged, and the average depth of the data points compared to the middle depth of the layer. For the 50-100 m layer, a minimum of 5 data points with average depths within 15 m of the middle depth of the layer were required. Horizontal correlation length scales were set to 60 km and the final gridded product had a 2 km resolution.

3.2.6 Along-path rate of change of heat content

In our analysis north of Svalbard, we estimate the along-path heat loss of the AW inflow by comparing the integrated heat content of AW from one cross-slope section to next further downstream. As shown in IOC et al. (2010); McDougall (2003), the first law of thermodynamics is practically equivalent to the conservation equation for Conservative Temperature (Θ), which is proportional to potential enthalpy, h_0 , as $\Theta = h_0/C_p$. The heat content per unit mass of seawater is then $C_p\Theta$. Finally, heat content is integrated laterally and vertically in the cross-slope region, to obtain total heat content per downstream meter.

The calculation of the heat loss between sections using the rate of change in heat content requires that the volume transport is conserved (Schauer and Beszczynska-Möller, 2009). For each synoptic section north of Svalbard, we therefore defined a stream tube conserving a specified volume transport of AW, representative of the core of the current. For each stream tube, we calculated velocity-weighted average Θ and S_A , and average u_r .

The along-path rate of change of heat content calculation is based on the methods described by Boyd and D'Asaro (1994) and Cokelet et al. (2008), assuming only the eddy fluxes at the surface are important, and neglecting thermal inertia and local advection of heat. Then all observed heat loss, Q , must be due to heat fluxes through the surface of our stream tubes. Applying Gauss theorem on the volume integral of the heat advection (see e.g. Schauer and Beszczynska-Möller, 2009), yields

$$\int_{Surface} Q \, dx dy = \rho C_p \bar{u} \int_A \frac{\partial \Theta}{\partial y} \, dx dz, \quad (3.1)$$

where the area integral is taken over the stream tube's cross-section A , \bar{u} is the mean u_r (along-isobath velocity), and ρ is the reference seawater density. Here, y is the along-path coordinate, and estimated as the distance between the sections along the 800-m isobath north of Svalbard. The along-path temperature gradient was obtained from the slope of a line fit to along-path dis-

tance against the velocity-weighted average Θ for each section. The advected area-integrated heat content change per along-path meter (W m^{-1}) from Eq. 3.1 was divided by the average width of the stream tube to obtain the surface heat flux (W m^{-2}).

3.2.7 Barents Sea Polar Front position

The position of the Barents Sea PF is determined following the method described by Oziel et al. (2016). Oziel et al. (2016) calculated two different fronts, a northern and a southern front based on the temperature and salinity fields, respectively. In our study, we focus only on the position of the northern front obtained from the temperature field. To achieve this, we create a horizontally mapped field by combining all available temperature (Θ) data for the 50-100 m layer, including both historical and recent data, using the method described in Section 3.2.5. Subsequently, we calculate the absolute temperature gradients across this field. We then construct a histogram with 0.05°C bins of the Θ values where the temperature gradient exceeds $0.06^\circ\text{C km}^{-1}$. The PF is then defined as the isotherm corresponding to the modal value of the histogram, here equal to the 0.1°C isotherm, with one standard deviation of 0.4°C . While the modal value is somewhat sensitive to the lower temperature gradient limit, the position of the front along Section B varies less than 15 km, within $\pm 0.4^\circ\text{C}$ (one standard deviation).

3.2.8 Turbulence measurements

When processing the shear probe data to estimate dissipation rates, we follow the guidelines and recommendations by the Scientific Committee on Oceanic Research working group on analysing ocean turbulence observations to quantify mixing (ATOMIX) <https://wiki.app.uib.no/atomix>. When the shear probe travels through the water along axis x , at speed U , then the voltage E_p produced by the probe in response to a cross-axis velocity v is given by

$$E_p = 2\sqrt{2}\hat{s}Uv, \quad (3.2)$$

where the constant \hat{s} is the sensitivity of the probe which must be determined by calibration (Lueck et al., 2002). The probe voltage is then converted to shear, $\partial v/\partial x$, in physical units as

$$\frac{\partial v}{\partial x} = \frac{1}{U} \frac{\partial v}{\partial t} = \frac{1}{2\sqrt{2}\hat{s}U^2} \frac{dE_p}{dt}, \quad (3.3)$$

by using the known sensitivity of the shear probe and the travel speed of the instrument (Lueck et al., 2002). A second probe oriented orthogonal to the first one similarly measures $\partial w/\partial x$. For the LAUV, the travel speed, U , is measured by the instrument, while for *Odin* it is inferred from the hydrodynamical flight model. For vertical profiling with the MSS, the instrument speed is calculated from the smoothed rate-of-change of pressure, obtaining the sinking velocity W . In the vertically profiling case we measure the $\partial(u, v)/\partial z$.

Shear spectra are used to estimate the dissipation rate of turbulent kinetic energy, ε . The time series from each shear probe was segmented into half-overlapping portions. The segment length, which differed depending on the platform, was 8 s, 10 s and 6 s for the LAUV, *Odin* and MSS, respectively. Next, a fast Fourier transformation (FFT) length corresponding to 1 s was chosen for the LAUV and 2 s for *Odin* and the MSS. Each half-overlapping FFT segment was detrended and smoothed using a Hanning window, before averaging them to get the shear frequency spectrum for each segment.

Shear spectra were converted from frequency, f , domain to wavenumber, k , domain using Taylor's frozen turbulence hypothesis and the platform speed through water, U , as $k = f/U$. For additional cleaning of the shear data, the shear spectrum signal coherent with the accelerometer spectrum signal from the instrument was removed using the method described by Goodman et al. (2006). For the MR data, two orthogonal vibration sensors are used in the Goodman method, while for the MSS only one vibration sensor is available (a body acceleration sensor). Bias induced by the Goodman method is corrected for.

The dissipation rate is proportional to the variance of shear contained at scales from $\mathcal{O}(1)$ m to $\mathcal{O}(10^{-2})$ m. Assuming isotropic turbulence, ε was calculated for each segment by integrating the cleaned wavenumber spectrum, $\Psi(k)$ as

$$\varepsilon = \frac{15}{2} \nu \overline{\left(\frac{\partial v}{\partial x}\right)^2} = \frac{15}{2} \nu \int_0^\infty \Psi(k) dk \approx \frac{15}{2} \nu \int_{k_1}^{k_u} \Psi(k) dk \quad (3.4)$$

where ν is the kinematic viscosity and overbar denotes averaging in time (e.g., Fer et al., 2014). The lower (k_1) integration limit is determined by the wavenumber corresponding to the FFT length, and the upper ($k_u < \infty$) integration limit is usually determined from a minimum in a low-order polynomial fit to the wavenumber spectrum in log-log space. Typically electronic noise takes over after the minimum in the spectrum. To account for the variance in the unresolved part of the spectrum (integration outside the k_1 and k_u limits), the empirical model for turbulence spectrum determined by Nasmyth (1970) was used for the data collected by the LAUV, and the model spectrum of Lueck (2022) was used for the data collected by *Odin* and the MSS. The model spectrum of Lueck (2022) is similar to the empirical Nasmyth spectrum (Nasmyth, 1970), but is a better-constrained approximation. A final quality screening is done by comparing the measured spectrum to the model spectrum, and the measured spectrum is flagged as bad if the two differ by more than 15%. When using two shear probes, the dissipation rate in the segment is calculated as the average of the values from both sensors.

Chapter 4

Summary of the scientific results

Paper I: Structure and Transport of Atlantic Water North of Svalbard From Observations in Summer and Fall 2018

Eivind Hugaas Kolås, Zoé Koenig, Ilker Fer, Frank Nilsen and Marika Marnela (2020), Journal of Geophysical Research: Oceans, 125(e2020JC016174), <https://doi.org/10.1029/2020JC016174>.

This paper addressed the research questions: How is the structure of the AW inflow along the boundary slope north of Svalbard? What is the short-term and intraseasonal variability of the AW boundary current, and what is forcing this variability? (Section 1.3)

We conducted a comprehensive analysis of hydrographic and current observations gathered from two scientific cruises, a Seaglider mission and two Argo floats during the summer and fall of 2018 in the region north of Svalbard (between 12°E and 24°E). Our investigation involved presenting the collected data as synoptic sections, composite sections, and depth-averaged currents. This approach allowed us to explore and understand short-term variability, intraseasonal variations, and the broader circulation patterns.

We proposed an AW circulation pattern as illustrated in Figure 4.1a. The observed AW boundary current flowed into the Arctic following the 800 m isobath. Adjacent to the AW boundary current, we identified an AW recirculation within the Sofia Deep. This recirculation encompassed a separate patch of AW overlaying an eastward-flowing, bottom-intensified current. The arrangement of the boundary current, the reverse AW flow, and the bottom-intensified current are depicted in Figure 4.1b and c.

The behavior of the boundary current north of Svalbard, specifically between 12°E and 24°E, is highly variable in both time and space. Our observations documented an average AW transport of 2.6 ± 0.2 Sv into the Arctic. Notably, the AW transport exhibited a seasonal variation, increasing from 2.0 ± 0.1 Sv in summer to 3.0 ± 0.2 Sv in fall, with a peak in October. Furthermore, we noted substantial short-term fluctuations; over a mere five days, the AW transport surged from 1.9 to 3.5 Sv. This rapid change was attributed to a sudden shift in wind stress curl ($\nabla \times \tau$) within the Sofia Deep, transitioning from negative to positive and

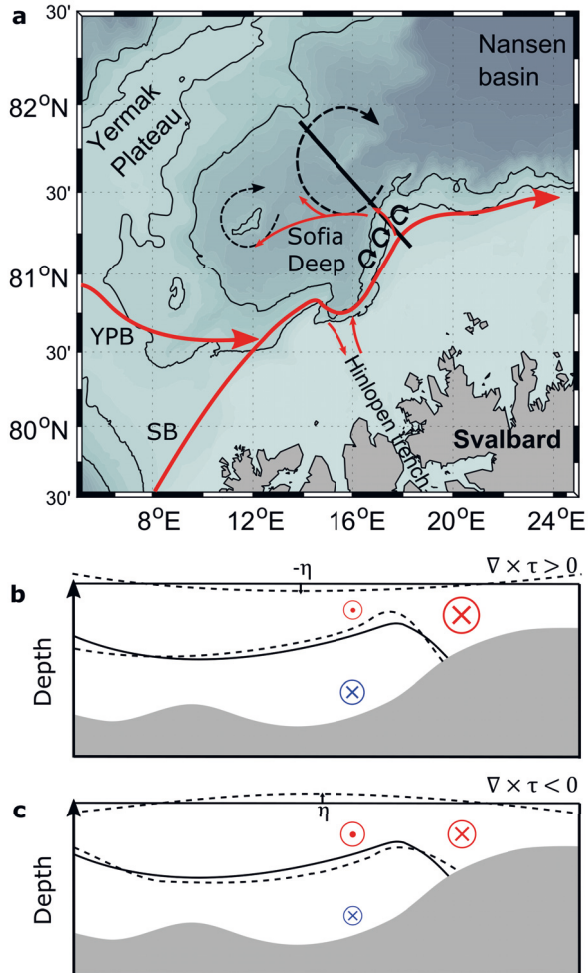


Figure 4.1: Figure from Kolås et al. (2020). (a) Red arrows show the AW circulation in the study region north of Svalbard. Black dashed arrows show possible anticyclonic circulation in the Sofia Deep. Small black arrows mark the possible generation site for eddies. The black line is the transect sketched in (b) and (c). Response of the circulation strength, sea level, and interface between the Atlantic Water and deeper water masses, to (b) a positive and (c) a negative wind stress curl in the Sofia Deep. For (b) and (c), solid line is the normal state, dashed line is perturbation from the wind stress curl.

consequently strengthening the AW boundary current.

Figures 4.1b and c illustrate the probable responses to anomalous wind stress curl events within the Sofia Deep. A negative $\nabla \times \tau$ event (Figure 4.1c) within the Sofia Deep weakens the AW boundary current through geostrophic set-up effects, potentially enabling it to overcome the boundary current and instigate a reversal on the shelf. On the other hand, a positive $\nabla \times \tau$ event (Figure 4.1b) triggers the opposite response, intensifying the boundary current and amplifying its transport.

Furthermore, the wind forcing likely affects the intensity of the return flow and the bottom-intensified flow, mirroring its impact on the boundary current. Alongside transient geostrophic set-up effects, an extended wind stress curl event in the Sofia Deep could lead to upwelling or downwelling along the continental slope. This, in turn, would modulate the isopycnal gradient and influence the strength of the bottom-intensified current (Figures 4.1b and c).

Lastly, we note that the continental slope around 18°E north of Svalbard is a probable generation site for eddies. These eddies detach from the boundary current and migrate into the Sofia Deep. Signatures of multiple eddies were found along the Seaglider transect that crossed the Sofia Deep. Our observations suggest an average anticyclonic circulation within the Sofia Deep, possibly around each of the seamounts. However, the mechanisms maintaining this anticyclonic circulation remain unclear and warrant further investigation.

Paper II: Technical note: Turbulence measurements from a light autonomous underwater vehicle

Eivind Hugaas Kolås, Tore Mo-Bjørkelund and Ilker Fer (2022), Ocean Science, 18(389-400), <https://doi.org/10.5194/os-18-389-2022>.

This paper addressed the research questions: Can a propeller-driven lightweight AUV carry turbulence probes, serving as a low-noise platform that does not contaminate the microstructure measurements? If so, what dissipation levels can this setup resolve? Can it operate in the open sea within Arctic waters? (see Section 1.3)

A turbulence instrument is modified to collect measurements under conditions of relatively large flow speed imposed by the propeller-driven light AUV (*Harald*). The turbulence package was mounted below *Harald* and tested in the Barents Sea during a cruise in February 2021. *Harald* conducted three transects across a surface temperature front at 11, 21 and 31 m depth, while continuously sampling microstructure shear. The experiment was designed to run an algorithm to automatically follow a temperature front, aimed at providing more efficient coverage relative to shipboard sampling. Microstructure measurements from such missions are highly useful and demanded to obtain turbulent fluxes of heat and solutes and to describe the turbulent mixing processes. Yet, applicability and limitations of shear probe measurements from a lightweight AUV has not been demonstrated.

The positioning of the MR below the nose of *Harald* was not ideal, causing additional variability in roll, pitch and yaw, and reduced the maneuverability of *Harald*. AUV maneuverability is critical in confined spaces or near potential hazardous environment such as sea ice. Hence the mission location was chosen to be a surface temperature front in the open sea away from potential obstacles.

The propulsion system of *Harald* was set to operate at a constant RPM (rotations per minute) of 1500, corresponding to 25 Hz. Both the vehicle motion and vibrations from the propulsion system were detected by the microstructure sensors. The shear spectra were significantly contaminated in the 10–30 Hz band and in narrow bands centered at integers of 25 Hz. The peaks at 25 Hz (and the higher harmonics) came from the propeller while the contamination in the 10–30 Hz band likely came from roll, pitch and, yaw.

Although the vehicle motion and propulsion vibrations of Harald contaminated the shear probe records, the shear spectra for dissipation levels above $5 \times 10^{-8} \text{ W kg}^{-1}$ were sufficiently cleaned using the Goodman method (Goodman et al., 2006). However, the overall noise level due to contamination from Harald was quite large. We conclude that this setup cannot detect dissipation rates below $5 \times 10^{-8} \text{ W kg}^{-1}$ reliably and is unfit for use in quiescent boundary layers.

However, an improved installation of the turbulence probes could reduce some of the limitations reported in this study, and allow acceptable quality dissipation measurements from light AUVs in relatively quiet environments. A better installation would be to implement the MR into the wet-section, the nose, of the light AUV, reducing the drag and resulting in a better balanced vehicle, potentially significantly reducing the variability in roll, pitch and yaw.

Paper III: Circulation and hydrography in the northwestern Barents Sea: insights from recent observations and historical data (1950–2022)

Eivind Hugaas Kolås, Till M. Baumann, Ragnheid Skogseth, Zoé Koenig, Ilker Fer

This paper addressed the research questions: What is the volume transport and structure of the different AW branches in the northwestern Barents Sea? How much AW reaches the Polar Front and how much Atlantic-origin water is able to cross the front? How do the AW properties in the northwestern Barents Sea between 2018 and 2022 compare to historical observations?

This study investigates the characteristics and dynamics of the AW and PW in the northwestern Barents Sea. Observations from three scientific cruises and nine glider missions conducted in the Barents Sea between 2019 and 2022 are synthesized to describe the present conditions. In addition, historical data collected after 1950 are averaged over decades and compared to recent observations.

We present detailed circulation pathways of Atlantic- and Polar-origin waters in a region essential for water mass transformation and poleward transport of heat and salt (Figure 3.6).

0.9 ± 0.1 Sv of Atlantic-origin water reaches the Hopen Trench between Spitsbergen Bank and Central Bank. This is about half of the AW inflow through the BSO. The AW inflow into the Hopen trench bifurcates; one branch flowing east along the Persey Trench and one continuing north along the Hopen Trench. Each of the two branches transport about 0.5 Sv of Atlantic-origin waters. At the northern edge of the Hopen Trench, AW eventually subducts under the PW and the PF, continuing northward along the eastern slope of the Olga Basin as a topographically steered current.

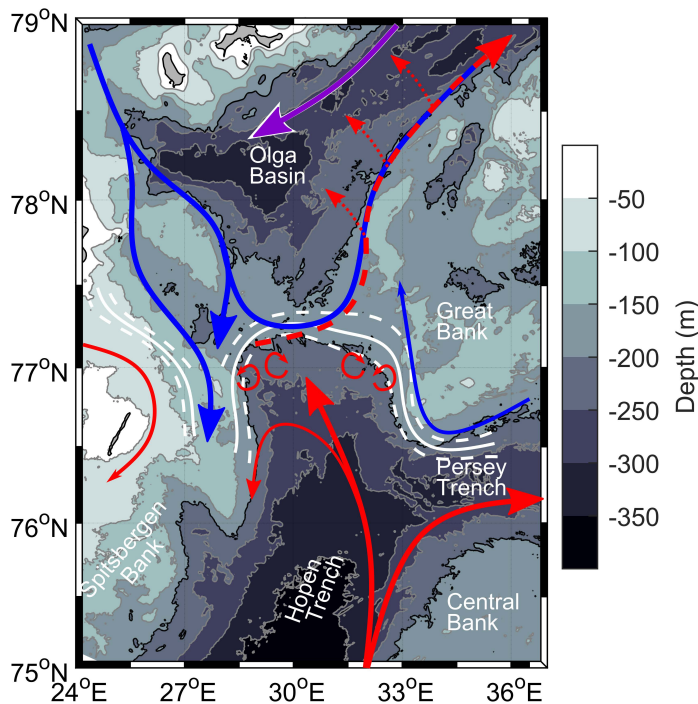


Figure 4.2: Figure from (Kolås et al., 2023, preprint). Mean currents of Atlantic Water (red) and Polar Water (blue) in our study region, as inferred from our observations between 2019 and 2022. Red dashed line indicates subducted Atlantic-origin waters. Purple line is PW that is relatively warmer than PW in the west, due to mixing with AW inflow. White solid line marks the mean position of the polar front based on historical and recent data, with the white dashed lines indicating one standard deviation.

PW enters the Olga Basin from the northeast and northwest (Figure 4.2). These two branches are of similar magnitude as the AW inflow, transporting 0.5 Sv each. The northwestern branch is the colder one, containing PW of lower temperature than the northeastern branch. The difference in heat content between the two branches is due to recirculating AW within the eastern Olga Basin, and AW entering from the north (Lundesgaard et al., 2022).

The AW is undergoing continuous modifications along its pathway. Upstream of the Hopen Trench, AW transformation is primarily influenced by cooling from the atmosphere, while along the Hopen Trench and Persey Trench the transformation is mainly driven by mixing between AW and PW.

We observe a 0.7°C warming of the AW inflow between 1980 and 2010 south of the PF. As a result, the Atlantic-origin water reaching the polar front in recent years is less modified compared to previous decades, and the 100–180 m layer-average temperature gradient across the PF has increased from $1.8^{\circ}\text{C}/100\text{ km}$ to $2.8^{\circ}\text{C}/100\text{ km}$ between the 80s and the 2019–2022 period. Consequently, the layer-average density gradient across the PF was reduced from $0.25\text{ kg m}^{-3}/100\text{ km}$ to $0.14\text{ kg m}^{-3}/100\text{ km}$ in the same period.

We hypothesize that the amount of warm water crossing the PF and the topographic sill separating AW from PW is regulated by the density difference between AW south of the sill and PW in the Olga Basin. Our observations indicate that the Olga Basin cooled from the 90s to the 2000s even though the AW temperature south of the sill continued to increase. This was likely a result of denser waters residing in the Olga Basin due to increased salinity.

Our recent observations show that the salinity of the AW inflow reduced by nearly 0.1 g kg^{-1} from the 2000s to the 2019–2022 period, reducing the AW density south of the PF by as much as 0.05 kg m^{-3} . As a result, less Atlantic-originating water flowed into the Olga Basin, and the average temperature below 100 m depth in the Olga Basin continued to cool. In addition, mixing of relatively less dense AW with PW produced less dense water in the 2019–2022 period compared to previous decades, which has potential far-reaching consequences for the general dense water production in the Barents Sea.

Paper IV: The Polar Front in the northwestern Barents Sea: structure, variability and mixing

Eivind Hugaas Kolås, Ilker Fer and Till M. Baumann

This paper addressed the research questions: How is the Polar Front structure on the sill between the Hopen Trench and Olga Basin in the northwestern Barents Sea, and how does this structure compare to the Polar Front elsewhere in the western Barents Sea? What is the short term and seasonal variability of the frontal structure at this location, and what are the drivers of this variability? What are the main mixing processes occurring across the front at this location?

This study provides insights into the dynamics and hydrography of the Barents Sea Polar Front within the region bounded by the Hopen Trench and Olga Basin in the Barents Sea (see Figure 4.2 for location of geographic names). The topographic sill separating the Hopen Trench from the Olga Basin is a location where AW meets PW setting up a front where AW eventually subducts below the PW. The data presented herein was collected during two scientific cruises in October 2020 and February 2021, as well as four glider missions spanning 2019 to 2021.

During the fall cruise, the western Barents Sea was devoid of sea ice, with sea surface temperatures mainly exceeding 0°C . In February however, the northwestern Barents Sea and

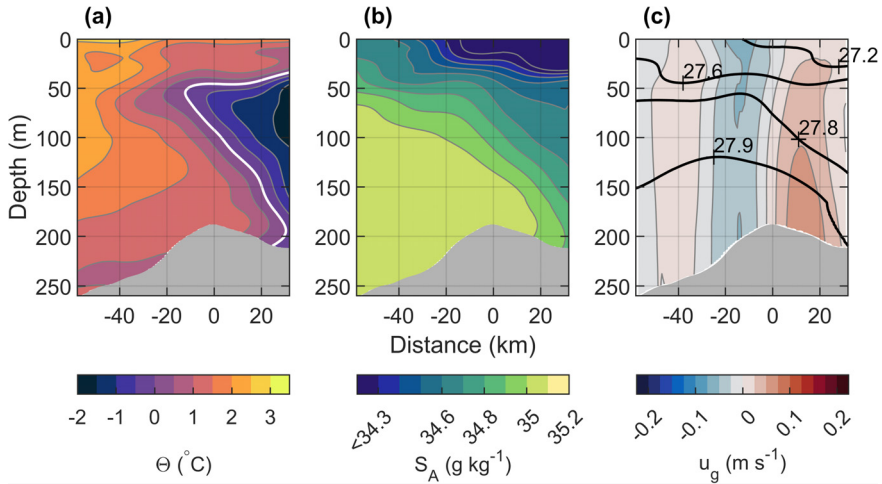


Figure 4.3: Composite section combining all hydrography and current data from the individual ship and glider transects. (a) Conservative Temperature, Θ , (b) Absolute Salinity, S_A , and (c) absolute geostrophic velocity, u_g . Positive values of u_g are eastward. The white line in (a) is the 0°C isotherm, indicating the center of the Polar Front when below 50 m depth. Black contours in (c) show isopycnals.

the sill separating the Hopen Trench and the Olga Basin were covered by sea ice, with the 0°C isotherm aligning closely with the 200m isobath. Despite the seasonal changes at the surface and in the surface mixed layer, the influence of the AW inflow near the seabed over the sill remained unperturbed.

This study shows that the PF over the sill is a distinct baroclinic front supporting an eastward geostrophic current above the sill (Figure 4.3). The average eastward transport of this current is estimated to 0.3 ± 0.2 Sv, where ± 0.2 denotes the standard deviation over 16 repeat transects. The baroclinic front differs markedly from prior observations along the Spitsbergen and Great Banks slopes, where a barotropic front with horizontal density lines was typically noted. The distinction arises from variations in bathymetry, as the absence of a topographic boundary permits a geostrophic adjustment to balance inflowing AW and overlying PW.

The upper layers of the PF (0–100 m) experienced pronounced seasonal fluctuations, influenced by atmospheric heating, sea ice formation, and brine rejection. However, the position of the front beneath 100 m depth exhibited minimal seasonal variability.

Short-term variability stemmed from tidal currents and mesoscale eddies. Tidal currents induced 2–4 km north-south displacement of water masses, especially notable when the subsurface temperature front was approximately vertical. However, the modification of the PF by tidal currents was negligible compared to the effects of mesoscale eddies. Signatures of two eddies were observed in our transects collected from ships and gliders during October and November 2020. Satellite data provide independent evidence supporting the presence of the eddies. These eddies influenced the front's structure, shifting the position of the front as much as 25 km in less than 4 days. In addition, the isopycnal slope across the front was markedly re-

duced after the passage of an eddy, suggesting the eddy reduced the available potential energy of the front during its traversing of the front. Simultaneously, as the eddy approached the front, satellite derived sea level anomalies showed the eddy's radial velocity increasing, suggesting the available potential energy was converted to eddy kinetic energy.

Microstructure measurements show intense mixing within the surface boundary layer, particularly in the upper 60 m. During winter, this mixing extended occasionally to 100 m. Below the surface layer, significant mixing was concentrated in the bottom boundary layer, and linked to the tidal oscillations across the sill. Nevertheless, we observe substantial water mass transformation across the front, which is likely a result of eddy driven along isopycnal mixing.

This study offers a comprehensive description of the Barents Sea Polar Front, shedding light on its interactions with seasonal shifts, tidal currents, and mesoscale eddies. The distinctive baroclinic structure observed across the topographic sill underscores the importance of local bathymetry in shaping front dynamics.

Chapter 5

Conclusions

5.1 Main takeaways

In this observational study, we delved into the ocean dynamics in two key regions of the Arctic Ocean; the northwestern Barents Sea and the continental shelf break north of Svalbard. Our focus is on the AW inflow into these key regions, analysing hydrographic, current and microstructure data collected during several scientific cruises and multiple AUV missions between 2018 and 2022. The vast majority of the hydrographic data collected and presented herein, more than 13,000 CTD profiles, comes from AUVs, and provides detailed insight into water mass properties, their variability, and the AW pathways into the Arctic Ocean.

North of Svalbard, we conducted several transects across the continental slope between 12°E to 24°E during summer and fall of 2018. The AW boundary current, following the 800 m isobath eastward along the continental slope, had an average volume transport of 2.6 ± 0.2 Sv. The short-term variability was large, at one point exceeding 1.5 Sv in less than five days. The large short-term variability was linked to the changing wind stress curl driving rapid shifts in AW transport. Furthermore, we identified an intriguing AW recirculation pattern within the Sofia Deep, overlaying an eastward-flowing, colder bottom-intensified current, both of which have not been previously described. We hypothesize that the wind stress curl plays a crucial role in regulating the strength of both the recirculation branch and the bottom-intensified current. These dynamics underscore the importance of wind-driven processes in shaping the region's circulation patterns.

In the northwestern Barents Sea, we conducted several transects across the main topographic depressions south of the PF. Integrating recent data from cruises and glider missions with available observations dating back to 1950, we discern circulation patterns and quantify volume transport in the region, and discuss the characteristics of water masses and their changes in the last 70 years.

Around 0.9 Sv of AW enters through the Hopen Trench, bifurcating into branches along the Persey and Hopen Trenches. At the northern end of the Hopen Trench AW meets PW

establishing the Barents Sea PF. AW continues northward underneath PW as modified water, and the AW signature can be traced northeastward along the edge of the Olga Basin. However, the amount of AW crossing the PF is likely regulated by the density difference between AW and PW. Anomalously fresh AW has entered the Barents Sea in recent years, resulting in reduced density difference between AW and PW. Subsequently, less AW was able to flow northward beneath PW in the 2019–2022 study period; instead, AW was directed eastward toward the Great Bank. Furthermore, the reduced density of the AW inflow results in a mixing product between AW and PW that is less dense than in the previous decades. A reduction in the Barents Sea dense-water production can have far reaching consequences for the circulation and ventilation of the Arctic Ocean.

The PF over the sill between Olga Basin and the Hopen Trench is identified as a distinct baroclinic front supporting an eastward geostrophic current, with an average transport of approximately 0.3 ± 0.2 Sv. While the upper layers of the PF experience pronounced seasonal changes, the position of the front below 100 m depth remains quite stationary. Short-term variability is attributed to tidal currents and mesoscale eddies, with eddies significantly influencing the front's structure. We observed an eddy causing the front to shift up to 25 km in less than 4 days. In addition, the isopycnal slope across the front was markedly reduced after the passage of an eddy, suggesting the eddy reduced the available potential energy of the front during its traversing of the front.

Microstructure measurements across the front indicate intense mixing within the surface boundary layer, occasionally extending to 100 m depth during winter, and within the bottom boundary layer. Mixing in the bottom boundary layer is linked to tidal oscillations across the sill. Nevertheless, we observe substantial water mass transformation across the front, away from the boundary layers, which is likely a result of eddy driven along isopycnal mixing.

5.2 Outlook and future perspective

One of the main objectives of this PhD study was to bridge physical oceanography and marine technology. The framework for doing so was based on collaboration between the University of Bergen and the Norwegian University of Science and Technology (NTNU). Guided by experts in their fields, this PhD study has pushed boundaries regarding the use of AUVs in Arctic condition. The focus of this study has been on the physical oceanography aspect, using data collected by AUVs. However, in parallel to this PhD study, a PhD study focusing on the technological aspect has been conducted at NTNU, and both studies have benefited vastly from close collaboration and sharing of knowledge across disciplines.

Building upon our current understanding, there are several avenues for future exploration. The continuation of comprehensive observational campaigns, relying more on advanced technologies like AUVs, can offer an even more detailed depiction of the evolving Arctic Ocean. The AUVs allow for sustained and fine-scale monitoring, capturing intricate processes that

shape the region's hydrography and circulation.

That said, the AUVs are not flawless. While ocean gliders have excellent endurance and are very cost-efficient, they move slowly (25 cm s^{-1}) and the data collected requires meticulous processing. The slow movement means their tracks can be disturbed by strong currents and target locations may not be reached. Furthermore, the slow movement means the data collected is subject to both temporal and spatial variability, and distinguishing between the two can be difficult. Nevertheless, combining AUV data with arguably more reliable ship data offers a great way to increase the data coverage at a low cost, with a relatively low carbon footprint compared to the ship.

Our study provides a stepping stone for unraveling the complexity of the Arctic Ocean's hydrography and circulation, relying heavily on AUV data. With ever-evolving technologies, the Arctic remains an intriguing frontier ripe for exploration, bearing crucial insights for understanding global ocean dynamics and climate.

Understanding ocean dynamics and ocean mixing plays an important role in understanding marine ecosystems and biology. Ocean mixing, driven by currents, tides, winds and waves, influences the distribution of nutrients, temperature, and dissolved gases in the ocean, forming the foundation for the diverse and interconnected biology within the oceans.

The well-documented Atlantification of the Arctic Ocean is causing a northward expansion of boreal species and consequently a gradual reduction of the ice-associated ecosystems (Ingvaldsen et al., 2021). The changes to the Arctic region caused by Atlantification add additional environmental stressors due to increased temperature and acidification, and have been shown to impact zooplankton communities (Espinell-Velasco et al., 2023). This prompts questions about the resilience of marine communities in view of Arctic Atlantification. The scientific communities are debating whether a reduced sea ice cover in the Arctic Ocean will lead to a reduction or an increase in the primary production (Lewis et al., 2020). However, recent observations suggest primary production in the Arctic has increased over the recent years, likely due to an influx of nutrients in the Arctic Ocean (Lewis et al., 2020). And combining observations of ocean mixing and currents to estimate nitrate fluxes has shown that nitrate fluxes across the PF are a source of nutrients in the Arctic Ocean (Koenig et al., 2023). Understanding processes in the Arctic is crucial for predicting and managing Arctic marine ecosystems, including the health and productivity of fisheries and other marine resources that sustain countless species.

In essence, delving into the complexities of ocean dynamics is key to predicting the future of marine ecosystems in the Arctic. This knowledge not only enhances our understanding of the fundamental processes governing life in the oceans but also provides valuable insights for sustainable management and conservation efforts in the face of ongoing environmental changes.

Chapter 6

Papers

Paper I

Structure and Transport of Atlantic Water North of Svalbard From Observations in Summer and Fall 2018





Eivind Hugaas Kolås, Zoé Koenig, Ilker Fer, Frank Nilsen and Marika Marnela

Journal of Geophysical Research: Oceans, **125**(e2020JC016174), 2020

<https://doi.org/10.1029/2020JC016174>

I

Structure and Transport of Atlantic Water North of Svalbard From Observations in Summer and Fall 2018

 Eivind H. Kolås¹ , Zoé Koenig^{1,2} , Ilker Fer¹ , Frank Nilsen^{3,1} , and Marika Marnela³
¹Geophysical Institute, University of Bergen and Bjerknes Center for Climate Research, Bergen, Norway, ²Norwegian Polar Institute, Tromsø, Norway, ³The University Center in Svalbard, Longyearbyen, Norway

Key Points:

- The average Atlantic Water inflow in summer and fall 2018 was 2.6 Sv, reaching 3 Sv in October
- A recirculation in the Sofia Deep transports (0.1–0.2 Sv) Atlantic Water westward
- A deep, bottom-intensified current on the lower continental slope carries cold waters into the Arctic

Correspondence to:

 E. H. Kolås,
eivind.kolas@uib.no

Citation:

 Kolås, E. H., Koenig, Z., Fer, I., Nilsen, F., & Marnela, M. (2020). Structure and transport of Atlantic Water north of Svalbard from observations in summer and fall 2018. *Journal of Geophysical Research: Oceans*, 125, e2020JC016174. <https://doi.org/10.1029/2020JC016174>

Received 21 FEB 2020

Accepted 16 AUG 2020

Accepted article online 20 AUG 2020

Abstract The transport of warm Atlantic Waters north of Svalbard is one of the major heat and salt sources to the Arctic Ocean. The circulation pathways and the associated heat transport influence the variability in the Arctic sea ice extent, the onset of freezing, and marine ecosystems. We present observations obtained from research cruises and an autonomous underwater glider mission in summer and fall 2018, to describe the hydrographic structure, volume transport, and circulation patterns of the warm Atlantic Water Boundary Current between 12°E and 24°E north of Svalbard. The Atlantic Water volume transport reaches a maximum of 3.0 ± 0.2 Sv in October, with an intraseasonal variability of 1 Sv ($1 \text{ Sv} = 10^6 \text{ m}^3 \text{ s}^{-1}$). During summer and late fall, we observed an Atlantic Water recirculation flowing westward (0.1–0.2 Sv) in the outer part of the section away from the shelf break. This counter current appears to be a part of an anticyclonic circulation in the Sofia Deep. The strength of the Atlantic Water recirculation and the Atlantic Water boundary current is very sensitive to the wind stress curl: The boundary current volume transport doubled in less than a week, corresponding to a transition from strongly negative ($-10^{-6} \text{ N m}^{-3}$) to strongly positive (10^{-6} N m^{-3}) wind stress curl over the Sofia Deep. A previously unknown, deep bottom-intensified current is observed to flow parallel to the boundary current, between the 1,500 and 2,000 m isobaths. Historical data in the region support the presence of the bottom-intensified current.

Plain Language Summary Atlantic Water enters the Arctic Ocean along two pathways, through the Barents Sea and through Fram Strait west of Svalbard. Being warmer and saltier than the Arctic Ocean, the Atlantic Water is the main heat and salt source for the Arctic Ocean. The circulation pathways and the heat transported by the Atlantic Water influence the variability of the Arctic sea ice and the marine ecosystems. We present observations from research cruises and an autonomous underwater glider mission in summer and fall 2018, to describe the Atlantic Water structure and circulation between 12°E and 24°E north of Svalbard (an extension of the Fram Strait inflow). The Atlantic Water volume transport reaches a maximum of 3.0 ± 0.2 Sv in October, with an intraseasonal variability of 1 Sv ($1 \text{ Sv} = 10^6 \text{ m}^3 \text{ s}^{-1}$). During summer and late fall, we observed Atlantic Water flowing westward (a counter current), north of the common eastward flowing Atlantic Water current. Observations suggest that the counter current is part of a clockwise circulation in the Sofia Deep, north of Svalbard. Our observations also reveal a previously undescribed deep, cold current flowing eastward into the Arctic Ocean. Historical data in the region support the presence of this deep current.

1. Introduction

In a time of decreasing sea ice volume and increasing atmospheric and oceanic temperatures in the Arctic region, understanding the processes controlling the warm water inflow into the Arctic Ocean is becoming increasingly important (Carmack et al., 2015; Polyakov et al., 2017). Relatively warm and salty waters of Atlantic origin (Atlantic Water, AW) enter the Arctic Ocean through the Barents Sea and Fram Strait. The West Spitsbergen current (WSC), located on the eastern continental slope in Fram Strait (Figure 1a), is considered the major oceanic heat source to the Arctic Ocean (Aagaard et al., 1987). However, the AW distribution and circulation in Fram Strait are complex, including multiple branches and recirculation paths (Hattermann et al., 2016; Manley, 1995; Marnela et al., 2013; von Appen et al., 2016).

The outer part of WSC recirculates, joining the East Greenland Current (Hattermann et al., 2016; Marnela et al., 2013; von Appen et al., 2016). Using geostrophic calculations based on summer hydrography, Marnela et al. (2013) found that the recirculation was strongest close to 79°N. Eddy-resolving regional

©2020. The Authors.

This is an open access article under the terms of the Creative Commons Attribution License, which permits use, distribution and reproduction in any medium, provided the original work is properly cited.

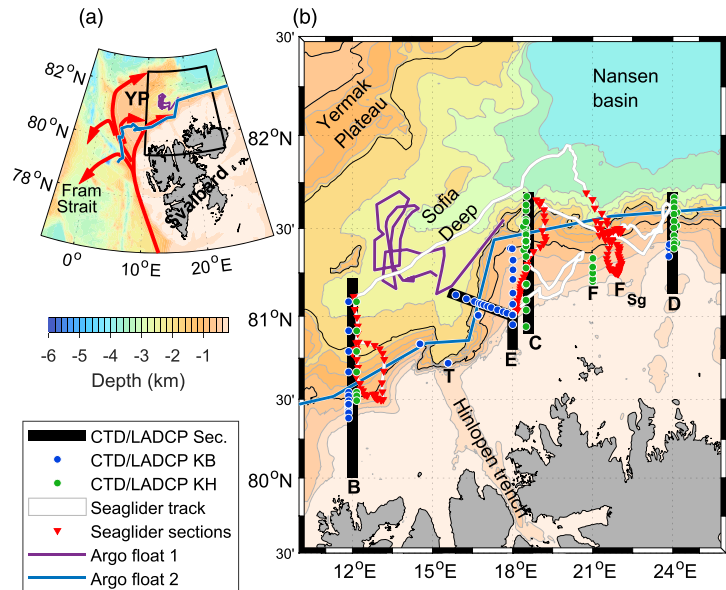


Figure 1. (a) Overview of the region of interest. Red arrows show the Atlantic Water circulation patterns. The black box is enlarged in (b). The Argo float paths are also shown. (b) Observation locations. CTD sections are marked with wide black lines extending from the southern to northern-most CTD profiles. Only CTD stations used for composite sections are marked with circles for clarity (coverage of other stations not shown on the sections can be seen in Figure 2): blue from the RV Kristine Bonnevie (KB) and green from the RV Kronprins Haakon (KH) cruises. Stations occupied in both cruises have been slightly offset for legibility. White line shows the entire Seaglider track, while red triangles show the Seaglider dives used for section plots. Black isobaths are at 800 and 1,500 m. Gray lines are isobaths from 200 to 1,400 m depth at every 200 m, and 2,000 to 6,000 at every 500 m. Letters indicate different sections referred to in the text, except T, which is a repeat occupation of three stations at the slopes of the topographic feature at the mouth of the Hinlopen trench.

ocean model results suggest that this recirculation contains relatively cold AW and is primarily related to the eastern rim of the Greenland Sea gyre, whereas the recirculation of the warmest AW occurs north of 80°N, mainly facilitated by eddies (Hattermann et al., 2016). Near the Yermak Plateau (YP), WSC initially splits into two branches: an outer branch following the slope of the plateau and an inner branch following the edge of the continental shelf, named the Svalbard branch (Aagaard et al., 1987). Further downstream the outer branch again divides into three branches: one branch recirculating in Fram Strait (Bourke et al., 1988; Hattermann et al., 2016; Wekerle et al., 2017), one continuing along the plateau, named the Yermak branch (Aagaard et al., 1987; Cokelet et al., 2008; Perkin & Lewis, 1984), and one flowing over the plateau along a topographic depression, named the Yermak pass branch (Gascard et al., 2013; Koenig et al., 2017; Menze et al., 2019). The Svalbard branch is relatively well-documented and accessible, whereas the outer Yermak and Yermak-pass branches are poorly documented due to meandering currents, challenging sea-ice conditions, and strong seasonal variability (Koenig et al., 2017).

A mooring array maintained across Fram Strait at 79°N shows that the long-term mean transport of waters with potential temperature >2°C in the WSC is about 3 Sv ($1 \text{ Sv} = 1 \times 10^6 \text{ m}^3 \text{ s}^{-1}$) (Beszczynska-Möller et al., 2012). However, the fraction of AW that enters the Arctic Ocean or recirculates westward to join the East Greenland current is not accurately known. As much as 50% of the AW entering Fram Strait is estimated to recirculate (Manley, 1995; Marnela et al., 2013). The Svalbard branch has historically been considered the main AW inflow route to the Arctic Ocean (Aagaard et al., 1987; Cokelet et al., 2008; Perkin & Lewis, 1984), but recent numerical simulations suggest that the Yermak Pass branch can be comparable

(Crews et al., 2019; Koenig et al., 2017). However, in situ observations are needed to quantify the relative contribution and variability of each branch. East of the YP, north of Svalbard, AW volume transport estimates range between 0.5 and 3.4 Sv, depending on the location and time of the observations and the AW definition that is used (Cokelet et al., 2008; Kolås & Fer, 2018; Pérez-Hernández et al., 2017; Våge et al., 2016). The most comprehensive of the estimates in this region is from a year-long record from a 6-mooring array across the continental slope north of Svalbard at 30°E covering the boundary current between the 200 m isobath and 50 km offshore of the shelf break (Pérez-Hernández et al., 2019). Using a definition of AW with potential temperature $\geq 1^\circ\text{C}$, practical salinity ≥ 34.9 , and potential density anomaly $\geq 27.6 \text{ kg m}^{-3}$, the average (± 1 standard deviation) AW transport was $2.1 \pm 0.2 \text{ Sv}$ (Pérez-Hernández et al., 2019). The transport estimates east of the YP likely integrate the contributions from the Svalbard, Yermak pass, and Yermak branches.

The three branches entering the Arctic Ocean are thought to merge and continue as a topographically steered boundary current. The Yermak Pass branch and the Svalbard branch probably merge between 10 and 15°E (Menze et al., 2019). The location where the Yermak branch merges with the other two is not clear. Historical observations suggested that parts of the Yermak branch left the Yermak Plateau at the northeastern tip, crossing over the basin before rejoining the boundary current (Perkin & Lewis, 1984). However, numerical models indicate that the Yermak branch flows around the plateau, following the slope, and rejoin the other branches between 12 and 18°E north of Svalbard (Crews et al., 2018; Koenig et al., 2017). Observations from drifting ice stations during winter and spring 2015 support paths seen in models (Meyer, Sundfjord, Fer, et al., 2017).

As the AW flows toward the Arctic, its hydrographic properties change through atmospheric forcing and interaction with sea ice and surrounding colder and fresher water masses (Boyd & D'Asaro, 1994; Rudels et al., 2000; Onarheim et al., 2014). Over steep topography, strong vertical shear and mixing as well as lateral exchange processes increase the rate of cooling and freshening. At the latitudes of YP, the along-path cooling and freshening is estimated to be 0.2°C per 100 km and 0.01 g/kg per 100 km, respectively, corresponding to a surface heat flux between 400 and 500 W m^{-2} (Boyd & D'Asaro, 1994; Cokelet et al., 2008; Saloranta & Haugan, 2004; Kolås & Fer, 2018). Such heat fluxes are much larger than the turbulent heat fluxes commonly observed near the YP. Typical heat fluxes near the plateau are $\mathcal{O}(10) \text{ W m}^{-2}$, and episodic events may reach $\mathcal{O}(100) \text{ W m}^{-2}$ (Fer et al., 2010; Meyer, Fer, et al., 2017; Sirevaag & Fer, 2009). It is not clear which processes can sustain such along-path cooling rates; however, eddies are thought to play a major role in this heat loss (Crews et al., 2019; Kolås & Fer, 2018; Våge et al., 2016). Eastward of 20°E, observations suggest substantially less along-path cooling (Pérez-Hernández et al., 2017).

In this study, we use observations during summer and fall 2018 (Figure 1b) to obtain a detailed description of the AW boundary current structure and volume transport north of Svalbard, east of the Yermak Plateau, and to quantify the intraseasonal variability. Our analysis identifies previously unknown circulation patterns in the region which may have implications for the transport and variability of the AW.

2. Data

Observational data from two scientific cruises (Fer et al., 2019, 2020), carried out as a part of the Nansen Legacy project, are supplemented by one Seaglider mission (Kolås & Fer, 2020) and two Argo floats north of Svalbard. All data were collected between July and December 2018. Station locations and tracks are shown in Figure 1b, and platform specific details are given in the corresponding subsections below.

2.1. Hydrographic Measurements From Cruises

The cruises were conducted by the Research Vessel (RV) Kristine Bonnevie between 27 June and 10 July 2018 and by the RV Kronprins Haakon between 12 and 24 September 2018. CTD profiles during both cruises were collected using a Sea-Bird Scientific, SBE 911plus system, with a 200 kHz Benthos altimeter allowing measurements close to seabed; 120 and 160 CTD profiles were collected during the summer and fall cruises, respectively. Water samples drawn at each station were used to calibrate salinity and dissolved oxygen measurements. Pressure, temperature, and practical salinity data are accurate to $\pm 0.5 \text{ dbar}$, $\pm 2 \times 10^{-3}^\circ\text{C}$, and $\pm 3 \times 10^{-3}$, respectively. CTD data were processed using the standard SBE Data Processing software. Conservative Temperature, Θ , and Absolute Salinity, S_A , were calculated using the thermodynamic

equation of seawater (IOC et al., 2010), and the Gibbs SeaWater Oceanographic Toolbox (McDougall & Barker, 2011).

2.2. Current Profiles From Cruises

The CTD frames on both vessels were fitted with a pair of acoustic Doppler current profilers (ADCPs), so-called lowered-ADCPs (LADCPs). The LADCPs were 6,000 m-rated 300 kHz Teledyne RD Instruments (RDI) Sentinel Workhorses, one mounted pointing downward and one upward. The LADCPs were synchronized and set to provide data vertically averaged in 8 m bins. On the Kristine Bonnevie the LADCPs had internal batteries, while on the Kronprins Haakon they had an external battery mounted on the frame. Compasses were calibrated on land prior to cruises with resulting errors less than 1–2°. LADCP data were processed using the LDEO software version IX-13 based on Visbeck (2002). The LADCP profiles were constrained by navigation data and 5-min averaged profiles from the ship's ADCPs (SADCP).

RV Kronprins Haakon had four SADCPs: two 38 kHz and two 150 kHz Teledyne RDI Ocean Surveyors. One of each was mounted on a drop keel, and one of each was flush-mounted in the hull. Flush-mounted ADCPs were protected by an acoustically transparent window allowing for profiling when moving through ice. Only the 38 kHz ADCP mounted on the drop keel was used for constraining the LADCP processing. Kristine Bonnevie had a 150 kHz Teledyne RDI Ocean Surveyor SADCP. The ADCPs collected profiles in 8 m vertical bins below a blank distance of 16 m. The data were collected using the VmDAS software onboard Kronprins Haakon and the UHDAS software onboard Kristine Bonnevie. Horizontal velocity profiles were obtained as 5 min averages using the University of Hawaii postprocessing software, to an uncertainty of 2–3 cm s⁻¹ (Firing & Ranada, 1995).

2.3. Seaglider Data

A Kongsberg Seaglider was deployed from the RV Kronprins Haakon on 17 September 2018. The Seaglider track (Figure 1b) was planned to maximize the number of cross-sections along the boundary current, while avoiding sea ice. A total of 377 dives (754 profiles) were performed before recovery on 11 November 2018. The typical horizontal distance between two surfacing locations was 3 km. The Seaglider operated between the surface and 1,000 m depth, sampling CTD on both dives and climbs at a sampling rate of 10 s in the upper 200 m, 20 s between 200 and 600 m, and 30 s below 600 m. The vertical velocity was normally close to 10 cm s⁻¹. For each dive, a depth-averaged current (DAC) is estimated based on the deviation between expected surfacing location deduced from the flight model and the actual surfacing location. The Seaglider was equipped with a Paine strain-gauge pressure sensor, a SBE CT Sail and an Aanderaa dissolved oxygen sensor. The data set was processed using the University of East Anglia Seaglider toolbox (<http://www.byqueste.com/toolbox.html>), based on the methods described by Garau et al. (2011) and Frajka-Williams et al. (2011). Processed S_A and Θ are accurate to 0.01 g kg⁻¹ and 0.001°C, respectively, and DAC is accurate to 0.01 m s⁻¹ (p. 9 “Seaglider Quality Control Manual,” 2012). Data spikes above three standard deviations, for each pressure level over all profiles, were removed during postprocessing. Finally, a salinity offset correction of 0.005 g kg⁻¹ was applied after comparing the deep part of Seaglider dives (750 to 1,000 m) to nearby CTD profiles (within 7 days and 15 km) collected from the RV Kronprins Haakon.

2.4. Argo Floats

Current trajectories from two Argo floats, WMO Id 6903548 and 3901910, hereby referred to as float 1 and 2, were available north of Svalbard in the period from June to December 2018. Both floats drifted at a parking depth of 1,000 dbar, profiling between a maximum depth of 2,000 dbar and the surface. Float 1 profiled every 3 days from June to 9 November, and every 10 days thereafter, and float 2 every 7 days during the study period. We calculated the current trajectories at 1,000 m depth at the midposition between two surfacing locations by dividing displacement by time. The Argo float data were collected and made freely available by the International Argo Program and the national programs that contribute to it (<http://www.argo.ucsd.edu>, <http://argo.jcommops.org>) (International Argo Program, 2003). The Argo Program is part of the Global Ocean Observing System.

2.5. NORAI0

Wind speed and direction at 10 m above sea level were extracted at hourly intervals in the area north of Svalbard (0–35°E, 79°N–83°N), from the Norwegian Reanalysis Archive (NORAI0; Reistad et al., 2011).

NORA10 is a regional high resolution (10–11 km) atmospheric downscaling of ERA-40 (Uppala et al., 2005) and ECMWF IFS (European Center for Medium-Range Weather Forecasts Integrated Forecasting System) operational analyses (after 2002), covering the northern North Atlantic and the Barents Sea. The dynamic atmospheric downscaling is performed as a series of short prognostic runs (using High Resolution Limited Area Model) initialized from a blend of ERA-40 and the previous prognostic run to preserve the fine-scale surface features from the high-resolution model, while maintaining the large-scale synoptic field from ERA-40. We calculated the wind stress components, using the Large and Pond (1981) parameterization, and the wind stress curl over the region of interest (box in Figure 8c). We present time series spatially averaged over the region and time-averaged fields during cruise periods and Seaglider transects.

2.6. Historical Data

Historical data for the region around Svalbard were obtained from the UNIS hydrographic database described by Skogseth et al. (2019). We used a subset of these data covering the continental slope north of Svalbard between 12°E and 24°E, for the months July to November. The profiles were initially scanned visually to remove large spikes, before removing data above three standard deviations at each pressure level over all profiles. A total of 1,118 profiles were used for the composite section (section 4.7), 65% of these were collected pre-2008 and 35% in the last decade.

2.7. Other Data Sets

Barotropic tidal currents were obtained from the Arctic Ocean Inverse Tide Model on a 5 km horizontal grid (Arc5km2018) (Erofeeva & Egbert, 2020). We used the eight main constituents (M_2 , S_2 , N_2 , K_2 , K_1 , O_1 , P_1 , and Q_1) and four nonlinear components (M_4 , MS_4 , MN_2 , and $2N_2$), to predict the horizontal tidal volume transport ($m^2 s^{-1}$) at profile location and midtime for cruise stations and at time and location of the Seaglider calculated from a flight model.

Bathymetry data are from the third version of the International Bathymetric Chart of the Arctic Ocean (IBCAO) (Jakobsson et al., 2012). We used the 30 arc-seconds grid in our analysis.

Daily mean sea ice properties based on satellite observations at 10 km grid resolution are obtained from the EUMETSAT Ocean and Sea Ice Satellite Application Facility (OSI SAF, www.osi-saf.org).

3. Methods

3.1. Detiding Current Measurements

Current profile measurements from LADCPs and SADCs and the DAC from the Seaglider were detided using the Arc5km2018 inverse tidal model. Barotropic tidal currents were obtained by dividing the predicted barotropic tidal transport at the time and location of the measurement, by the total water depth at measurement location. Water depth at measurement location was interpolated from a smoothed version of IBCAO (described in section 3.3). The barotropic tidal components were subtracted from the measured currents.

Detiding of the DAC measured by the Seaglider needs care because one dive-climb cycle takes about 6 hr (time between pairs of pre-dive and post-climb GPS fixes). We estimated the average tidal current during the dive-climb cycle. Based on the Seaglider flight model, latitude, longitude, and time stamps were estimated for every decibar during the dive-climb cycle. These values were used as input to predict the barotropic tidal transport at given time and location at each depth level. Bottom depth along the Seaglider track was interpolated from the smoothed IBCAO field, in order to obtain tidal velocity. Finally, we calculated the average tidal current during profiling and subtracted it from the Seaglider's depth average current.

3.2. Synoptic Sections

Each section (section B, C, D, E, and F, see Figure 1) is defined along a line normal to the 800 m isobath close to the original station locations. Note that the stations identified with markers in Figure 1 are for those used to construct composites (section 3.3), and the complete station coverage along each section can be seen (arrowheads) in Figure 2. Using station depth obtained from the smoothed IBCAO field, we moved each station along isobaths onto the corresponding section. The current vectors u and v (east and north) were rotated to obtain along isobath velocity u_r (>0 eastward) and across isobath velocity v_r (>0 toward deep water), relative to the local 800 m isobath's orientation at the corresponding section. Distance to the 800 m isobath is positive toward the shelf and negative toward deep waters. Seaglider data were horizontally averaged in

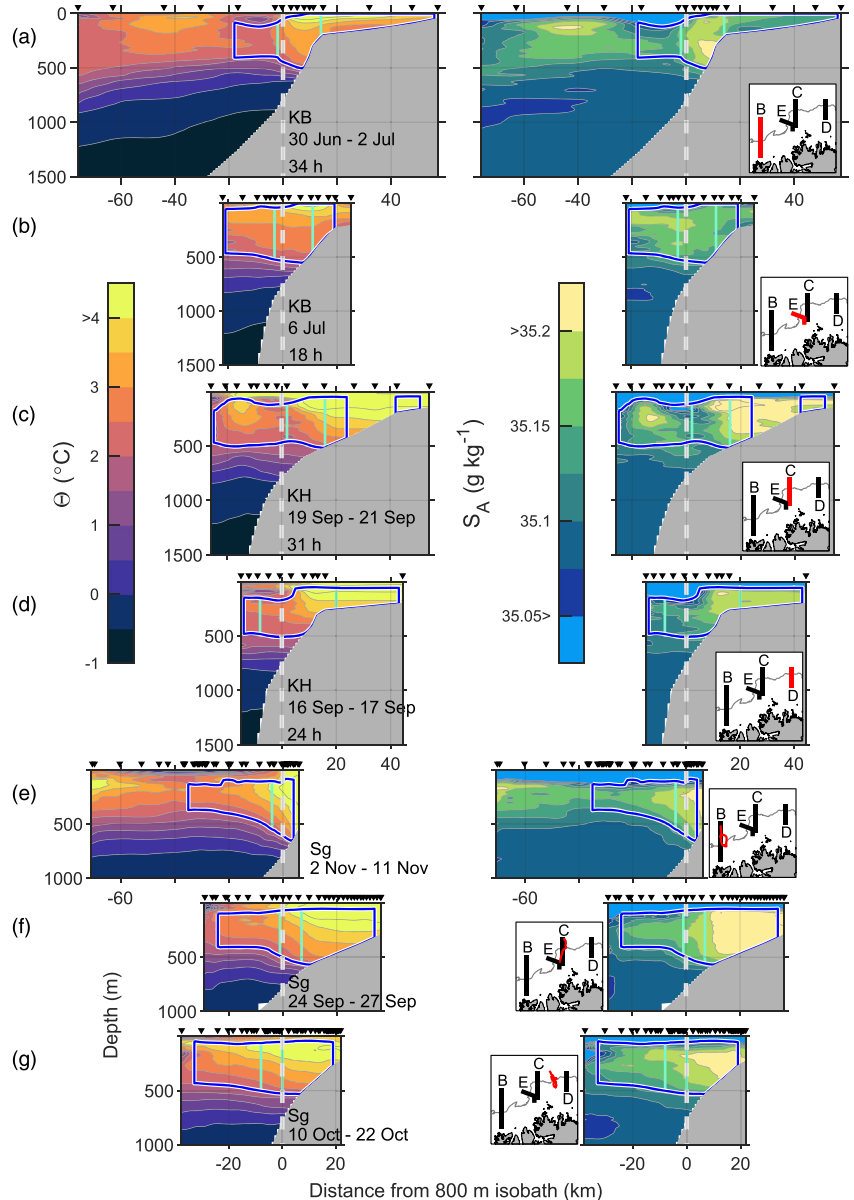


Figure 2. Conservative Temperature, Θ , and Absolute Salinity, S_A , for synoptic sections. The section displayed in each row is indicated by a red line in the respective overview inset on the right. The white dashed line at 0 km and the isobath marked in the overview inset show the location of the 800 m isobath. Blue line envelopes AW with $U_g > 0$. Green vertical lines envelope the stream tube used in the along-path heat loss calculations. Black triangles at the top of each panel show cruise profile location and Seaglider surface location. KB = RV Kristine Bonnevie, KH = RV Kronprins Haakon, Sg = Seaglider.

2 km bins before interpolation. All sections, including the Seaglider sections (B_{sg} , C_{sg} , and F_{sg}), were interpolated onto a $2\text{ m} \times 1\text{ km}$ grid (vertical \times horizontal). We used a Laplacian spline interpolation method with tension, choosing a 15 km search radius and no smoothing (Smith & Wessel, 1990; Pickart & Smethie, 1998). Finally all sections are smoothed using a $20\text{ m} \times 20\text{ km}$ moving average window to remove small scale variability.

3.3. Composite Sections

Composite sections for each cruise and the Seaglider were constructed by organizing the data on the average bathymetry profile described in Appendix A. A station is positioned at the distance on the average bathymetry profile corresponding to the water depth at measurement location. After locating each station at the cross section, the data were binned, interpolated, and smoothed similar to the synoptic sections described in section 3.2. CTD stations used for the summer and fall composite sections are shown in Figure 1. All Seaglider dives were included in the late fall composite.

Prior to generating the composite section, velocity vectors are projected onto local along- (u_r) and across-isobath (v_r) components using the smoothed IBCAO bathymetry to remove small scale local variations in topographic gradients. Smoothing is made using a 3 km Gaussian window as a 2-D convolution operator. The bathymetry gradients at each CTD station and average Seaglider dive locations were then used to project velocity vectors onto along- and across-isobath vectors. The along-isobath component of the de-tided observed velocity in these composite sections is used to constrain the geostrophic velocities (section 3.4).

3.4. Absolute Geostrophic Velocity and Atlantic Water Volume Transport

Relative geostrophic velocity was obtained from Gibbs SeaWater Oceanographic Toolbox using dynamic height anomaly referenced to the surface pressure (McDougall & Barker, 2011). Absolute geostrophic velocities were obtained by vertically integrating the geostrophic shear and constraining its depth average by the along-isobath component of the observed depth-averaged current. For sections B, C, E, D, and the composite sections, the observed depth-averaged current was obtained from LADCPs, whereas for the synoptic and composite Seaglider sections DAC was used.

We calculated the transport density U_g ($\text{m}^2\text{ s}^{-1}$) in the AW layer by vertical trapezoidal integral of the geostrophic current u_g . Following Swift and Aagaard (1981), Aagaard et al. (1985) and Cokolet et al. (2008), we defined AW as water with $\Theta > 2^\circ\text{C}$ and $S_A > 35.05\text{ g kg}^{-1}$. Lateral boundaries of the AW inflow were defined as the location where the layer integrated velocity was zero ($U_g = 0$). Total volume transport was then computed as the horizontal integral of $U_g > 0$.

3.5. Along-Path Rate of Change of Heat Content

We estimate the along-path heat loss of the AW inflow by comparing the integrated heat content of AW from one cross-slope section to the next further downstream. As shown in IOC et al. (2010) and McDougall (2003) the first law of thermodynamics is practically equivalent to the conservation equation for Conservative Temperature (Θ), which is proportional to potential enthalpy, h_0 , as $\Theta = h_0/C_p$. The heat content per unit mass of seawater is then $C_p\Theta$, where $C_p = 3991.867\text{ J kg}^{-1}\text{ K}^{-1}$ is the specific heat (IOC et al., 2010). Finally, heat content is integrated laterally and vertically in the cross-slope region, to obtain total heat content per downstream meter.

While the AW volume transport for each section can be calculated as described in section 3.4, the calculation of the heat loss between sections using the rate of change in heat content requires that the volume transport is conserved. For each synoptic section, we therefore defined a stream tube conserving a specified volume transport of AW, representative of the core of the current. We constrained each stream tube at 1.1 Sv , which is the AW volume transport through section D after excluding the outer parts with station gaps. Starting at the location of maximum layer-integrated velocity (i.e., maximum U_g), we integrated U_g symmetrically across the section until we reached the target volume transport. For each stream tube we calculated velocity-weighted average Θ and S_A , and average u_r .

The along-path rate of change of heat content calculation is based on the methods described by Boyd and D'Asaro (1994) and Cokolet et al. (2008), assuming only the eddy fluxes at the surface are important and neglecting thermal inertia and local advection of heat. Then all observed heat loss, Q , must be due to heat

fluxes through the surface of our stream tubes. Applying Gauss theorem on the volume integral of the heat advection yields

$$\int_{Surface} Q dx dy = \rho_0 C_p \bar{u} \int_A \frac{\partial \Theta}{\partial y} dx dz, \quad (1)$$

where the area integral is taken over the stream tube's cross section A , \bar{u} is the mean u_r (along-isobath velocity), and ρ_0 is the reference seawater density. Here, y is the along-path coordinate and estimated as the distance between the sections along the 800-m isobath north of Svalbard. The along-path temperature gradient was obtained from the slope of a line fit to along-path distance against the velocity-weighted average Θ for each section. The advected area-integrated heat content change per along-path meter ($W m^{-1}$) from Equation 1 was divided by the average width of the stream tube to obtain the surface heat flux ($W m^{-2}$). These calculations are similar to and can be compared with those reported in Kolås and Fer (2018) for the AW current west of Spitsbergen.

4. Results

The summer, fall, and late fall conditions are presented, first in form of individual sections and then the corresponding composite sections. Figure 2 shows Conservative Temperature (Θ) and Absolute Salinity (S_A) for sections B, C, D, and E, and Seaglider sections B_{Sg} , C_{Sg} , and F_{Sg} . Figure 3 shows the same synoptic sections as Figure 2 but for absolute geostrophic velocity. Figure 4 shows the composite sections for the summer cruise, fall cruise, and the Seaglider mission (late fall).

4.1. Summer

Sections B and E were collected during June and July from the RV Kristine Bonnevie and are referred to as the summer sections (Figures 2a, 2b, 3a, and 3b). Section B shows two cores in Θ and S_A . The outer core is located at -40 km, roughly above the 1,700 m isobath, while the inner core is located at 10 km. The inner core is the AW boundary current flowing eastward into the Arctic and transports 1.8 Sv of AW. Details are given in Table 1. Four days later at section E the transport is 1.7 Sv. Section E does not capture the outer extent of the AW, however, covers its dynamic core. While the average AW salinity remains roughly the same from B to E, the temperature decreases slightly by $0.2^\circ C$. The upper layer of AW is known to enter the Hinlopen trench at $17^\circ E$ (Figure 1) and is likely cooled as a result of this circulation (Menze et al., 2019). The maximum AW temperature is found near the surface in both sections. In section B, there is a clear salinity maximum near the seabed at the shelf break (right panel of Figure 2a), which is absent in section E. A likely explanation for this is convectively driven mixing induced by downslope Ekman transport advecting lighter water under denser water, known to be important in the region (Kolås & Fer, 2018).

The along-path rate of change of heat content advected in the AW layer from sections B to E is $-9.1 \times 10^7 W m^{-1}$, corresponding to a heat loss of $550 W m^{-2}$. Note that at this section the temperatures are increasing toward the surface; thus any heat loss must be caused by lateral mixing or advection or by vertical mixing with colder waters below the Atlantic layer. However, there may be upward heat loss to the overlying waters on the shelf as the AW circulates in the Hinlopen trench. AW heat loss in the Hinlopen trench has not been accounted for when calculating heat loss along the 800 m isobath. The along-path temperature and salinity gradients are $-0.21^\circ C/100$ km and $-0.015 g kg^{-1}/100$ km, respectively, from sections B to E.

The summer composite hydrography shows a two-branch structure in temperature and salinity (Figures 4a and 4b), where the outer branch flows westward and the inner branch eastward (Figure 4c). The inner branch is barotropic and symmetrically centered around 8 km. In summer, the average AW transport into the Arctic is 2.0 Sv. The outer branch, located at -30 km, is baroclinic, with eastward bottom currents. Possible origin of this bottom-intensified current will be discussed in section 5.3. Geostrophic velocity integrated vertically over the AW layer shows a weak westward AW transport in the outer branch (Figure 4d). This westward transport is consistent in all our composite sections and motivated us to calculate the general statistics of this flow (see Table 2). The average temperature of the reverse current is 0.4 to $0.9^\circ C$ lower than the main branch.

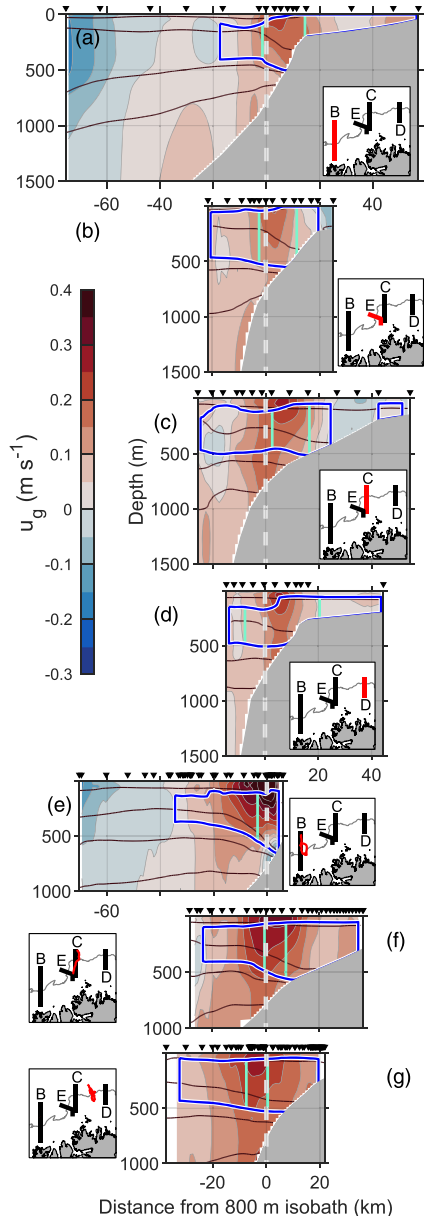


Figure 3. Same as Figure 2, but for along-isobath absolute geostrophic velocity, u_g . Black lines are σ_0 contours. Positive velocities are approximately eastward along the continental slope.

4.2. Fall

Figures 2c and 2d show sections C and D during the September cruise. Section C shows two separate cores in Θ and S_A , an outer core located at ~ 15 km, and an inner core near the 500 m isobath at 20 km. u_g does not show the same two-core structure (Figure 3c) but a surface-intensified core with a vertically integrated u_g maximum at 9 km. However, the isopycnals spread roughly where the outer core is located and u_g becomes negative. This suggests that the outer core may be water trapped in an anticyclonic eddy, detached from the inner core, with a center at the edge of section C. The AW volume transport at section C is 1.9 Sv (Table 1). Note that an opposing flow between 22 and 41 km on the shelf, where u_g is negative, divides the AW layer.

Section D at 24°E, conducted 4 days prior to section C, shows a less saline AW layer, indicating mixing with surrounding fresher water masses. Θ and S_A maxima are located at the shelf break, while the u_g core is located above the 550 m isobath (Figure 3d). Section D shows a sharp front between AW and polar surface water with polar surface water intruding above the outer part of the AW layer. Note the large gap without stations between the 20 and 40 km on the shelf. The AW volume transport at section D is 1.4 Sv.

The along-path rate of change of heat content advected from section C to D is $-9.6 \times 10^6 \text{ W m}^{-1}$, equivalent to a surface heat loss of 420 W m^{-2} . The along-path temperature and salinity gradients are $-0.21^\circ\text{C}/100 \text{ km}$ and $-0.017 \text{ g kg}^{-1}/100 \text{ km}$, respectively.

The middle column of Figure 4 shows the composite section from the September cruise. The AW layer flowing into the Arctic is wide with two salinity cores (Figure 4b). The outer core is co-located with a local u_g maximum (Figure 4c), also observed as a peak in U_g (Figure 4d). The transport estimated from this composite is 2.9 Sv, larger than that in the synoptic sections C and D (1.9 and 1.4 Sv, respectively). One reason for this is that the composite section contains more CTD stations (along 12°E and 21°E, see Figure 1b) than only those from the two synoptic sections. In addition, the counter current observed on the shelf in section C is missing in the composite, thus increasing the cross-stream area of the eastward flow. However, although the composite sections are useful, allowing direct comparison between cruises, we do alter the cross-stream Θ and S_A gradients by moving stations onto corresponding isobaths on the composite section. This can potentially lead to unrealistic u_g estimates, which we discuss in section 5.4.

4.3. Late Fall

Figures 2e–2g show the Seaglider sections conducted between late September and early November. Section B_{Sg} (Figure 2e) is at the same location as section B. Of the two cores of warm and saline AW seen in the Θ and S_A distribution, only the inner branch is the eastward flowing boundary current (Figure 3e). The outer branch, starting at ~ 40 km, flows westward and is surface intensified. The AW transport at section B_{Sg} is 2.3 Sv; however, this transport is likely an underestimate because the shallow side of the AW layer on the shelf is not captured by the Seaglider.

Section C_{Sg} (Figures 2f and 3f) is at the same location as section C. Whereas both the Θ and S_A maxima are located up-slope of the 800 m

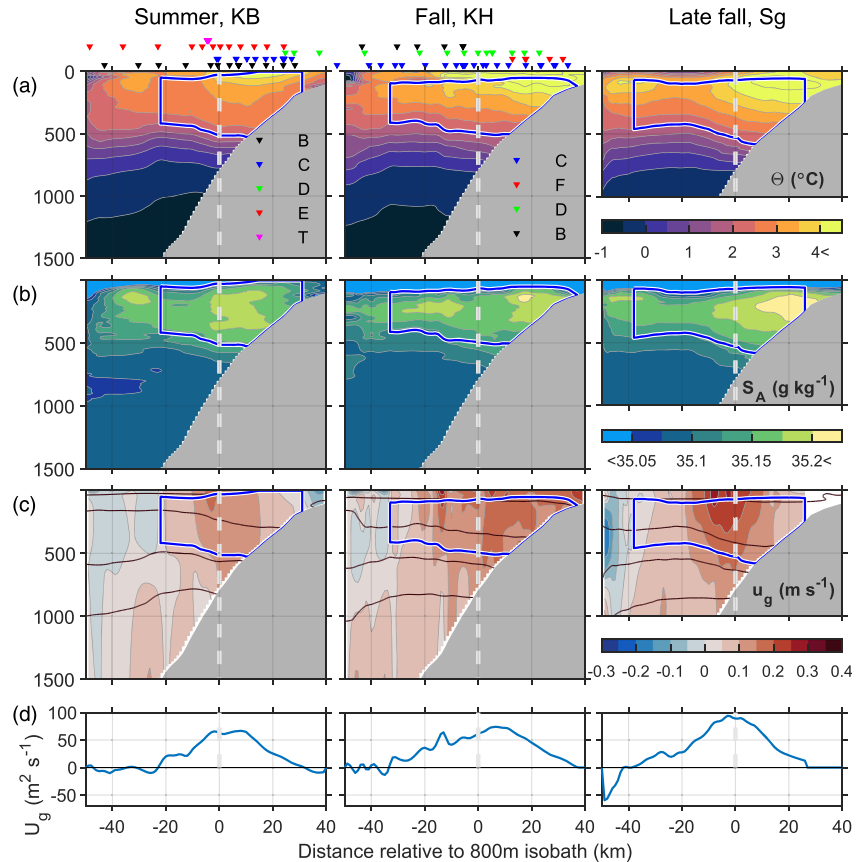


Figure 4. Composite sections for the summer cruise (KB), the fall cruise (KH), and the Seaglider mission during late fall (Sg). White dashed line at 0 km indicates the location of the 800 m isobath. Arrowheads, colored for the sections as indicated, show the location of the profiles. (a) Conservative Temperature, Θ , (b) Absolute Salinity, (c) along-isobath absolute geostrophic velocity, u_g , and (d) transport density, U_g , calculated by vertically integrating u_g within the Atlantic Water layer defined by temperature and salinity properties. Blue line envelopes the Atlantic Water with $U_g > 0$ used in transport calculations.

isobath, the u_g core is located at the 800 m isobath. The AW volume transport is 3.5 Sv. Note that section C_{Sg} was conducted only a few days after section C, where the AW volume transport was 1.9 Sv. The large increase from section C to C_{Sg} will be discussed in section 5.2.

Finally, section F_{Sg} (Figures 2g and 3g) is located between C and D. Section F_{Sg} is very similar to section C_{Sg} . Θ and S_A cores are located up-slope from the u_g core, and the AW transport is 3.4 Sv.

While conserving the volume transport in stream tubes (as described in section 3.5) we calculated the along-path rate of change of heat content advected from section B_{Sg} to F_{Sg} to be $-1.5 \times 10^7 \text{ W m}^{-1}$, where the temperature gradient was $-0.34 \text{ }^\circ\text{C}/100 \text{ km}$. For comparison, Saloranta and Haugan (2004) found a downstream winter temperature gradient of $-0.34 \text{ }^\circ\text{C}/100 \text{ km}$ west of Svalbard. Due to the large time difference between the Seaglider sections we had to account for the seasonal temperature change. Using a linear fit to the mean AW stream tube temperatures and time of occupations of sections B, C, C_{Sg} , and B_{Sg} we found a

Table 1
Properties of the Atlantic Water Boundary Current

Section	$\bar{\Theta}$ (°C)	\bar{S}_A (g kg ⁻¹)	\bar{u}_g (m s ⁻¹)	Area (km ²)	Transport (Sv)
B	3.2 ± 0.1	35.16 ± 0.01	0.10	17	1.8 ± 0.1
E	3.0 ± 0.1	35.16 ± 0.01	0.09	18	1.7 ± 0.1
C	3.1 ± 0.1	35.15 ± 0.01	0.08	26	1.9 ± 0.1
D	3.2 ± 0.1	35.14 ± 0.01	0.08	15	1.4 ± 0.2
B _{Sg}	3.5 ± 0.1	35.16 ± 0.01	0.15	13	2.3 ± 0.1
C _{Sg}	3.4 ± 0.1	35.17 ± 0.01	0.15	22	3.5 ± 0.1
F _{Sg}	3.4 ± 0.1	35.16 ± 0.02	0.16	21	3.4 ± 0.2
Summer	2.9 ± 0.1	35.16 ± 0.01	0.09	21	2.0 ± 0.1
Fall	3.3 ± 0.1	35.16 ± 0.02	0.13	23	2.9 ± 0.4
Late fall	3.3 ± 0.1	35.16 ± 0.01	0.11	25	3.0 ± 0.2
Average	3.2 ± 0.1	35.16 ± 0.01	0.10	25	2.6 ± 0.2

Note. Calculations are presented for the synoptic sections, the seasonal composite sections, and the full period average composite section. For calculation methods the reader is referred to section 3. Overbar denotes velocity-weighted arithmetic means. Error calculations are described in Appendix B and are rounded to one significant digit for $\bar{\Theta}$ and volume transport and two significant digits for S_A .

site of the along-isobath component of the summer and fall cruises and finally average the depth-averaged currents together with the Seaglider DAC. We use the 0–1,000 m depth-averaged current to be consistent with the Seaglider which averages the currents in the upper 1,000 m. However, the results are not sensitive to this: When compared to the full depth averages, LADCP 0–1,000 m average current differed by less than 0.5 cm s⁻¹.

Two branches identified by temperature and salinity maxima separate at the 1,500 m isobath (–20 km), where the isopycnals shoal locally. The inner branch is the AW boundary current with an average volume transport of 2.6 Sv. The outer branch is a westward current that transports about 0.1 Sv of AW (see Table 2 for details). We note that the westward flowing branch is not fully captured by our observations, and our calculations are potentially an underestimate. The two branches, each about 500 m thick, are separated by a thinner AW layer. Figures 5b–5d show the summer, fall, and late fall anomalies, respectively. Anomalies, calculated by subtracting the seasonal average from the individual composites, highlight the changes that occurred from summer through late fall. During summer, the AW is characterized by negative salinity and temperature anomalies, overlain by a relatively salty surface layer. Throughout the summer and fall, the surface layer freshens because of summer sea ice melt, and the AW becomes warmer and saltier. From fall to late fall the surface layer above the AW cools and the salinity increases again, while the Atlantic layer continues to heat and increase in salinity, especially at depth. The outer branch shows an even stronger seasonal change than the inner branch, suggesting more AW is directed into the outer branch during late fall.

Between summer and late fall, we observe a 1 ± 0.3 Sv increase in the AW inflow, with maximum transports observed during October. In the same period, the velocity-weighted average AW temperature increased by 0.4 ± 0.2°C. The seasonal increase in transport and heat content of the Atlantic Water boundary current can be linked to the seasonal variability of the Atlantic Water inflow west of Svalbard, which is known to be at a maximum at the end of fall/beginning of winter (Beszczynska-Möller et al., 2012).

seasonal change of 0.20°C/month. A linear fit approximates the segment of the annual cycle between July and November well. Note that before applying the linear fit, the average stream tube temperatures in sections C and C_{Sg} were moved to section B location by using the downstream temperature gradient observed during summer and fall. This was done in order to minimize the spatial contribution in the seasonal change estimate.

Similar to the summer section, the composite section obtained from all data collected by the Seaglider shows a two-branched structure in $\bar{\Theta}$ and S_A , where the outer branch flows westward (the right column of Figure 4). The inner branch (marked with blue box) is the boundary current flowing into the Arctic. u_g and U_g are centered at the 800 m isobath. The AW transport estimate is 3.0 Sv.

4.4. Average Section

An average section is obtained by averaging the summer, fall, and late fall composites for $\bar{\Theta}$ and S_A (Figure 5). Relative geostrophic velocity is then calculated from the average $\bar{\Theta}$ and S_A fields (Figure 5a), and absolute geostrophic velocity is obtained by using the average 0–1,000 m depth-averaged observed velocity from all three data sets as reference velocity. That is, we calculate the 0–1,000 m depth-averaged LADCP velocity from the composite of the along-isobath component of the summer and fall cruises and finally average the depth-averaged currents together with the Seaglider DAC. We use the 0–1,000 m depth-averaged current to be consistent with the Seaglider which averages the currents in the upper 1,000 m. However, the results are not sensitive to this: When compared to the full depth averages, LADCP 0–1,000 m average current differed by less than 0.5 cm s⁻¹.

Table 2
Properties of the Atlantic Water Reverse Current ($U_g < 0$)

Section	$\bar{\Theta}$ (°C)	\bar{S}_A (g kg ⁻¹)	\bar{u}_g (m s ⁻¹)	Area (km ²)	Transport (Sv)
Summer	2.5	35.14	0.01	10	–0.1
Fall	2.6	35.14	0.02	5	–0.1
Late fall	2.7	35.14	0.08	4	–0.2
Average	2.3	35.13	0.02	3	–0.1

Note. Calculations are presented for the seasonal composite sections and the full period average composite section. Overbar denotes velocity-weighted arithmetic means. The negative transports are westward.

From the u_g anomalies we see that the current intensifies from summer to fall, as its core shifts seaward. Below the AW layer, there is an outer bottom-intensified current, which we discuss in section 5.3. The bottom-intensified current is capped by a local salinity minimum shown with the red contour in the S_A plot. This salinity minimum is common in the Eurasian Basin and is identified as the Arctic Intermediate Water formed in the Nordic Seas (Rudels et al., 2005).

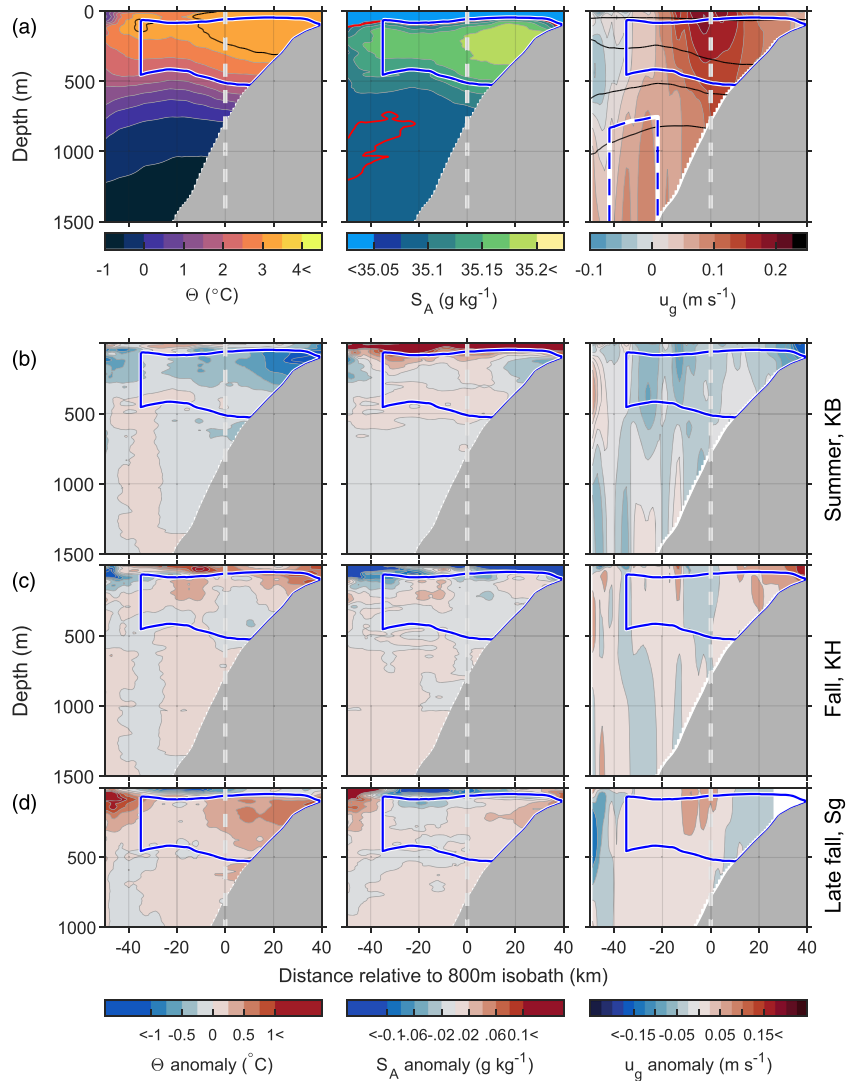


Figure 5. (a) Average composite sections for Θ , S_A , and u_g , based on the summer, fall, and late fall composites in Figure 4. Anomalies for Θ , S_A and u_g from the average composite section are shown for (b) summer, (c) fall, and (d) late fall. White dashed line indicates the location of the 800 m isobath. Blue line envelops the Atlantic Water with $U_g > 0$. Blue dashed line envelops the bottom-intensified current. Black line in the Θ plot is the 3.3°C isotherm. Red line in the S_A plot is the 35.08 g kg^{-1} isohaline. Black lines in the u_g plot are isopycnals.

In our study period, we identify two main domains on $\Theta - S_A$ space, where water flows into the Arctic Ocean (Figure 6). We compute the volume transport from the composite section using bins of $d\Theta = 0.25^\circ\text{C}$ and $dS_A = 0.01 \text{ g kg}^{-1}$. The transport is concentrated in the boundary current transporting AW (2.6 Sv), and the bottom-intensified current transporting Arctic Intermediate Water, Eurasian Basin Deep Water, and

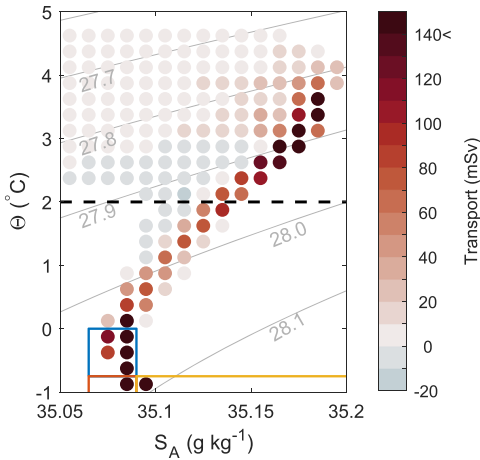


Figure 6. $\Theta - S_A$ diagram from the seasonal average composite section (Figure 5), showing volume transport estimated for $\Theta - S_A$ grid cells ($dS_A = 0.01 \text{ g kg}^{-1}$, $d\Theta = 0.25^\circ\text{C}$). Blue box encloses Arctic Intermediate Water, red encloses cold Norwegian Sea Deep Water, and yellow encloses Eurasian Basin Deep Water (Schlichtholz & Houssais, 2002). Black dashed line indicates the lower Θ boundary of the Atlantic Water.

cold Norwegian Sea Deep Water (water mass definitions from Schlichtholz and Houssais (2002)). In order to quantify the contribution from the bottom-intensified current, we excluded water masses with $\Theta > 0$ and $S_A > 35.1$ and integrated u_g vertically to obtain layer-integrated velocity. The lateral boundaries were set where the layer-integrated velocity first reduced to less than 50% of its maximum. This yielded the blue dashed line enveloping the bottom-intensified current in the u_g plot in Figure 5a. Transport by the bottom-intensified current is 1.5 Sv and represent 35% of the observed flow entering the Arctic Ocean. The average temperature and salinity are -0.6°C and 35.08 g kg^{-1} , respectively, with an average geostrophic velocity of 0.07 m s^{-1} .

4.5. Vertically-Averaged Currents

Circulation patterns inferred by combining all our measurements can help interpret the hydrographic observations. Figure 7a shows observed average currents between June and November, while Figure 7b shows the objectively mapped field of the average currents. The average circulation during our study period is obtained using observations from LADCPs, SADCs, and the DAC from the Seaglider. Observations were averaged over the upper 1,000 m (or full depth if shallower), before bin averaging in 3 km by 3 km horizontal bins. Average currents were objectively interpolated using a covariance function depending on the spatial distance between binned observations and the fractional distance to large-scale barotropic potential vorticity (f/H) contours (Böhme & Send, 2005). We used a 25 km correlation length scale, based on the semivariogram analysis

described in Appendix B and 20% error. Currents from Argo floats were calculated from the displacement between two surfacing locations; however, they were not included in the objective interpolation as their drift at 1,000 m depth may not be representative of the upper 1,000 m average currents.

The AW boundary current follows the continental slope roughly along the 800 m isobath, except for between sections E and C (Figure 7). West of section C (at 18°E and 81.25°N) the objective interpolation shows a divergent field along the path of the boundary current. The divergence suggests a deviation from the average geostrophic flow and indicates a location with highly variable currents. We hypothesize that the shelf break near 18°E can be important for ejecting and distributing AW into the Sofia Deep. Along the southern rim of the Sofia Deep, the currents flow westward, consistent with the reverse flow observed at the seaward edge of our sections (Figure 4).

4.6. Wind forcing

The wind forcing was highly variable in the region north of Svalbard. Figure 8 shows the wind stress vector (τ) and wind stress curl ($\nabla \times \tau$), both as a time series from June to November (Figures 8a and 8b), and average conditions during the cruise periods and the different Seaglider sections (Figures 8c–8g). From Figures 8d (Fall cruise) to 8e (Seaglider section C_{Sg}) we see a large change in τ and $\nabla \times \tau$. During the cruise transect along section C (end of the Fall cruise), $\nabla \times \tau$ was negative over the Sofia Deep and the continental slope, and rapidly changed sign to positive at the time of the Seaglider transect. The dashed vertical line in Figure 8a separates the Fall cruise from the Seaglider transect. This rapid change in wind stress curl occurs at the same time as the volume transport through section C increases from 1.9 to 3.5 Sv, and is likely a geostrophic response to the change in sea surface height (η) forced by the wind, discussed in section 5.2.

The root-mean-squared (RMS) wind stress curl from the time series in Figure 8a was $0.43 \times 10^{-6} \text{ N m}^{-3}$. Between 1 June and 30 November, we observed seven events with positive wind stress curl and six events with negative wind stress curl with magnitudes above one RMS value. The events lasted between 1 and 5 days, with the longest event being the positive anomaly during the Seaglider transect C_{Sg} .

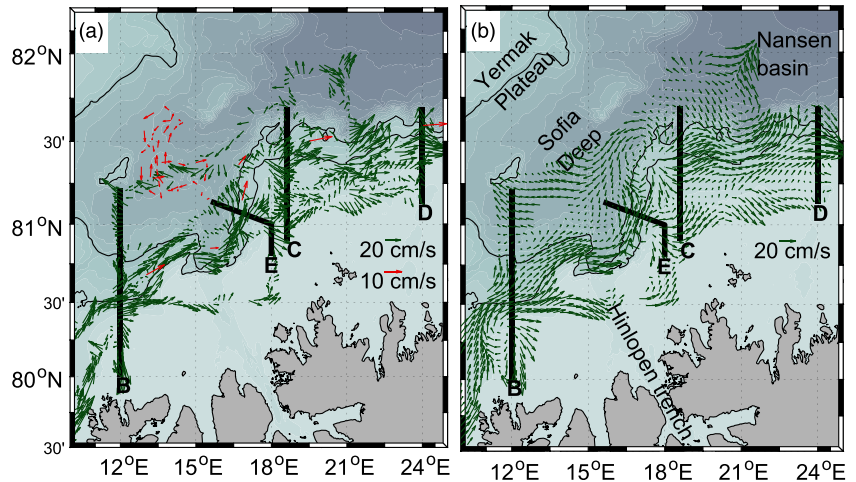


Figure 7. (a) Green arrows show 0–1,000 m depth-averaged currents, bin-averaged over 3 km by 3 km horizontal bins, from SADCPs, LADCPs, and Seaglider. Red arrows show drift trajectories from Argo floats. Note the different scale for the green and red arrows. (b) Objective interpolation of average currents in (a). Thick black lines show predefined sections. Black contours show the 800 and 1,500 m isobath.

4.7. Historical Data

Recent changes reported in the general hydrography and sea ice conditions of the Arctic Ocean motivate a comparison of our observations to the last decades. In Figure 9 we compare our summer through fall average hydrography (Figure 9a) to average hydrography from the last decade (Figure 9b) and pre-2008 data (Figure 9c), including relative u_z calculated from the obtained Θ and S_A sections. Historical data from June to November were binned in 5 km horizontal bins before interpolating and finally smoothed using a 20 m by 20 km (vertical by horizontal) moving average. Lacking velocity observations, we choose a common cross-slope width of AW between -40 and 40 km (between the 2,060 m and 110 m isobaths respectively on our average bathymetry) to compare the average AW properties (Table 3). Heat content is calculated as described in section 3.5, and salt content is calculated (instead of an ambiguous fresh water content) following Schauer and Losch (2019).

Heat and salt content in our summer-fall 2018 observations are between the values inferred for the past decade and pre-2008. The average AW layer during the past decade stands out as particularly warm and salty. However, we note that average Θ in the AW layer is nearly the same in our observations as the past decade and that the difference in heat content is due to a thicker AW layer during the past decade. The average S_A in the AW layer is the same in our observations as pre-2008. The two-core structure observed in our data has a stronger resemblance in the past decade than pre-2008, potentially related to a shrinking sea ice cover and stronger atmospheric forcing.

5. Discussion

5.1. Average Transport and Seasonality

We observed an average AW volume transport of 2.6 ± 0.2 Sv from our measurements from summer to late fall and between 12°E and 24°E north of Svalbard. From a cruise in September 2013, Pérez-Hernández et al. (2017) observed an AW volume transport of 2.3 ± 0.3 Sv farther east, between 21°E and 33°E . The transport estimated from a mooring array at 30°E during 2013, averaged over the open water season to be comparable to our measurements, was 2.4 ± 0.1 Sv (Pérez-Hernández et al., 2019). We note that the

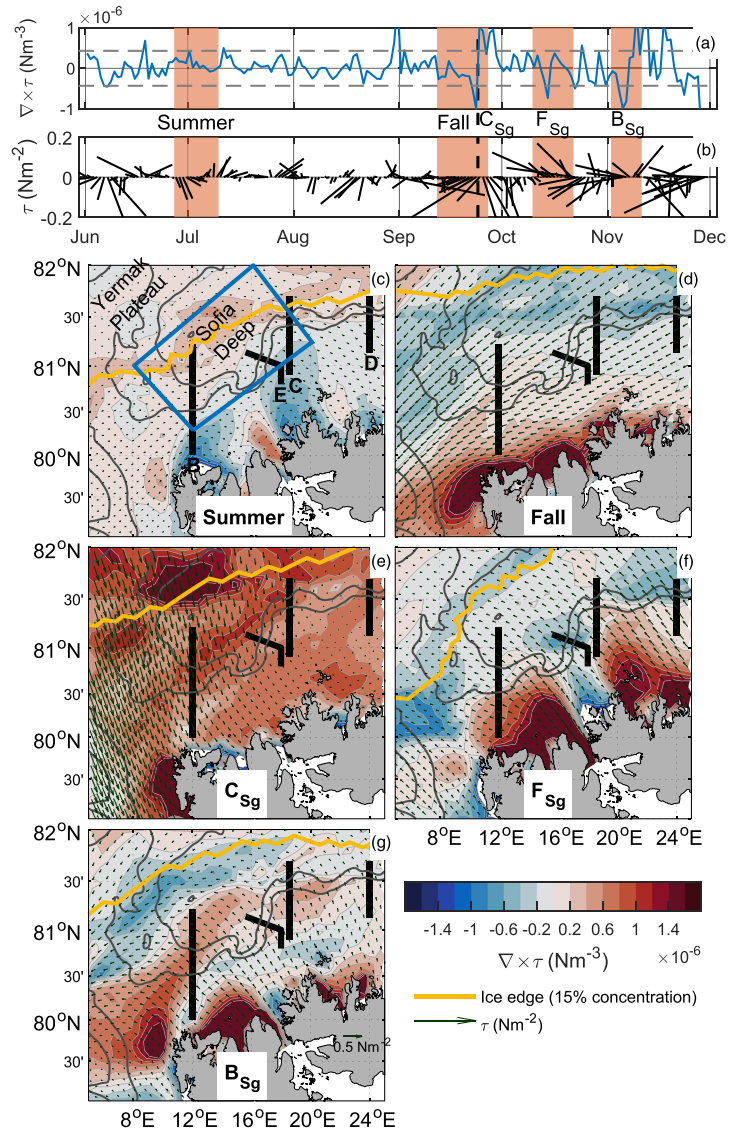


Figure 8. (a) Daily mean wind stress curl ($\nabla \times \tau$) averaged over the blue box shown in (c). Highlighted time periods indicate the times of the cruises and the Seaglider transects. Dashed black line separates the fall cruise from Seaglider transect C_{Sg}. Dashed gray lines indicate the root-mean-squared value. (b) Daily mean wind stress (τ) and wind stress direction averaged over the box in (c). c–g) Mean atmospheric conditions during the different cruises and Seaglider transects. Solid black lines indicate the predefined sections. Solid gray lines are the 800 and 1,500 m isobaths.

definition of AW used by Pérez-Hernández et al. (2017, 2019) differs from ours in the temperature criterion: They use $\Theta > 1$, whereas we use $\Theta > 2$. Our average AW volume transport estimate increases to 3.0 ± 0.2 Sv when the same definition as Pérez-Hernández et al. (2017, 2019) is used, that is, larger by 0.7 Sv than in

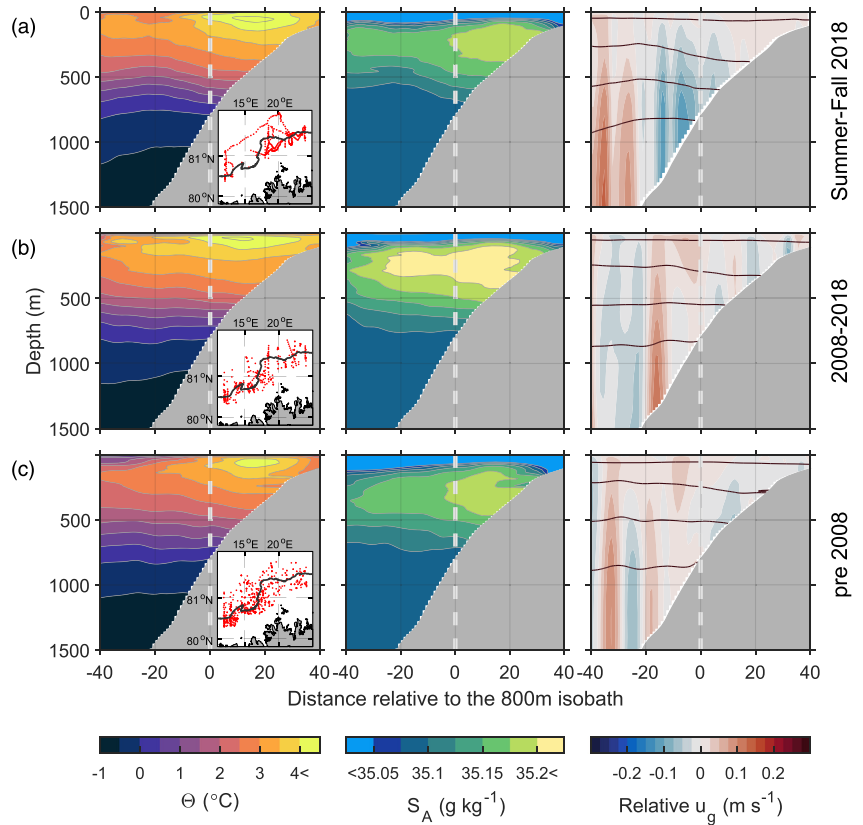


Figure 9. (a) Average composite sections, same as Figure 5a, but with relative u_g . (b) Average Θ , S_A , and relative u_g during June–November for the last 10 years (2008–2018). (c) Average Θ , S_A , and relative u_g during June–November for pre-2008. Black lines are isopycnals. The maps in the Θ plots show the CTD stations used for compiling the respective plots. The historical CTD data were fitted onto our average bathymetry similar to our composite sections.

Pérez-Hernández et al. (2019). However, the average volume transports reported by Pérez-Hernández et al. (2017, 2019) are observed further east than our sampling region, and we expect AW to gradually cool downstream. In addition, the mooring array at 30°E is located east of the Kvitøya Trough, where AW is known to enter and mix with colder shelf waters (Pérez-Hernández et al., 2017). Hence, our original temperature threshold estimate may be directly compared, which then agrees with the 2013 estimates to within errorbars. Nonetheless, this agreement can be fortuitous as we note that Våge et al. (2016) and Kolås and Fer (2018) reported smaller AW volume transports (1.6 ± 0.3 Sv and 1.3 Sv, respectively), which emphasizes the large volume transport variability observed north of Svalbard.

The boundary current north of Svalbard has a strong seasonal signal. We observed a 1 ± 0.3 Sv increase in the AW inflow from summer to fall, with a maximum of 3 Sv in October. This is comparable to the seasonality observed by the mooring array at 30°E (Pérez-Hernández et al., 2019). In the same period, we observed an increase in the velocity-weighted average AW temperature by $0.4 \pm 0.2^\circ\text{C}$, which is less than the

Table 3
Calculations of Laterally and Vertically Integrated Heat and Salt Content Within AW Between –40 and 40 km

	Summer-fall 2018	2008–2018	Pre-2008
AW area (km ²)	27	29	24
$\bar{\Theta}$ (°C)	3.19	3.21	2.85
\bar{S}_A (g kg ⁻¹)	35.15	35.17	35.15
Heat content (10 ¹⁴ J m ⁻¹)	3.5	3.8	2.8
Salt content (10 ⁸ kg m ⁻¹)	9.6	10.5	8.5

Note. Calculations are based on the hydrography presented in Figure 9.

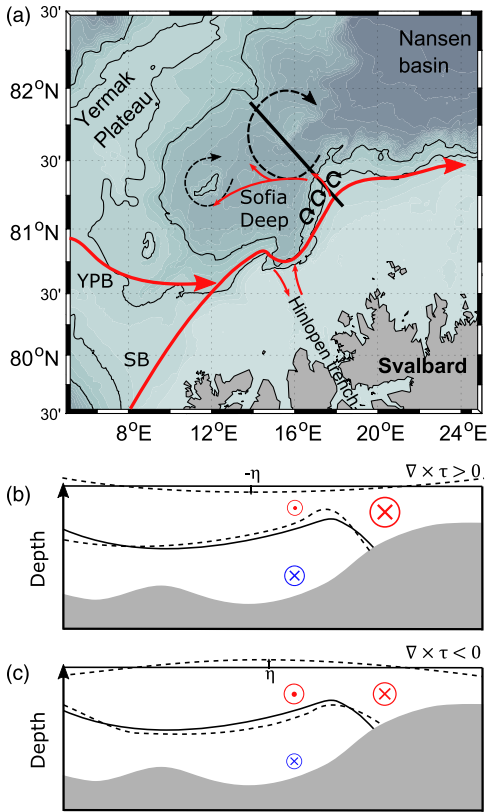


Figure 10. (a) Red arrows show the AW circulation in the study region. Black dashed arrows show possible anticyclonic circulation in the Sofia Deep. Small black arrows mark the possible generation site for eddies. The black line is the transect sketched in (b) and (c). Response of the circulation strength, sea level, and interface between the Atlantic Water and deeper water masses, to (b) a positive and (c) a negative wind stress curl in the Sofia Deep. For (b) and (c), solid line is the normal state, dashed line is perturbation from the wind stress curl.

0.84°C seasonal change observed by Pérez-Hernández et al. (2019). The seasonality of the AW inflow north of Svalbard is highly correlated with the volume transport of the WSC (Lique & Steele, 2012) and should be distinguished from the short-term and spatial variability north of Svalbard.

5.2. Spatial and Short-Term Variability

We observe large spatial and short-term variability in our synoptic sections north of Svalbard. Most noteworthy are the changes in volume transport of AW from section C (1.9 Sv) to D (1.4 Sv) and between C (1.9 Sv) and C_{Sg} (3.5 Sv). The change from C to D is likely partially explained by modification of AW due to heat loss to colder surrounding water and partially by the lack of observations on the shelf (Figure 3d). The change between sections C and C_{Sg} , only 5 days apart, tells a different story. There is a flow reversal on the shallow side of the first transect (Figure 3c); however, the reversal transport is only 0.1 Sv and does not explain why u_g in the entire AW layer is intensified during the second transect (Figure 3f). We suggest this increase in transport is related to the wind stress curl (section 4.6).

During the few days between conducting sections C and C_{Sg} , the average $\nabla \times \tau$ over the Sofia Deep changed from strongly negative (-10^6 N m^{-3}) to strongly positive (10^6 N m^{-3}) (Figure 8a). A schematic of expected response to anomalous wind stress curl events in the Sofia Deep is shown in Figures 10b and 10c. A negative $\nabla \times \tau$ event in the Sofia Deep would increase the sea surface height, η , in the Sofia Deep and decrease it on the continental shelf, thus act to weaken the AW boundary current. This is the effect we observed along section C during the Fall cruise (Figure 8d), where the boundary current weakened enough to cause a reversal on the shelf (Figure 3c). A positive $\nabla \times \tau$ event would have the opposite effect, decreasing η in the Sofia Deep and increasing η on the shelf, intensifying the boundary current and increasing the transport. This is the effect we observed a few days later during the Seaglider transect C_{Sg} (Figure 3f), following the abrupt change in wind stress curl (Figure 8e). Studies in the Chukchi Sea and Beaufort Sea show that η lags the onset of τ by about a day and that the geostrophic response to η , the balance between the pressure gradient force and Coriolis follows the change in η without any lag (Li et al., 2019; Lin et al., 2019). The geostrophic response to a change in η can be $\mathcal{O}(10) \text{ cm s}^{-1}$ and can be strong enough to cause a reversal in the average flow (Lin et al., 2019). A similar mechanism has also been observed on the West Spitsbergen Shelf where winter cyclones are known to accelerate and widen the West Spitsbergen Current (Nilsen et al., 2016).

5.3. Bottom-Intensified Current and the AW Recirculation

The complex bathymetry in the region affects the circulation patterns. In addition to the AW boundary current, approximately centered at the 800 m isobath, we observe two features not previously discussed in literature, yet supported by previous observations. One is the westward flowing AW along the southern rim of the Sofia Deep (Figure 7), hereby referred to as the AW recirculation. The other feature is the bottom-intensified current following the continental slope roughly between the 1,500 and 1,800 m isobaths.

The bottom-intensified current on the lower continental slope is observed along sections B, C, and E (Figures 3a–3c). The slope of isopycnals in the deeper part of the Seaglider sections suggests the presence of a bottom-intensified current (Figures 3e–3g); however, the glider does not extend deep enough to resolve the current. This outer bottom-intensified current is seen in all composite sections, as well as the seasonal average (Figure 5) and is distinct in the volumetric $\Theta - S_A$ diagram (Figure 6). The bottom-intensified current mainly consists of Arctic Intermediate Water, and to a lesser extent cold Norwegian Sea Deep Water and

Eurasian Basin Deep Water (Figure 6). These water masses are common in the Eurasian Basin. Our water mass definitions are based on earlier work and recent changes in the Arctic Ocean could potentially affect the water mass limits.

Revisiting earlier published observations from this region, we note that bottom-intensified currents were occasionally measured north of Svalbard. In one of their transects, Våge et al. (2016) observed a bottom-intensified current along 30°E but did not further discuss it. Pérez-Hernández et al. (2017) discussed a bottom intensification of the AW layer as the AW meandered seawards but did not show any bottom intensification in the deeper parts. Our analysis of historical hydrographic observations from north of Svalbard suggests that the bottom-intensified flow near 1,500 m depth is a robust feature (Figure 9), both during the last decade and pre-2008, although its location on the slope may vary.

The bottom-intensified current and the AW boundary current are separated by shoaling deep isopycnals; see the black density lines in the composite sections (Figures 4 and 5). The positive isopycnal slope seaward of the bottom-intensified current is due to colder and saltier water found further up in the water column near the continental shelf than further out in the basin. This must be caused by either lifting the colder water up slope or depressing the water in the basin. Subinertial vorticity waves (e.g., coastal or topographically trapped waves), low frequency internal waves, or wind-induced upwelling could move deep, cold waters upslope; however, because the observations are robust in all composites (as well as in the multiyear averaged historical data), a local, transient lifting mechanism seems unlikely. Instead, we suggest the deeper isopycnals are being depressed in the Sofia Deep by an average anticyclonic circulation. The southern edge of this is captured by the negative geostrophic velocity near the deep end of our sections (Figure 3) and by the westward currents along the Seaglider track in the Sofia Deep (Figure 7). Cokelet et al. (2008) show an anticyclonic circulation in their section 3, crossing the Sofia Deep. They discuss the outer edges of their section as two separate domains and do not consider an anticyclonic circulation pattern. We propose these edges are likely linked and potentially related dynamically to the seamounts in the Sofia Deep. The isopycnals along section 3 of Cokelet et al. (2008) spread in the middle, supporting such an anticyclonic circulation.

However, our observations differ somewhat from those by Cokelet et al. (2008). They observed mostly barotropic currents, whereas we observe a baroclinic flow with the upper AW layer flowing westward and the deeper water flowing eastward. One reason for this difference may be that our higher resolution observations capture stronger cross-slope density gradients. The cross-slope density gradient may also be affected by the wind stress curl, thus periodically changing the strength of the bottom-intensified current.

The strength of the AW recirculation and the bottom-intensified flow is likely affected by the wind forcing, similar to the boundary current (section 5.2). Positive $\nabla \times \tau$ would decrease the barotropic counter current, while negative $\nabla \times \tau$ would increase it. In addition to the transient geostrophic set-up effect, a prolonged wind stress curl event in the Sofia Deep could cause upwelling or downwelling on the continental slope, affecting the isopycnal gradient and the strength of the bottom-intensified current (Figures 10b and 10c). Finally, upwelling will act to pull up the isopycnals separating the AW boundary current and the opposing flow, potentially creating a density barrier between the two. When the density barrier is strong, that is, prolonged positive $\nabla \times \tau$, we expect less interaction between the AW boundary current and the counter flow, whereas when the density barrier is weakened, that is, prolonged negative $\nabla \times \tau$, we expect more AW water to spread laterally.

Along our Seaglider track in the Sofia Deep, we do not observe one continuous AW layer but instead patches of AW with variable layer thickness and spreading isopycnals, suggesting several anticyclonic eddies (not shown). Thus it is likely that AW is not continuously fed into the anticyclonic circulation in the Sofia Deep but instead released from the AW boundary current as eddies.

Our interpretation finds support from numerical models and other observations. An eddy-resolving model (FESOM_1km) was used by Wekerle et al. (2017) to simulate the layer-averaged AW velocity for the region west and north of Svalbard in the period 2001–2009. Their results show a westward flowing current north of the eastward flowing boundary current (extending as far as 31°E) and an anticyclonic circulation in the Sofia Deep, supporting our observations. We also note that an average hydrographic section (constructed from eight cross-slope transects) near 31°E north of Svalbard shows an outer westward-flowing branch containing AW with a local salinity maximum (Pérez-Hernández et al., 2017).

An alternative hypothesis could be that our observations capture the southern edge of a standing eddy (not resolved with our data), possibly being fed by the anticyclones shed from the instability of the boundary current. It is common that the steepening slope, such as in our region, allow generation of eddies through baroclinic, barotropic or mixed instabilities (Dugstad et al., 2019; Isachsen, 2015). An example of such an eddy is the permanent Lofoten Basin eddy observed in the Norwegian Sea (see Bosse et al., 2019, and the references therein).

5.4. Method Sensitivity

In most of our observations, spatial variability and day-to-day variability cannot be distinguished. To complete a section, ship uses about a day, whereas the Seaglider uses several days. The variability captured along such a section is a combination of spatial and temporal variability. Several transects along the same section are needed to resolve such variability.

As we lacked repeated sections for most of our transects, a comparison between different cruises and different data sets is difficult. For that reason we decided to compile composite sections (as described in Section 3.3) even though the topography in the region is complex. However, moving the original data location along isobaths onto a section normal to the 800 m isobath can potentially change the horizontal temperature and salinity gradients, thus influencing the geostrophic velocity calculations. For example, if we calculate the average AW volume transport from a composite section consisting of only CTD stations along sections C and D, we obtain 2.4 ± 0.2 Sv, although the volume transport through sections C and D is only 1.9 and 1.4 Sv, respectively (Table 1). In this case our average bathymetry is not representative of the average slope along sections C and D and produces unrealistically large cross-slope gradients. Our average bathymetry is an average over the entire continental slope between 12°E and 24°E north of Svalbard and is chosen in order to minimize the change in horizontal gradient when the CTD stations used for the composite represent the same region.

Although the sections were carefully chosen in order to minimize the change in horizontal gradient, we tested the sensitivity by using an alternative method for calculating the Seaglider section F_{Sg} , which has a substantial scatter of station locations (Figure 1). Instead of moving data along isobaths we interpolated the data at their original location onto 1 dbar level grids, before choosing a section across the isobaths, roughly in the middle of our data cluster. This method increased the volume transport across the section by about 10%. In addition, throughout our analysis we have interpolated our sections onto a 1 km horizontal grid. Decreasing the horizontal resolution from 1 to 5 km reduced the transport by about 15%. However, a 5 km horizontal resolution is coarser than the ship's station resolution through the center of the core and is a too low resolution for realistic core transport estimates.

6. Summary

We analyzed hydrographic and current observations from two scientific cruises, one Seaglider mission and two Argo floats, during summer and fall 2018, north of Svalbard (Figure 1). We presented the data as synoptic sections, composite sections, and depth-averaged currents in order to resolve short-term variability, intra-seasonal variability, and general circulation.

We suggest the AW circulation pattern presented in Figure 10a. Our observations showed the AW boundary current into the Arctic, following the 800 m isobath. North of the AW boundary current we observed an AW recirculation in the Sofia Deep, a return flow containing a separate patch of AW, overlaying an eastward flowing bottom-intensified current (Figures 4 and 5).

The boundary current north of Svalbard between 12°E and 24°E is highly variable both in time and space. We observed an average AW transport of 2.6 ± 0.2 Sv into the Arctic (Table 1). From summer to fall, the average AW transport increased from 2.0 ± 0.1 Sv to 3.0 ± 0.2 Sv, with a maximum in October. The short-term variations were even larger, for example two transects along the same section, only 5 days apart, showed an increase in AW transport from 1.9 to 3.5 Sv. This increase was caused by an abrupt change in wind stress curl from negative to positive in the Sofia Deep, strengthening the AW boundary current.

Figures 10b and 10c summarize the likely response to anomalous wind stress curl events in the Sofia Deep. A negative $\nabla \times \tau$ event (Figure 10c) in the Sofia Deep weakens the AW boundary current through a geostrophic

set-up effect and could potentially overcome the boundary current and lead to a reversal on the shelf (section C during the Fall cruise, Figure 3c). A positive $\nabla \times \tau$ event (Figure 10b) would have the opposite effect, intensify the boundary current and increase its transport (as in the Seaglider transect C_{Sg} , Figure 3f).

Also the strength of the return flow and the bottom-intensified flow is likely affected by the wind forcing, similar to the boundary current. In addition to a transient geostrophic set-up effect, a prolonged wind stress curl event in the Sofia Deep could cause upwelling or downwelling on the continental slope, modulating the isopycnal gradient and the strength of the bottom-intensified current (Figures 10b and 10c).

Finally, we note that section C, near 18°E, is a likely generation site for eddies that detach from the boundary current and are transported into the Sofia Deep. Signatures of multiple eddies were found along the Seaglider transect crossing the Sofia Deep and will be the subject of future analyses. Our data suggest the presence of an average anticyclonic circulation in the Sofia Deep, likely around each of the seamounts. However, the mechanism maintaining such an anticyclonic circulation is unclear and merits further studies.

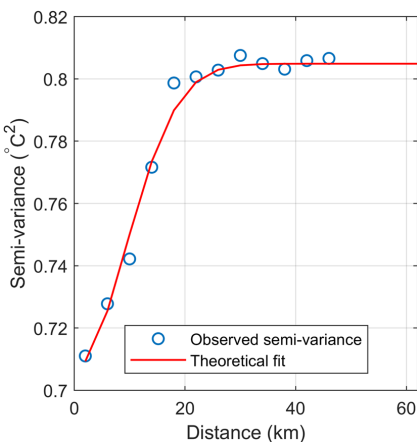
Appendix A: Average Bathymetry for Composite Sections

Following a method similar to Fratantoni and Pickart (2007), we construct a composite section. Using full resolution data from IBCAO v3, we extracted bottom topography data along 30 sections normal to the 800 m isobath north of Svalbard, between 11°E and 24°E. Coordinates were transformed into Cartesian (x,z) coordinates, and the bottom data along the sections were interpolated onto a 1 km horizontal resolution grid. Next we calculated the inverse slope $[(dz/dx)^{-1}]$ and removed all points where the inverse slope was above 0, or less than -0.35 (vertical m/horizontal km) $^{-1}$. The median depth and median inverse slope were calculated for 50 m vertical bins between 150 and 2,500 m depth. We use the median instead of the average in order to exclude some outliers. For each bin, the inverse slope was multiplied by dz in order to obtain the horizontal displacement, dx . Finally, dx was summed and referenced to the horizontal location of the 800 m isobath. In our sections, negative dx is toward deep water and positive toward shallow waters.

When generating the composite sections, the following stations were excluded. For the summer cruise, data from the three southern-most stations along sections B and C required tens of kilometers relocation to fit the average bottom and were excluded. The southern-most station along section D and the northernmost station along section B were removed for both cruises because the bottom slope changes sign.

Appendix B: Error Calculations

For each section we subtracted the gridded section field from our measurements, retaining the residuals. Pairwise semivariance (variance divided by two) between the residuals was plotted against horizontal distance between the pairs of the residuals, obtaining a so-called semivariogram. An example is shown in Figure B1. Next, we fitted a Gaussian variogram model to our empirical variogram using the following equation (ch. 2.4 Cressie, 1993):



$$\gamma(d) = (\sigma^2 - \nu) \left(1 - \exp\left(-3\frac{d^2}{r^2}\right) \right) + \nu \quad (B1)$$

where σ^2 is the saturation value at which the variogram stabilises (the sill), r is the distance where the variogram reaches the sill, ν is the zero-crossing value of the variogram, and d is the distance between the pairs of residuals. Knowing the horizontal distance between any grid point in our gridded field and the closest measurement, we computed semivariance matrices. Instrumental errors were added to the variance before taking the square root, obtaining the one-sided standard deviation at any grid point. One thousand Gaussian distributed random error matrices, using the obtained standard deviation, were added to each section, including composite sections. Reported errors are the root-mean-square of the difference between calculations from the original gridded field and each of the fields including the random error

Figure B1. Variogram showing semivariance of Θ versus distance between residuals.

matrices. For Θ , S_A and volume transport, the errors are rounded up to the nearest 0.1°C , 0.01 g kg^{-1} , and 0.1 Sv , respectively.

Data Availability Statement

All data are available from the Norwegian Marine Data Centre; data sets from the July cruise (KB 2018616) are available at <https://doi.org/10.21335/NMDC-2047975397>, data sets from the September cruise (KH 2018709) are available at <https://doi.org/10.21335/NMDC-2039932526>, and the glider data are available online (<https://doi.org/10.21335/NMDC-1841837601>). The historical data are available from the University Centre in Svalbard (<https://doi.org/10.21334/unis-hydrography>). The ice edge data are available online (https://thredds.met.no/thredds/osisaf/osisaf_seaiceedge.html). Argo float data are available from <https://argo.jcommops.org>, using the identification numbers 6903548 and 3901910.

Acknowledgments

This work was supported by the Nansen Legacy Project, project number 276730. We thank the officers, crew and scientist of the *RV Kristine Bonnevie* cruise in July 2018 and of the *RV Kronprins Haakon* cruise in September 2018. We thank the glider team at NorGliders (<http://norgliders.gfi.uib.no/>). We thank two anonymous reviewers whose comments helped improve a previous version of this paper.

References

- Aagaard, K., Foldvik, A., & Hillman, S. R. (1987). The West Spitsbergen Current: Disposition and water mass transformation. *Journal of Geophysical Research*, *92*(C4), 3778. <https://doi.org/10.1029/jc092ic04p03778>
- Aagaard, K., Swift, J. H., & Carmack, E. C. (1985). Thermohaline circulation in the Arctic Mediterranean Seas. *Journal of Geophysical Research*, *90*(C3), 4833–4846. <https://doi.org/10.1029/jc090ic03p04833>
- Böhme, L., & Send, U. (2005). Objective analyses of hydrographic data for referencing profiling float salinities in highly variable environments. *Deep Sea Research Part II: Topical Studies in Oceanography*, *52*(3–4), 651–664. <https://doi.org/10.1016/j.dsr2.2004.12.014>
- Beszczynska-Möller, A., Fahrback, E., Schauer, U., & Hansen, E. (2012). Variability in Atlantic water temperature and transport at the entrance to the Arctic Ocean, 1997–2010. *ICES Journal of Marine Science*, *69*(5), 852–863. <https://doi.org/10.1093/icesjms/iss056>
- Bosse, A., Fer, I., Lilly, J. M., & Soiland, H. (2019). Dynamical controls on the longevity of a non-linear vortex: The case of the Lofoten Basin Eddy. *Scientific Reports*, *9*(1), 13448. <https://doi.org/10.1038/s41598-019-49599-8>
- Bourke, R. H., Weigel, A. M., & Paquette, R. G. (1988). The westward turning branch of the West Spitsbergen Current. *Journal of Geophysical Research*, *93*(C11), 14065. <https://doi.org/10.1029/jc093ic11p14065>
- Boyd, T. J., & D'Asaro, E. A. (1994). Cooling of the West Spitsbergen Current: Wintertime observations West of Svalbard. *Journal of Geophysical Research*, *99*(C11), 22,597–22,618. <https://doi.org/10.1029/94jc01824>
- Carmack, E., Polyakov, I., Padman, L., Fer, I., Hunke, E., Hutchings, J., et al. (2015). Toward quantifying the increasing role of oceanic heat in sea ice loss in the New Arctic. *Bulletin of the American Meteorological Society*, *96*(12), 2079–2105. <https://doi.org/10.1175/bams-d-13-00177.1>
- Cokelet, E. D., Tervalon, N., & Bellingham, J. G. (2008). Hydrography of the West Spitsbergen Current, Svalbard Branch: Autumn 2001. *Journal of Geophysical Research*, *113*, C01006. <https://doi.org/10.1029/2007jc004150>
- Cressie, N. A. C. (1993). *Statistics for spatial data* (2nd ed.). New York: Wiley-Interscience Publication.
- Crews, L., Sundfjord, A., Albretsen, J., & Hattermann, T. (2018). Mesoscale eddy activity and transport in the Atlantic water inflow region north of Svalbard. *Journal of Geophysical Research: Oceans*, *123*, 201–215. <https://doi.org/10.1002/2017JC013198>
- Crews, L., Sundfjord, A., & Hattermann, T. (2019). How the Yermak Pass Branch regulates Atlantic water inflow to the Arctic Ocean. *Journal of Geophysical Research: Oceans*, *124*, 267–280. <https://doi.org/10.1029/2018JC014476>
- Dugstad, J., Fer, I., LaCasce, J., de La Lama, M. S., & Trodahl, M. (2019). Lateral heat transport in the Lofoten Basin: Near-surface pathways and subsurface exchange. *Journal of Geophysical Research: Oceans*, *124*, 2992–3006. <https://doi.org/10.1029/2018jc014774>
- Erofeeva, S., & Egbert, G. (2020). Arc5km2018: Arctic Ocean inverse tide model on a 5 kilometer grid, 2018. Arctic Data Center. <https://doi.org/10.18739/A21R6N14K>
- Fer, I., Koenig, Z., Bosse, A., Falck, E., Kolås, E., & Nilsen, F. (2020). *Physical oceanography data from the cruise KB 2018616 with R.V. Kristine Bonnevie*. Bergen: University of Bergen. <https://doi.org/10.21335/NMDC-2047975397>
- Fer, I., Koenig, Z., Kolås, E., Falck, E., Fossum, T., Ludvigsen, M., et al. (2019). *Physical oceanography data from the cruise KH 2018709 with R.V. Kronprins Haakon, 12–24 September 2018*. Bergen: University of Bergen. <https://doi.org/10.21335/NMDC-2039932526>
- Fer, I., Skogseth, R., & Geyer, F. (2010). Internal waves and mixing in the marginal ice zone near the Yermak Plateau. *Journal of Physical Oceanography*, *40*(7), 1613–1630. <https://doi.org/10.1175/2010jp04371.1>
- Firing, E., & Ranada, J. (1995). Processing ADCP data with the CODAS software system version 3.1. [Computer software manual].
- Frajka-Williams, E., Eriksen, C. C., Rhines, P. B., & Harcourt, R. R. (2011). Determining vertical water velocities from Seaglider. *Journal of Atmospheric and Oceanic Technology*, *28*(12), 1641–1656. <https://doi.org/10.1175/2011jtecho830.1>
- Fratantoni, P. S., & Pickart, R. S. (2007). The Western North Atlantic shelfbreak current system in summer. *Journal of Physical Oceanography*, *37*(10), 2509–2533. <https://doi.org/10.1175/jpo3123.1>
- Garau, B., Ruiz, S., Zhang, W. G., Pascual, A., Heslop, E., Kerfoot, J., & Tintoré, J. (2011). Thermal lag correction on Slocum CTD glider data. *Journal of Atmospheric and Oceanic Technology*, *28*(9), 1065–1071. <https://doi.org/10.1175/jtech-d-10-05030.1>
- Gascard, J.-C., Richez, C., & Rouault, C. (2013). New insights on large-scale oceanography in Fram Strait: The West Spitsbergen current. In *Arctic oceanography: Marginal ice zones and continental shelves* (pp. 131–182). Washington, DC: American Geophysical Union. <https://doi.org/10.1029/CE049p0131>
- Hattermann, T., Isachsen, P. E., von Appen, W.-J., Albretsen, J., & Sundfjord, A. (2016). Eddy-driven recirculation of Atlantic Water in Fram Strait. *Geophysical Research Letters*, *43*, 3406–3414. <https://doi.org/10.1002/2016gl068323>
- IOC, SCOR, & IAPSO (2010). The international thermodynamic equation of seawater 2010: Calculations and use of thermodynamic properties (Intergovernmental Oceanographic Commission, Manuals and Guides No. 56 ed.). [Computer software manual]. UNESCO.
- International Argo Program (2003). Temperature, salinity, pressure, and biogeochemical profile data from globally distributed Argo profiling floats, by month since April 2003 for the Global Argo Data Repository, containing data from 1995-09-07 to present. [WMO Id 6903548 and 3901910]. NOAA National Centers for Environmental Information. Dataset. (Accessed on 15.11.2019) <https://doi.org/10.25921/q97e-d719>

- Isachsen, P. E. (2015). Baroclinic instability and the mesoscale eddy field around the Lofoten Basin. *Journal of Geophysical Research: Oceans*, *120*, 2884–2903. <https://doi.org/10.1002/2014jc010448>
- Jakobsson, M., Mayer, L., Coakley, B., Dowdeswell, J. A., Forbes, S., Fridman, B., et al. (2012). The International Bathymetric Chart of the Arctic Ocean (IBCAO) Version 3.0. *Geophysical Research Letters*, *39*, L12609. <https://doi.org/10.1029/2012gl052219>
- Koenig, Z., Provost, C., Sennéchal, N., Garric, G., & Gascard, J.-C. (2017). The Yermak Pass Branch: A major pathway for the Atlantic water north of Svalbard? *Journal of Geophysical Research: Oceans*, *122*, 9332–9349. <https://doi.org/10.1002/2017jc013271>
- Kolås, E., & Fer, I. (2018). Hydrography, transport and mixing of the West Spitsbergen Current: The Svalbard Branch in summer 2015. *Ocean Science*, *14*(6), 1603–1618. <https://doi.org/10.5194/os-14-1603-2018>
- Kolås, E., & Fer, I. (2020). *Physical oceanography data from a Seaglider mission north of Svalbard, late fall 2018*. Bergen: University of Bergen. <https://doi.org/10.21335/NMDC-1841837601>
- Large, W. G., & Pond, S. (1981). Open ocean momentum flux measurements in moderate to strong winds. *Journal of Physical Oceanography*, *11*(3), 324–336.
- Li, M., Pickart, R. S., Spall, M. A., Weingartner, T. J., Lin, P., Moore, G. W. K., & Qi, Y. (2019). Circulation of the Chukchi Sea shelfbreak and slope from moored timeseries. *Progress in Oceanography*, *172*, 14–33. <https://doi.org/10.1016/j.pocean.2019.01.002>
- Lin, P., Pickart, R. S., Moore, G. W. K., Spall, M. A., & Hu, J. (2019). Characteristics and dynamics of wind-driven upwelling in the Alaskan Beaufort Sea based on six years of mooring data. *Deep Sea Research Part II: Topical Studies in Oceanography*, *162*, 79–92. <https://doi.org/10.1016/j.dsr2.2018.01.002>
- Lique, C., & Steele, M. (2012). Where can we find a seasonal cycle of the Atlantic water temperature within the Arctic Basin? *Journal of Geophysical Research*, *117*, C03026. <https://doi.org/10.1029/2011JC007612>
- Manley, T. O. (1995). Branching of Atlantic Water within the Greenland-Spitsbergen Passage: An estimate of recirculation. *Journal of Geophysical Research*, *100*(C10), 20627. <https://doi.org/10.1029/95jc01251>
- Marnela, M., Rudels, B., Houssais, M.-N., Beszczynska-Möller, A., & Eriksson, P. B. (2013). Recirculation in the Fram Strait and transports of water in and north of the Fram Strait derived from CTD data. *Ocean Science*, *9*(3), 499–519. <https://doi.org/10.5194/os-9-499-2013>
- McDougall, T. J. (2003). Potential enthalpy: A conservative oceanic variable for evaluating heat content and heat fluxes. *Journal of Physical Oceanography*, *33*(5), 945–963. [https://doi.org/10.1175/1520-0485\(2003\)033<0945:PEACOV>2.0.CO;2](https://doi.org/10.1175/1520-0485(2003)033<0945:PEACOV>2.0.CO;2)
- McDougall, T. J., & Barker, P. M. (2011). Getting started with TEOS-10 and the Gibbs Seawater (GSW) oceanographic toolbox. SCOR/IAPSO WG127, 28 pp.
- Menze, S., Ingvaldsen, R. B., Haugan, P., Fer, I., Sundfjord, A., Beszczynska-Möller, A., & Falk-Petersen, S. (2019). Atlantic water pathways along the north-western Svalbard shelf mapped using vessel-mounted current profilers. *Journal of Geophysical Research: Oceans*, *124*, 1699–1716. <https://doi.org/10.1029/2018jc014299>
- Meyer, A., Fer, I., Sundfjord, A., & Peterson, A. K. (2017). Mixing rates and vertical heat fluxes north of Svalbard from Arctic winter to spring. *Journal of Geophysical Research: Oceans*, *122*, 4569–4586. <https://doi.org/10.1002/2016jc012441>
- Meyer, A., Sundfjord, A., Fer, I., Provost, C., Robineau, N. V., Koenig, Z., et al. (2017). Winter to summer oceanographic observations in the Arctic Ocean north of Svalbard. *Journal of Geophysical Research: Oceans*, *122*, 6218–6237. <https://doi.org/10.1002/2016jc012391>
- Nilsen, F., Skogseth, R., Vaardal-Lunde, J., & Inall, M. (2016). A simple shelf circulation model: Intrusion of Atlantic water on the west Spitsbergen shelf. *Journal of Physical Oceanography*, *46*(4), 1209–1230. <https://doi.org/10.1175/jpo-d-15-0058.1>
- Onarheim, I. H., Smedsrud, L. H., Ingvaldsen, R. B., & Nilsen, F. (2014). Loss of sea ice during winter north of Svalbard. *Tellus A: Dynamic Meteorology and Oceanography*, *66*(1), 23,933–23,941. <https://doi.org/10.3402/tellusa.v66.23933>
- Pérez-Hernández, M. D., Pickart, R. S., Pavlov, V., Våge, K., Ingvaldsen, R., Sundfjord, A., et al. (2017). The Atlantic water boundary current north of Svalbard in late summer. *Journal of Geophysical Research: Oceans*, *122*, 2269–2290. <https://doi.org/10.1002/2016jc012486>
- Pérez-Hernández, M. D., Pickart, R. S., Torres, D. J., Bahr, F., Sundfjord, A., Ingvaldsen, R., et al. (2019). Structure, transport and seasonality of the Atlantic water boundary current north of Svalbard: Results from a year-long mooring array. *Journal of Geophysical Research: Oceans*, *124*, 1679–1698. <https://doi.org/10.1029/2018jc014759>
- Perkin, R. G., & Lewis, E. L. (1984). Mixing in the west Spitsbergen current. *Journal of Physical Oceanography*, *14*(8), 1315–1325. [https://doi.org/10.1175/1520-0485\(1984\)014<1315:MITWSC>2.0.CO;2](https://doi.org/10.1175/1520-0485(1984)014<1315:MITWSC>2.0.CO;2)
- Pickart, R. S., & Smethie, W. M. (1998). Temporal evolution of the deep western boundary current where it enters the sub-tropical domain. *Deep Sea Research Part I: Oceanographic Research Papers*, *45*(7), 1053–1083. [https://doi.org/10.1016/s0967-0637\(97\)00084-8](https://doi.org/10.1016/s0967-0637(97)00084-8)
- Polyakov, I. V., Pnyushkov, A. V., Alkire, M. B., Ashik, I. M., Baumann, T. M., Carmack, E. C., et al. (2017). Greater role for Atlantic inflows on sea-ice loss in the Eurasian Basin of the Arctic Ocean. *Science*, *356*(6335), 285–291. <https://doi.org/10.1126/science.aai8204>
- Reistad, M., Breivik, O., Haakenstad, H., Aarnes, O. J., Furevik, B. R., & Bidlot, J.-R. (2011). A high-resolution hindcast of wind and waves for the North Sea, the Norwegian Sea, and the Barents Sea. *Journal of Geophysical Research*, *116*, C05019. <https://doi.org/10.1029/2010jc006402>
- Rudels, B., Björk, G., Nilsson, J., Winsor, P., Lake, I., & Nohr, C. (2005). The interaction between waters from the Arctic Ocean and the Nordic Seas north of Fram Strait and along the East Greenland Current: Results from the Arctic Ocean-02 Oden expedition. *Journal of Marine Systems*, *55*(1-2), 1–30. <https://doi.org/10.1016/j.jmarsys.2004.06.008>
- Rudels, B., Muench, R. D., Gunn, J., Schauer, U., & Friedrich, H. J. (2000). Evolution of the Arctic Ocean boundary current north of the Siberian shelves. *Journal of Marine Systems*, *25*(1), 77–99. [https://doi.org/10.1016/s0924-7963\(00\)00009-9](https://doi.org/10.1016/s0924-7963(00)00009-9)
- Saloranta, T. M., & Haugan, P. M. (2004). Northward cooling and freshening of the warm core of the west Spitsbergen current. *Polar Research*, *23*(1), 79–88. <https://doi.org/10.3402/polar.v23i1.6268>
- Schauer, U., & Losch, M. (2019). Freshwater in the ocean is not a useful parameter in climate research. *Journal of Physical Oceanography*, *2019*, 2309–2321. <https://doi.org/10.1175/JP0-D-19-0102.1>
- Schlichtholz, P., & Houssais, M.-N. (2002). An overview of the θ - S correlations in Fram Strait based on the MIZEX 84 data. *Oceanologia*, *44*(2), 243–272.
- Seaglider Quality Control Manual (2012). (Version 1.11 ed.) [Computer software manual].
- Sirevaag, A., & Fer, I. (2009). Early spring oceanic heat fluxes and mixing observed from drift stations north of Svalbard. *Journal of Physical Oceanography*, *39*(12), 3049–3069. <https://doi.org/10.1175/2009jpo4172.1>
- Skogseth, R., Ellingsen, P., Berge, J., Cottier, F., Falk-Petersen, S., Ivanov, B., et al. (2019). *UNIS hydrographic database*. Tromsø: Norwegian Polar Institute. <https://doi.org/10.21334/unis-hydrography>
- Smith, W. H. F., & Wessel, P. (1990). Gridding with continuous curvature splines in tension. *Geophysics*, *55*(3), 293–305. <https://doi.org/10.1190/1.1442837>
- Swift, J. H., & Aagaard, K. (1981). Seasonal transitions and water mass formation in the Iceland and Greenland seas. *Deep Sea Research Part A. Oceanographic Research Papers*, *28*(10), 1107–1129. [https://doi.org/10.1016/0198-0149\(81\)90050-9](https://doi.org/10.1016/0198-0149(81)90050-9)

- Uppala, S. M., Kållberg, P. W., Simmons, A. J., Andreae, U., Da Costa Bechtold, V., Fiorino, M., et al. (2005). The ERA-40 re-analysis. *Quarterly Journal of the Royal Meteorological Society: A journal of the atmospheric sciences, applied meteorology and physical oceanography*, *131*(612), 2961–3012.
- Våge, K., Pickart, R. S., Pavlov, V., Lin, P., Torres, D. J., Ingvaldsen, R., et al. (2016). The Atlantic water boundary current in the Nansen Basin: Transport and mechanisms of lateral exchange. *Journal of Geophysical Research: Oceans*, *121*, 6946–6960. <https://doi.org/10.1002/2016jc011715>
- Visbeck, M. (2002). Deep velocity profiling using lowered acoustic Doppler current profilers: Bottom track and inverse solutions. *Journal of Atmospheric and Oceanic Technology*, *19*(5), 794–807. [https://doi.org/10.1175/1520-0426\(2002\)019<0794:DVPULA>2.0.CO;2](https://doi.org/10.1175/1520-0426(2002)019<0794:DVPULA>2.0.CO;2)
- von Appen, W.-J., Schauer, U., Hattermann, T., & Beszczynska-Möller, A. (2016). Seasonal cycle of mesoscale instability of the west Spitsbergen current. *Journal of Physical Oceanography*, *46*(4), 1231–1254. <https://doi.org/10.1175/jpo-d-15-0184.1>
- Wekerle, C., Wang, Q., von Appen, W.-J., Danilov, S., Schourup-Kristensen, V., & Jung, T. (2017). Eddy-resolving simulation of the Atlantic water circulation in the Fram Strait with focus on the seasonal cycle. *Journal of Geophysical Research: Oceans*, *122*, 8385–8405. <https://doi.org/10.1002/2017jc012974>

Paper II

Technical note: Turbulence measurements from a light autonomous underwater vehicle

Eivind Hugaas Kolås, Tore Mo-Bjørkelund and Ilker Fer

Ocean Science, **18(389-400)**, 2022

<https://doi.org/10.5194/os-18-389-2022>

II



Technical note: Turbulence measurements from a light autonomous underwater vehicle

Eivind H. Kolås¹, Tore Mo-Bjørkelund², and Ilker Fer^{1,3}

¹Geophysical Institute, University of Bergen and Bjerknes Center for Climate Research, Bergen, Norway

²Department of Marine Technology, Norwegian University of Science and Technology, Trondheim, Norway

³Department of Arctic Geophysics, UNIS – The University Centre in Svalbard, Longyearbyen, Norway

Correspondence: Eivind H. Kolås (eivind.kolas@uib.no)

Received: 3 November 2021 – Discussion started: 8 November 2021

Revised: 25 February 2022 – Accepted: 3 March 2022 – Published: 24 March 2022

Abstract. A self-contained turbulence instrument from Rockland Scientific was installed on a light autonomous underwater vehicle (AUV) from OceanScan Marine Systems and Technology Lda. We report on the data quality and discuss limitations of dissipation estimated from two shear probes during a deployment in the Barents Sea in February 2021. The AUV mission lasted for 5 h, operating at a typical horizontal speed of 1.1 m s^{-1} . The AUV was programmed to find and cross the maximum along-path thermal gradient at 10, 20 and 30 m depths along 4 km transects. Although the AUV vibrations contaminate the shear probe records, the noise is mitigated by removing vibration-induced components from shear spectra using the accelerometer signal measured in multiple directions. Dissipation rate estimates in the observed transects varied in the range 1×10^{-8} and $6 \times 10^{-6} \text{ W kg}^{-1}$, with the values from the two orthogonal probes typically in agreement to within a factor of 2. Dissipation estimates from the AUV show good agreement with nearby vertical microstructure profiles obtained from the ship during the transects, indicating that the turbulence measurements from the AUV are reliable for this relatively turbulent environment. However, the lowest reliable dissipation rates are limited to $5 \times 10^{-8} \text{ W kg}^{-1}$, making this setup unfit for use in quiescent environments.

ing evolution and transformation of water masses. The dissipation rate of turbulent kinetic energy provides the energy that homogenizes the gradients of temperature and salinity. Quantifying the magnitude and distribution of the dissipation rate helps identify the different forcing mechanisms and their relative contribution to mixing. In general, the necessary requirements for measuring ocean turbulence can be summed up in three elements: a sensor or probe that detects the physical parameter of interest, an electronic circuitry that amplifies and filters the signal produced by the probe, and a stable platform that is rigid or moves smoothly in the ocean (Lueck et al., 2002). Holding a probe stable while moving it smoothly through a dynamic ocean is not trivial. Ocean waves, currents and controlled platform adjustments will lead to platform motion and artificial signals not associated with natural turbulence.

The most common method for measuring ocean turbulence is to measure the small-scale velocity shear by using free-falling or loosely tethered vertical microstructure profilers equipped with airfoil shear probes (Lueck, 2005; Gregg, 2021). Such profilers are commonly deployed from vessels or drifting sea ice. However, the vertical profiling limits the horizontal and temporal resolution of the measurements. Robotic platforms offer the potential to increase the availability of ocean-mixing measurements (Frajka-Williams et al., 2022). Robotic platforms such as autonomous underwater vehicles (AUVs) and ocean gliders enable turbulence measurements in a variety of patterns and detect structures that may be left undetected using vertical profiling alone (Yamazaki et al., 1990; Frajka-Williams et al., 2022).

1 Introduction

Turbulence measurements in the ocean are needed to quantify the turbulent fluxes of heat, salt and momentum, and they are important for understanding the processes affect-

Obtaining high-quality turbulence measurements from robotic platforms can be challenging. The vehicle motion, both forward motion and maneuvering, must be resolved and its effect on the measured signal must be filtered out. Pioneering work in the 1990s used turbulence measurement packages and three orthogonal accelerometers mounted on AUVs, such as described by Levine and Lueck (1999) and Dhanak and Holappa (1999). Vehicle vibrations were found to completely obscure oceanic signals at distinct frequencies. Using coherency analysis between the shear probe record and the acceleration measured by the accelerometer aligned with the shear probe, noise could be removed in the time and frequency domain (Levine and Lueck, 1999). Goodman et al. (2006) improved this technique and developed a multivariate correction approach to remove vibration-induced components from shear spectra using the accelerometer signal measured in multiple directions. This latter way of minimizing the effects of body motion and probe vibrations on the turbulence measurements is commonly known as the “Goodman method” and paved the way for a range of robotic platforms with microstructure sensors.

Modern microstructure measurements using shear probes attached to robotic platforms include those from gliders (Fer et al., 2014; Palmer et al., 2015; Schultze et al., 2017; Scheifele et al., 2018) and from AUVs such as REMUS (Goodman et al., 2006) and the Autosub Long Range AUV (Thorpe et al., 2003; McPhail et al., 2019; Garabato et al., 2019; Spingys et al., 2021). Gliders are buoyancy-driven and, in contrast to AUVs, do not use a thruster for forward motion (some new-generation gliders can be equipped with a thruster for rapid maneuvering when needed). The smooth motion of the gliders with negligible vehicle vibration and signal contamination makes them excellent platforms for shear probe measurements (Fer et al., 2014). While offering extended endurance of 1 to 3 months, gliders move relatively slowly ($0.1\text{--}0.3\text{ m s}^{-1}$ through water) and typically profile in a saw-tooth pattern. AUVs move faster (order 1 m s^{-1} through water) and are more maneuverable but typically have shorter endurance (order of hours to days). A major concern regarding the quality of turbulence measurements from an AUV is the vibrations caused by the propulsion system.

In this study, we mounted a self-contained turbulence instrument package on a light AUV and collected measurements in the Barents Sea in a frontal region where waters of Atlantic and Arctic origin meet (Fig. 1).

The light AUV is lighter than REMUS and the Autosub Long Range AUV. With a typical configuration of sensors, it weighs about 35 kg in air, can be handled by one person, and enables easy deployment and recovery. In addition, the light AUV is considerably more affordable compared to other AUVs, and it offers open-access software and ease of hardware configurations, making it a desirable and versatile product.

In this technical note we describe the instrument setup, the data collected (Sect. 2) and the processing methods (Sect. 3),

and we present the data quality and the capability of the light AUV for dissipation rate measurements (Sect. 4). In our notation, data processing and format of the data, we follow the recommendations and conventions of the SCOR Working Group on analyzing ocean turbulence observations to quantify mixing (ATOMIX, <http://wiki.uib.no/atomix>, last access: 22 March 2022). Data are available from Fer et al. (2021).

2 Instruments, cruise and data

The data were collected during a Nansen Legacy cruise (9 February–1 March 2021) on board the research icebreaker *Kronprins Haakon* in the Barents Sea (Nilsen et al., 2021). Turbulence measurements using the light AUV (“Harald”, hereafter referred to as AUV) were made on the morning of 26 February 2021 near the Polar Front between Atlantic water and Polar water. The AUV was deployed at 07:30 UTC at $76^{\circ}24.94'\text{ N}$, $34^{\circ}9.61'\text{ E}$ and recovered at 12:15 UTC at $76^{\circ}26.11'\text{ N}$, $34^{\circ}11.21'\text{ E}$ after completing three crossings of the front. Before and during the AUV mission, the wind speed was around 10 m s^{-1} , air temperatures were close to -5° C measured at 15 m height and the surface boundary layer extended to about 60 m depth. The turbulence package on the AUV continuously measured ocean microstructure. Additional data used include near-surface temperature and salinity measured by a Sea-Bird Electronics thermosalinograph with water intake at 4 m depth, as well as two reference dissipation profiles measured by a vertical microstructure profiler (MSS-90L) from Sea and Sun Technology. The temperature and conductivity measured by the thermosalinograph are accurate to $\pm 0.001^{\circ}\text{ C}$ and $\pm 0.001\text{ S m}^{-1}$. The noise level of the dissipation measurements from the MSS-90L is $(1\text{--}3) \times 10^{-9}\text{ W kg}^{-1}$. The ship track, AUV track and MSS positions are shown in Fig. 1b.

2.1 Light autonomous underwater vehicle

The light AUV was developed at the Underwater Systems and Technology Laboratory at the University of Porto (Sousa et al., 2012). It is commercially produced by OceanScan Marine Systems and Technology Lda. Our AUV (sketch shown in Fig. 2) is an extended version compared to the standard light AUV.

It is 100 m pressure-rated and equipped with a pumped conductivity–temperature–depth sensor (CTD; SBE-49 Fast-CAT), a Nortek Doppler velocity log (DVL1000), an attitude sensor (Lord Microstrain 3DM-GX4-25), an acoustic modem, a fluorescence sensor and a dissolved oxygen optode. The accuracies of the measurements from the AUV are $\pm 0.002^{\circ}\text{ C}$ for temperature, $\pm 0.0003\text{ S m}^{-1}$ for conductivity, 0.3 % rms (root mean square) of the measured value for horizontal flow speed past the instrument (measured by DVL1000), $\pm 8.5^{\circ}$ for yaw at the observation latitude, and $\pm 2.0^{\circ}$ for pitch and roll. As the depth was about 250 m,

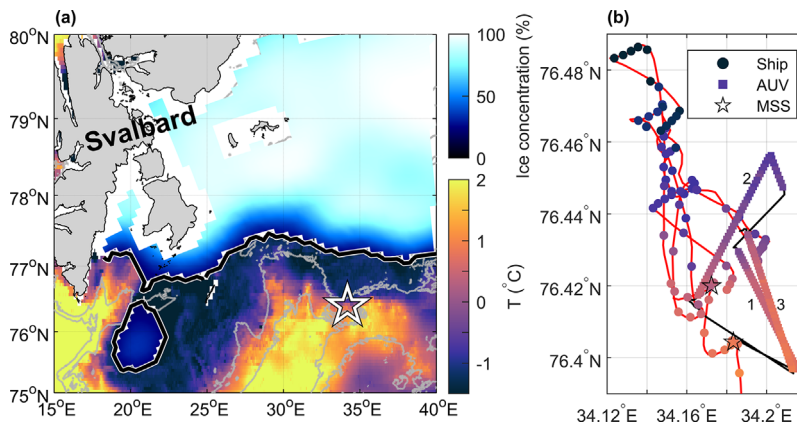


Figure 1. (a) Overview map of the study region in the Barents Sea. Ice concentration and ice edge (thick black contour) on 26 February 2021 are from OSI SAF (OSI SAF, 2017). Sea surface temperature is from the EU Copernicus Marine Service product SEAICE_ARC_SEAICE_L4_NRT_OBSERVATIONS_011_008 at 0.05° resolution based upon observations from the Metop-A AVHRR instrument. The experiment location marked by a star near 34° E is expanded in (b). (b) The ship's track (red) with near-surface temperature from the ship's thermosalinograph and the AUV track (black) with the AUV's temperature measurements along the three transects are color-coded (temperature color scale is the same as in a). Stations where a vertical microstructure profile (MSS) was collected are also shown.

the DVL1000 did not track bottom during this mission. The AUV trajectory was only constrained by inertial navigation, with an expected drift of about 15 % of the distance traveled. The AUV is controlled by the onboard software DUNE Unified Navigation Environment and is configurable in both hardware and software. The expected mission duration is between a few hours and 48 h, largely depending on the operating speed. While maximum speed can exceed 2 m s^{-1} , a normal operating speed (without the turbulence package) is about 1.5 m s^{-1} . The AUV communicates via satellite (iridium), WiFi and acoustics. It can be remotely controlled within the WiFi range of about 200 m, which can be useful during deployment and recovery. While deployment is easily done from a ship using a crane (see Fig. 3), recovery is best done from smaller work boats to avoid damaging the instrument. The turbulence package was mounted below the AUV using custom-made brackets and connected to the AUV using a bulkhead connector and a custom-made cable. Due to the extra drag caused by the turbulence package, the operating speed during our mission was about 1.1 m s^{-1} . Before deployment, we programmed the AUV to follow the frontal zone by tracking the maximum temperature gradient at different depths, which it successfully did.

2.2 Turbulence package

Turbulence measurements were made using a MicroRider-1000LP (MR) from Rockland Scientific, Canada. The MR was modified to the tidal energy (TE) configuration, which was used earlier in high-flow tidal energy channels. The

TE configuration includes increasing the sampling rate to 1024 Hz for fast channels (from the typical 512 Hz), replacing the ASTP circuit board components with an anti-aliasing filter of 196 Hz (from the typical 98 Hz), and reducing the gain of the shear channel by a factor of 10 from about 1 to 0.1 s. This modification allows reaching wavenumbers high enough to resolve the shear spectrum (reaching 130 cpm at 1.5 m s^{-1} and with 196 Hz anti-aliasing filter). Reduction in the gain is to compensate for the larger signals produced by faster sensor speed through the water (the shear sensor signal increases in proportion to speed squared).

The MR was attached beneath the AUV as seen in Figs. 2 and 3. It was powered by a stand-alone 4S1P (14.8 V) lithium-ion battery integrated into the vehicle and controlled by a relay connected to the main power board inside the AUV. This was done to provide a relatively clean power source. Earlier tests in a Norwegian fjord when the MR was fully integrated into the AUV power source showed significant electronic noise in the microstructure measurements. Data were stored internally on a compact flash memory card. The vertical axis-to-axis separation between the AUV and the MR was approximately 30 cm. The flow field around AUVs with a similar shape and cross-section as the AUV we used has been modeled (Mostafapour et al., 2018). Although this computational fluid dynamics modeling does not fully represent our AUV with the turbulence package attached, it indicates the flow deformation around the AUV hull. All turbulence sensors protruded about 25 cm from the nose of the AUV and are expected to sample flow with negligible deformation.

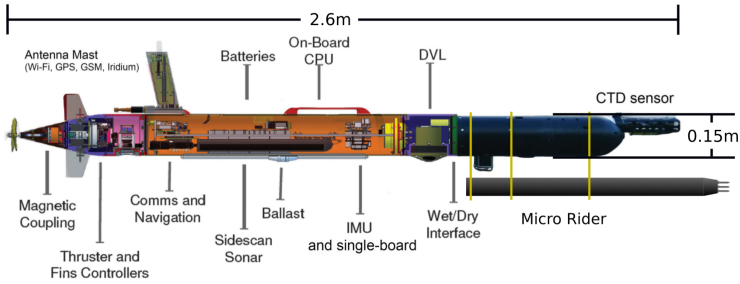


Figure 2. Sketch showing the AUV used on this mission, with instruments and hardware as indicated. This sketch is a modified version of a figure in Fossum et al. (2021).

and pressure. The accuracy of the measurements is 0.1 % for the pressure, 2 % for the piezo-accelerometers and 5 % for the shear probes. Because of an error in the setup configuration file, the thermistor did not record measurements. Roll, pitch and yaw are clockwise rotations around the x , y and z axis of the AUV or the MR, following the right-hand rule. However, the instrument axis coordinate systems differ: for the MR x points outward from the nose along the instrument’s axis, y is to the left (positive toward port) and z is positive upward. For the AUV, the vehicle x – y – z frame is aligned with [north, east, down]; x is positive in the nominal vehicle direction of motion (forward), y is to the right (starboard) and z is positive in the down direction.

3 Processing

Before converting the raw data from the shear probes into physical units, the MR time stamp was corrected against the AUV time stamp. When the shear probe travels through the water horizontally along axis x at speed U , the voltage E_p produced by the probe in response to a cross-axis velocity v is given by

$$E_p = 2\sqrt{2}\hat{s}Uv, \tag{1}$$

where the constant \hat{s} is the sensitivity of the probe, which must be determined by calibration (Lueck et al., 2002). The probe voltage is then converted to shear, $\partial v/\partial x$, in physical units as

$$\frac{\partial v}{\partial x} = \frac{1}{U} \frac{\partial v}{\partial t} = \frac{1}{2\sqrt{2}\hat{s}U^2} \frac{dE_p}{dt} \tag{2}$$

by using the known sensitivity of the shear probe and the travel speed of the AUV (Lueck et al., 2002). The time derivative of E_p is obtained from the differentiator in the electronics of the shear probe with a known gain. A second probe oriented orthogonal to the first one similarly measures $\partial w/\partial x$. An initial high-pass filtering at 0.6 Hz of the shear and vibration signals was performed in order to exclude signals at scales larger than the AUV (about 2 m). Spectral loss

Figure 3. Deployment of MicroRider-1000LP mounted below the light AUV “Harald” in the Barents Sea at 07:30 on 26 February 2021. From left: co-author Tore Mo-Bjørkelund and crew member Svein Are Simonsen. Photographer: Frank Nilsen, University Centre in Svalbard.

The MR was equipped with two airfoil velocity shear probes (SPM-38), one fast-response thermistor (FP07), a pressure transducer, a two-axis vibration sensor (a pair of piezo-accelerometers) and a high-accuracy dual-axis inclinometer. The MR samples the signal plus signal derivatives on the thermistor and pressure transducer, as well as the derivative for shear signals, allowing high-resolution measurements. The sampling rate is 1024 Hz for the vibration, shear and temperature sensors, and it is 128 Hz for pitch, roll

due to high-pass filtering was corrected for. In addition, both shear and vibration signals were despiked before calculating shear spectrum. Despiking was done by comparing the absolute shear and vibration time series to their 0.5 Hz low-passed records. When the ratio between the absolute and the low-passed time series exceeded 9 (8) for the shear (vibration), ± 0.04 s centered at the spike were replaced by the value averaged over ± 0.5 s before and after the spike.

Shear spectra are used to estimate the dissipation rate of turbulent kinetic energy, ϵ . The dissipation rate is proportional to the variance of shear contained at scales from $\mathcal{O}(1)$ to $\mathcal{O}(10^{-2})$ m. The time series from each shear probe was segmented into half-overlapping 8 s long portions, corresponding to roughly 10 m portions along the transects. A fast Fourier transformation (FFT) length corresponding to 1 s was chosen, and each half-overlapping 1 s segment was detrended and smoothed using a Hanning window before averaging them to get the shear frequency spectrum for each 8 s segment. Spectral loss due to the size of the shear probe was corrected for.

Shear spectra were converted from frequency, f , domain to wavenumber, k , domain using Taylor's frozen turbulence hypothesis and the AUV speed, U , as $k = f/U$. The Doppler velocity log (DVL) on the AUV measured U , and the average value for each 8 s segment was used in the conversion. Typical U was 1.1 m s^{-1} , and thus the FFT length is equivalent to 1.1 m along-path length and resolves the low wavenumber part of the spectrum while excluding scales greater than or equal to the vehicle length. For additional cleaning of the shear data, the shear spectrum signal coherent with the accelerometer spectrum signal was removed using the method described by Goodman et al. (2006).

Assuming isotropic turbulence, ϵ was calculated for each segment by integrating the cleaned wavenumber spectrum, $\Psi(k)$, as

$$\epsilon = \frac{15}{2} \nu \overline{\left(\frac{\partial v}{\partial x}\right)^2} = \frac{15}{2} \nu \int_0^{\infty} \Psi(k) dk \approx \frac{15}{2} \nu \int_{k_1}^{k_u} \Psi(k) dk, \quad (3)$$

where ν is the kinematic viscosity and the overbar denotes averaging in time (e.g., Fer et al., 2014). The lower (k_1) integration limit is determined by the wavenumber corresponding to the FFT length, and the upper ($k_u < \infty$) integration limit is usually determined from a minimum in a low-order polynomial fit to the wavenumber spectrum in log–log space. Typically electronic noise takes over after the minimum in the spectrum. To account for the variance in the unresolved part of the spectrum (integration outside the k_1 and k_u limits), the empirical model for the turbulence spectrum determined by Nasmyth (1970) was used, and hence the estimated ϵ is close to the full integration. When using two shear probes, the dissipation rate in the segment is calculated as the average of the values from both sensors. In our data, the two sensors always agreed within a factor of 4.

From dissipation estimate time series, we extracted sections when the AUV performed horizontal transects at approximately constant depth with the propeller set to 1500 rotations per minute (RPM). During the horizontal transects the angle of attack (AOA), which is the difference between the pitch and the direction of travel, was much smaller ($< 3^\circ$) than the critical value of $\pm 20^\circ$ for when the flow over the shear probe is no longer laminar (Osborn and Crawford, 1980). Final data screening excluded data with a rate of change exceeding 10, 5 and 2 units per 1 s for roll, pitch and RPM, respectively. The thresholds in the final screening were determined from visual inspection of the rate of change versus dissipation estimates.

4 Results

Five transects at depths 10, 20, 30, 40 and 50 m were planned across the temperature front; however, the mission ended abruptly after three transects due to a leak in the main hull of the AUV. The leakage was through the antenna and is a rare problem ($< 1\%$ of missions ended due to leakages). Data recovered from the three transects are sufficient for the purpose of this technical note. Flight kinematics measured by the AUV are shown in Fig. 4. Pitch was in general less than 2.5° , and roll was less than 7.5° . The relatively large average roll is probably a result of the positioning of the MR relative to the AUV, and the rolling moment induced by the propeller. The peak roll early in transect 2 is when the AUV made an abrupt turn (see Fig. 1b). Note that when the rate of change of roll, pitch and RPM was large, the dissipation rate data were excluded (Sect. 3). The propeller rate was set constant at 1500 RPM, yet the speed past the instrument varied between 1 and 1.2 m s^{-1} , seemingly related to the transition between the water masses (Fig. 4b and c).

Figure 5a and b show mean shear spectra in frequency space using 8 s long records (length used for single dissipation estimates) for a moderate and a high value of ϵ , respectively. Corresponding vibration spectra from the accelerometers are also shown.

The 95 % confidence interval around a mean spectrum can be calculated as the factor $\exp(\pm 1.96 \times \frac{5}{4} (N_f - N_v)^{-\frac{1}{2}})$, where N_f is the number of fft segments and N_v is the number of vibration signals (Lueck, 2022). Using $N_f = 15$ and $N_v = 2$, we obtain [0.72, 1.40]. The 95 % interval carried over to our epsilon estimates, including an additional 10 % sensor sensitivity calibration uncertainty, becomes about [0.6, 1.6].

An RPM of 1500 corresponds to 25 Hz, or using a mean speed of 1.1 m s^{-1} to 23 cycles per meter (cpm). The contamination of the shear spectra by the propulsion system is visible in Fig. 5; the propulsion system is not perfectly balanced around its rotational axis, and vibrations at 25, 50 and 75 Hz (and the harmonics of these frequencies) are induced by this off-center rotation. The main contaminating energy is at 75 Hz, related to the three-bladed propeller. In addition, the

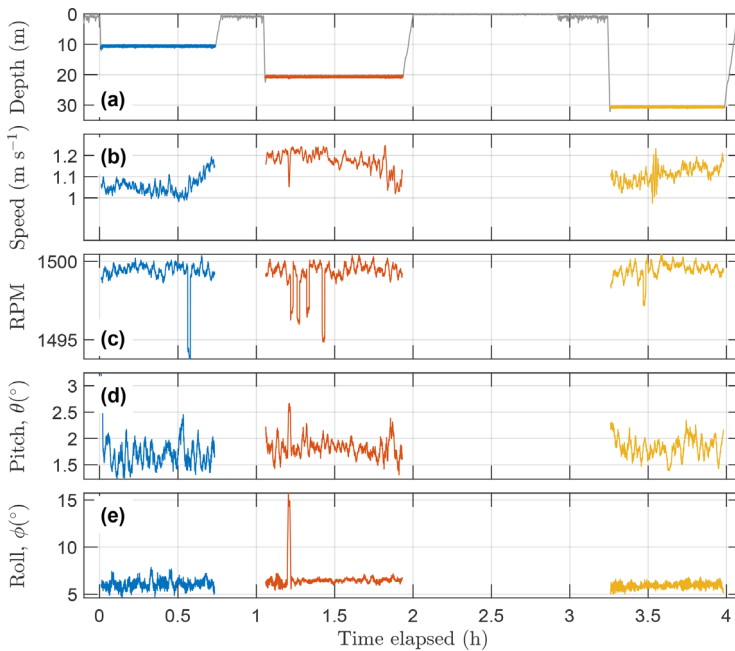


Figure 4. Flight kinematics from the AUV. Time series of (a) depth, (b) speed past the instrument, (c) rotation per minute (RPM), (d) pitch and (e) roll. Time elapsed is from 26 February at 08:06 UTC. Selected transects at approximately 10, 20 and 30 m are shown.

accelerometers indicate that vibrations between 15 and 22 Hz also affect the shear signal; however, the source of these vibrations is not clear and is discussed further in Sect. 5. The cleaned frequency spectra show that contamination from instrument vibration has been successfully removed and that the spectra resemble the empirical Nasmyth spectra (Nasmyth, 1970). Note, however, that the cleaned spectra also show a reduction in the spectral levels at low frequencies at which the vibration signal is relatively low. The reduction in spectral levels and potential biases associated with the Goodman method are discussed in Sect. 5. The shear spectra in the wavenumber domain, for the same values of ε as in (a) and (b), are shown in Fig. 5c and d. In general, shear probe 1, $\partial w/\partial x$, resolves somewhat higher wavenumbers than shear probe 2, $\partial v/\partial x$. For moderate ε , shear probes 1 and 2 resolve wavenumbers up to 40 and 30 cpm, respectively, while for high ε they resolve wavenumbers up to 85 and 65 cpm, respectively. Beyond the resolved part of the spectrum, noise levels become too large, and the shear spectrum deviates significantly from the empirical Nasmyth spectrum.

Further quality control of our data is done by bin-averaging ε over different ranges. Figure 6a and b show bin-averaged clean spectra in wavenumber domain for $\partial w/\partial x$ and $\partial v/\partial x$, respectively. Values limiting the bins are listed in the caption.

For $\varepsilon > 10^{-7} \text{ W kg}^{-1}$ the spectra closely resemble the bin-averaged Nasmyth spectra. However, the roll-off in the dissipation subrange starts earlier than that indicated in the Nasmyth spectra, suggesting that the most energetic dissipation rates are not fully resolved. For comparison, we also include the bin-averaged theoretical Panchev–Kesich spectrum (Panchev and Kesich, 1969) and observe that the roll-off of the Panchev–Kesich spectrum fits our cleaned spectrum better than the Nasmyth spectrum. Comparing $\partial w/\partial x$ to $\partial v/\partial x$, we observe that $\partial w/\partial x$ is generally capable of resolving wavenumbers 10–20 cpm higher than $\partial v/\partial x$. For $\varepsilon < 10^{-7} \text{ W kg}^{-1}$ the bin-averaged spectra start deviating from the empirical Nasmyth and theoretical Panchev–Kesich spectra significantly for wavenumbers below 4 cpm, especially for $\partial v/\partial x$. While the difference in data quality delivered by the two probes is less than ideal, it is expected that the shear probes oriented orthogonally will sense the vehicle motion differently. Comparison with spectral shapes, vehicle motion and noise sources is discussed further in Sect. 5.

The systematic difference in data quality seen in the low dissipation range in Fig. 6 may manifest itself in the dissipation estimates. Figure 7 compares ε_1 and ε_2 calculated from the two different probes.

The scatter plot (Fig. 7a) shows that the two probes agree well within a factor of two. In fact, 97 % of the dissipation

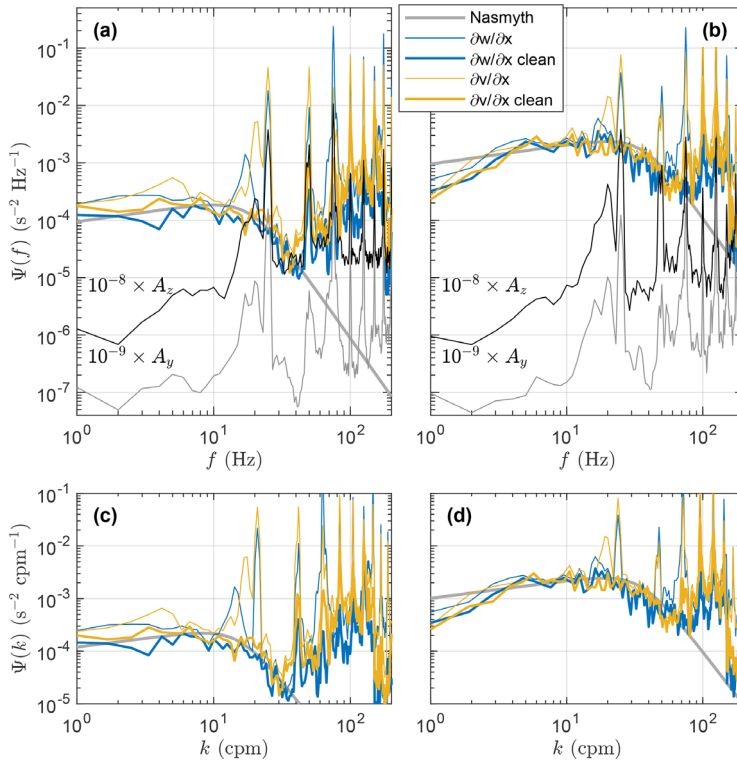


Figure 5. Example frequency spectra with (a) moderate ($\varepsilon = 5.7 \times 10^{-8} \text{ W kg}^{-1}$) and (b) high ($\varepsilon = 1.4 \times 10^{-6} \text{ W kg}^{-1}$) dissipation rates using 8 s long records. Vibration spectra along the instrument’s main and transverse axes are also shown with an offset as indicated. Cleaned spectra as indicated by the legend show frequency spectra after removing the shear probe signal coherent with the accelerometer signal. Empirical Nasmyth spectra are shown for the values of ε . Panels (c) and (d) show the same shear spectra as (a) and (b), respectively, but in the wavenumber domain. $\partial w/\partial x$ and $\partial v/\partial x$ are shear probes 1 and 2, respectively, on the MicroRider.

estimates from the two probes agree within a factor of 2. Yet, while the disagreement between the two probes is more or less random for $\varepsilon > 5 \times 10^{-8} \text{ W kg}^{-1}$, there is a systematic offset for $\varepsilon < 5 \times 10^{-8} \text{ W kg}^{-1}$, with ε_2 showing higher dissipation rates than ε_1 . The probability distribution function (PDF) for ε_1 and ε_2 (Fig. 7b) shows that the two probes in general agree very well for $\varepsilon > 10^{-7} \text{ W kg}^{-1}$. For comparison of the three transects of the AUV, we show PDFs of ε_1 and ε_2 at 11, 21 and 31 m depth (Fig. 7c, d and e, respectively). While the PDFs at 11 and 21 m depth resemble lognormal or skewed lognormal distributions, for which ε_1 and ε_2 typically agree (Fig. 7c, d), the PDF at 31 m depth differs. At this deeper transect, a larger portion of the ε measurements is below $10^{-7} \text{ W kg}^{-1}$. A second mode appears in low dissipation rates, particularly for ε_2 , suggesting that noise contributes significantly to the measurements at 31 m depth.

For additional quality control, we compare the final estimates of ε to dissipation measurements from a vertical microstructure profiler (MSS-90 from Sea and Sun Technology) collected near the AUV transects during the AUV mission (see Fig. 1b). The temperature sampled along the three transects at 11, 21, and 31 m depth, as well as the corresponding dissipation rates, are shown in Fig. 8a and b, respectively.

The dissipation rate of turbulent kinetic energy (TKE) varies throughout the different transects but generally becomes smaller at greater depth, which is expected in the boundary layer. The arithmetic mean (including 95 % confidence intervals) of the natural logarithm of the dissipation rates along the horizontal transects is compared to vertical microstructure profiles (Fig. 8c). Although the spatial variability of ε is known to be large (Yamazaki et al., 1990), the vertical profiles and the horizontal transects show comparable dissipation rates. Note, however, that the comparison between the two MSS profiles and the average dissipation rates

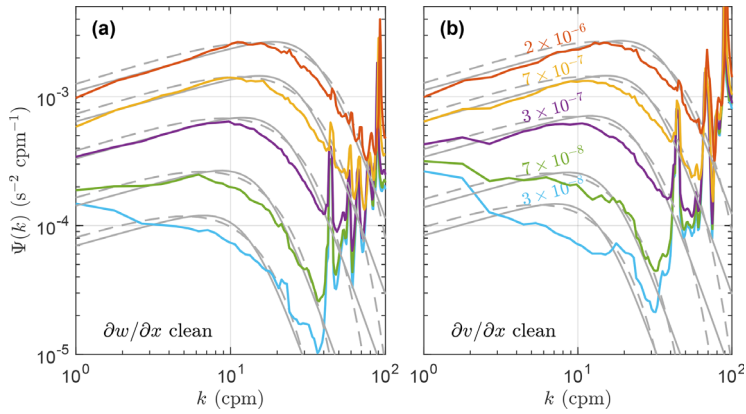


Figure 6. Wavenumber shear spectra of (a) cleaned $\partial w/\partial x$ (shear probe 1) and (b) cleaned $\partial v/\partial x$ (shear probe 2) averaged in increasing bins of dissipation rate estimates using data from all depths. Bin averaging limits are set to 1×10^{-8} , 5×10^{-8} , 1×10^{-7} , 5×10^{-7} , 1×10^{-6} and 5×10^{-6} , averaging over 210, 145, 827, 466 and 382 ($\partial w/\partial x$) as well as 186, 146, 748, 529 and 415 ($\partial v/\partial x$) spectra. Bin-averaged values of ε (units: W kg^{-1}) are only shown in (b) as they were similar for both probes. Background curves are the bin-averaged (solid) Nasmyth and (dashed) Panchev–Kesich spectra averaged over all individual estimates in the corresponding dissipation bins.

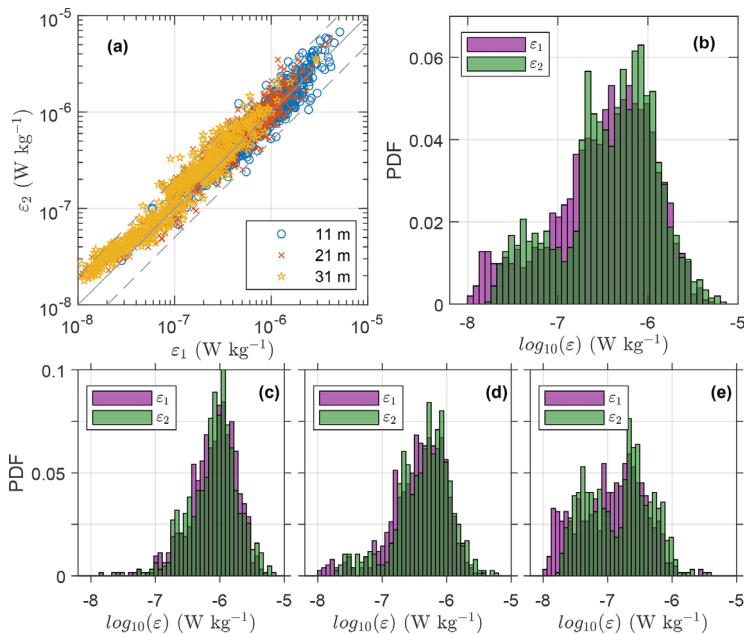


Figure 7. Comparison of dissipation estimates from two probes. ε_1 is from $\partial w/\partial x$ measurements, and ε_2 is from $\partial v/\partial x$. (a) Scatter plot of dissipation estimates from each probe, color-coded with respect to measurement depth. Gray dashed lines span the agreement within a factor of 2. (b) Probability distribution function (PDF) for dissipation rates from each probe using data from all depths. (c, d, e) PDFs for dissipation rates from each probe using data from transects at 11, 21 and 31 m depths, respectively.

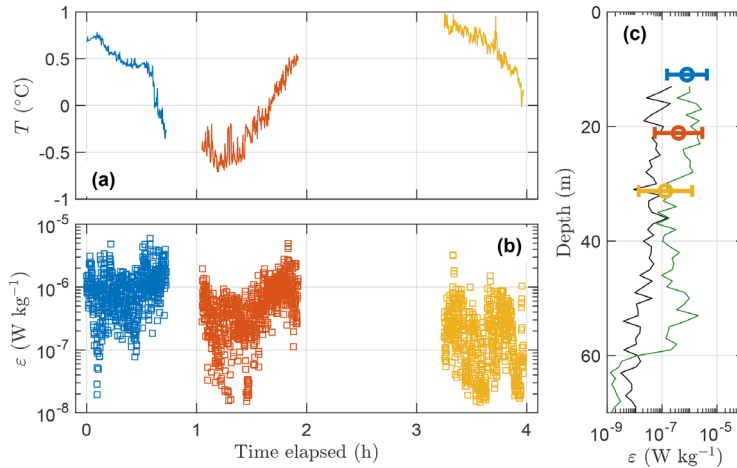


Figure 8. Overview of dissipation rates. Time series of (a) temperature and (b) final estimate of the dissipation rate. (c) Vertical profiles (black and green) of ε measured by the vertical microstructure profiler at two co-located stations marked by stars in Fig. 1b. Mean value and the lower and upper limits (95 % confidence intervals) of the natural logarithm of the AUV–MR measurement are shown at their corresponding average depth in (c). Blue, red and yellow correspond to 11, 21 and 31 m depth, respectively.

must be interpreted with caution. The two MSS profiles differ by 1 order of magnitude, enveloping the AUV-based measurements, and cannot be used to statistically test the validity of the AUV measurements.

5 Discussion

While microstructure measurements from gliders and larger AUVs have been extensively tested, microstructure measurements from smaller AUVs have not. Although the light AUV is both more affordable and easier to handle than its larger siblings, it has potential drawbacks. Being smaller, the AUV is more susceptible to body motion and vibration, potentially contaminating the microstructure measurements. In addition, when the AUV platform is only a few times larger than the MR, AUV maneuvering skills may suffer from the added drag from the MR, depending on how the MR is integrated.

From Fig. 5, we see that the shear spectra are significantly contaminated in the 10–30 Hz band (9–27 cpm) and in narrow bands centered at the integers of 25 Hz. The narrowband peaks at 25, 50 and 75 Hz (and their higher harmonics) come from the three-bladed propeller operating at 1500 RPM. While vibrations from the propulsion system are less than ideal for turbulence measurements, the contamination occurs in a narrow band and is easily detected by both the accelerometers. The vibrations detected between 10 and 22 Hz (9–20 cpm) are more worrisome as this contamination covers a broader band of the turbulence spectrum in the wavenumbers at which the spectrum typically rolls off. The spectral peaks in the shear spectra are at different frequencies

for $\partial w/\partial x$ and $\partial v/\partial x$, suggesting that the vehicle motion (pitch, roll, yaw) is the main source of this contamination. While $\partial v/\partial x$ will be affected by the roll and yaw fluctuations, $\partial w/\partial x$ will be affected by changes in pitch but should be fairly insensitive to changes in roll and yaw.

The method for noise removal relies on the squared coherency between the shear probe signal and the accelerometer signals (Goodman et al., 2006). Removal of the shear probe signal coherent with the accelerometer signal produces clean spectra (Fig. 5). The clean spectra show that the spikes in the 10–30 Hz band have been successfully removed. Note, however, that squared coherency will always be nonzero even when the shear probe and accelerometer time series are completely incoherent. This results in a bias by removing some of the incoherent signal. We did not correct this bias in our study. When we apply a simple correction recommended in the ATOMIX guidelines, the clean spectra increase by a factor of about 1.2. This potential bias does not affect our conclusions.

The bin-averaged shear spectra suggest that the most energetic wavenumbers are not fully resolved by our instrumentation; i.e., the transition between the inertial subrange and the dissipation subrange rolls off at lower wavenumbers compared to the similarly bin-averaged Nasmyth and Panchev–Kesich spectra (Fig. 6). While the shape of the spectral roll-off is relatively similar to that in the Panchev–Kesich spectrum, the offset between the observed and the theoretical spectra is significant. The bias unaccounted for in application of the Goodman method cannot explain this offset fully. Some of the discrepancies in the roll-off are likely

caused by averaging the spectra over variable dissipation rates, whereby the spectral peak shifts to higher wavenumbers with increasing ε , which will smooth the spectral roll-off. Yet, to mimic the effect of smoothing of the spectral roll-off, we bin-average individual Nasmyth and Panchev–Kesich spectra similarly. Another possible reason for the difference between the observed and the Nasmyth spectra is that an unknown fraction of the removed shear probe signal coherent with the accelerometers can be natural turbulence indistinguishable from the vibrations caused by the AUV (Palmer et al., 2015). This likely leads to a reduction of variance in the contaminated band between 10 and 30 Hz (9–27 cpm).

The average shear spectra for the smaller dissipation rates (Fig. 6) deviate from the Nasmyth shape for small wavenumbers. Combined with the issues resolving the spectral roll-off, this suggests that the instrument is not able to resolve dissipation rates smaller than about $5 \times 10^{-8} \text{ W kg}^{-1}$. This is particularly problematic for $\partial v / \partial x$ (ε_2). For $\varepsilon < 5 \times 10^{-8} \text{ W kg}^{-1}$, there is a systematic offset between the two shear probes in the low wavenumber part of the spectrum (< 3 cpm). In weakly turbulent regimes, the assumption of local isotropy may be violated, and the dissipation estimates from the orthogonal probes deviate when the buoyancy Reynolds number ($\frac{\varepsilon}{\nu N^2}$) is about 200 or less (Yamazaki and Osborn, 1990). Here, the AUV mission is conducted within the weakly stratified upper surface layer with large buoyancy Reynolds numbers ($> 10^4$, not shown), and we do not expect differences caused by vertical stratification or anisotropy at probe separation scales. As with the noise contamination in the 10–22 Hz band, the difference between the two probes is likely because the two probes sense the changes in pitch, roll and yaw differently. Furthermore, the effect of pitch, yaw and roll on the shear sensors is also dependent on how the MR is mounted on the AUV.

When mounting the MR on the AUV, our main concern was to ensure that the shear sensors protruded outside the region of flow deformation, without modifying the AUV itself. To avoid interfering with the acoustic modem and fluorescence sensor on the upper part of the AUV, we mounted the MR below the AUV using brackets. This solution led to unwanted pitching at higher velocities due to the change in the center of drag. An alternative solution would be to redesign the wet section (nose) of the AUV to fit the MR. This would likely lead to better AUV maneuverability, reducing changes in pitch, roll and yaw, hence reducing the vehicle motion sensed by the MR.

The MR was modified to the tidal energy (TE) configuration (Sect. 2.2) to allow for sufficiently resolved measurements at high operation speeds of the AUV. The AUV used in this paper has the capability to move at speeds exceeding 2 m s^{-1} . The practical application in this study limited the maximum operating speeds to about 1.5 m s^{-1} because of the drag added by the MR. To further limit vibrations, we kept the operation speed at $1\text{--}1.2 \text{ m s}^{-1}$. For such operating speeds, the standard MR configuration could work satisfac-

torily. However, with a better integrated MR, for instance inside the wet-nose section of the AUV, higher speeds would be achievable with reduced drag, necessitating the use of the TE configuration.

6 Summary and conclusions

A modified MicroRider-1000LP was mounted below a light AUV and tested in the Barents Sea during a cruise in February 2021. The AUV conducted three transects across a surface temperature front at 11, 21 and 31 m depth, while continuously sampling microstructure shear. The dissipation rate of turbulent kinetic energy is estimated from the shear measurements. Although the vibrations of the AUV contaminate the shear probe records, the shear spectra for dissipation levels above $5 \times 10^{-8} \text{ W kg}^{-1}$ are sufficiently cleaned using the Goodman method (Goodman et al., 2006). Dissipation rates measured from the AUV agree well with the measurements using a loosely tethered vertical microstructure profiler from the ship. However, the overall noise level from the AUV is quite large; this setup cannot detect dissipation rates below $5 \times 10^{-8} \text{ W kg}^{-1}$ reliably and is unfit for use in quiescent boundary layers. An improved installation of the turbulence probes on the nose of the AUV could reduce some of the limitations reported here and allow acceptable quality dissipation measurements from the AUV in relatively quiet environments.

Data availability. The AUV and MicroRider data set is available from Fer et al. (2021) through the Norwegian Marine Data Centre (<https://doi.org/10.21335/NMDC-1821443450>) with a Creative Commons Attribution 4.0 International License. SST data are obtained from the E.U. Copernicus Marine Service Information; <https://doi.org/10.48670/moi-00130> (E.U. Copernicus Marine Service Information, 2020).

Author contributions. IF, TMB and EHK collected the data in addition to conceiving and planning the analysis. IF and EHK performed the analysis. EHK wrote the paper, with advice and critical feedback from IF and TMB. All authors discussed the results and finalized the paper.

Competing interests. At least one of the (co-)authors is a member of the editorial board of *Ocean Science*. The peer-review process was guided by an independent editor, and the authors also have no other competing interests to declare.

Disclaimer. Publisher's note: Copernicus Publications remains neutral with regard to jurisdictional claims in published maps and institutional affiliations.

Acknowledgements. We thank the officers and crew of the *Kronprins Haakon* for their skillful operations and the cruise leader Frank Nilsen for supporting the experiment. Martin Ludvigsen facilitated the AUV and provided valuable advice in preparations and planning. We thank Rolf Lueck and Evan Cervelli at Rockland Scientific for their advice and assistance in modifying the MicroRider for the AUV application. The research is part of the Nansen Legacy project. The Nansen Legacy uses NIRD as a data depository (account numbers NS9610K and NS9530K). Figure 1a is produced using EU Copernicus Marine Service Information.

Financial support. The research was funded by the Research Council of Norway through the Nansen Legacy project (grant no. 276730).

Review statement. This paper was edited by Katsuro Katsumata and reviewed by Achim Randelhoff and one anonymous referee.

References

- Dhanak, M. R. and Holappa, K.: An Autonomous Ocean Turbulence Measurement Platform, *J. Atmos. Ocean. Tech.*, 16, 1506–1518, [https://doi.org/10.1175/1520-0426\(1999\)016<1506:AAOTMP>2.0.CO;2](https://doi.org/10.1175/1520-0426(1999)016<1506:AAOTMP>2.0.CO;2), 1999.
- E.U. Copernicus Marine Service Information: Arctic Ocean – Sea and Ice Surface Temperature, E.U. Copernicus Marine Service Information [data set], <https://doi.org/10.48670/MOI-00130>, 2020.
- Fer, I., Peterson, A. K., and Ulgren, J. E.: Microstructure Measurements from an Underwater Glider in the Turbulent Faroe Bank Channel Overflow, *J. Atmos. Ocean. Tech.*, 31, 1128–1150, <https://doi.org/10.1175/JTECH-D-13-00221.1>, 2014.
- Fer, I., Mo-Bjørkelund, T., and Kolås, E. H.: Dissipation measurements from AUV transects across a surface temperature front in the Barents Sea, NMDC [data set], <https://doi.org/10.21335/NMDC-1821443450>, 2021.
- Fossum, T. O., Norgren, P., Fer, I., Nilsen, F., Koenig, Z. C., and Ludvigsen, M.: Adaptive Sampling of Surface Fronts in the Arctic Using an Autonomous Underwater Vehicle, *IEEE J. Oceanic Eng.*, 46, 1155–1164, <https://doi.org/10.1109/JOE.2021.3070912>, 2021.
- Frajka-Williams, E., Brearley, J. A., Nash, J. D., and Whalen, C. B.: Chapter 14 – New technological frontiers in ocean mixing, in: *Ocean Mixing*, edited by: Meredith, M. and Garabato, A. N., 345–361, Elsevier, <https://doi.org/10.1016/B978-0-12-821512-8.00021-9>, 2022.
- Garabato, A. C. N., Frajka-Williams, E. E., Spingys, C. P., Legg, S., Polzin, K. L., Forryan, A., Abrahamson, E. P., Buckingham, C. E., Griffies, S. M., McPhail, S. D., Nicholls, K. W., Thomas, L. N., and Meredith, M. P.: Rapid mixing and exchange of deep-ocean waters in an abyssal boundary current, *P. Natl. Acad. Sci. USA*, 116, 13233–13238, <https://doi.org/10.1073/pnas.1904087116>, 2019.
- Goodman, L., Levine, E. R., and Lueck, R. G.: On Measuring the Terms of the Turbulent Kinetic Energy Budget from an AUV, *J. Atmos. Ocean. Tech.*, 23, 977–990, <https://doi.org/10.1175/JTECH1889.1>, 2006.
- Gregg, M. C.: *Ocean Mixing*, Cambridge University Press, <https://doi.org/10.1017/9781316795439>, 2021.
- Jakobsson, M., Mayer, L. A., Bringensparr, C., Castro, C. F., Mohammad, R., Johnson, P., Ketter, T., Accetella, D., Amblas, D., An, L., Arndt, J. E., Canals, M., Casamor, J. L., Chauché, N., Coakley, B., Danielson, S., Demarte, M., Dickson, M.-L., Dorschel, B., Dowdeswell, J. A., Dreutter, S., Fremand, A. C., Gallant, D., Hall, J. K., Hehemann, L., Hodnesdal, H., Hong, J., Ivaldi, R., Kane, E., Klaucke, I., Krawczyk, D. W., Kristoffersen, Y., Kuipers, B. R., Millan, R., Masetti, G., Morlighem, M., Noormets, R., Prescott, M. M., Rebesco, M., Rignot, E., Semiletov, I., Tate, A. J., Travaglini, P., Velicogna, I., Weatherall, P., Weinrebe, W., Willis, J. K., Wood, M., Zarayskaya, Y., Zhang, T., Zimmermann, M., and Zinglensen, K. B.: The International Bathymetric Chart of the Arctic Ocean Version 4.0, *Scientific Data*, 7, 176, <https://doi.org/10.1038/s41597-020-0520-9>, 2020.
- Levine, E. R. and Lueck, R. G.: Turbulence Measurement from an Autonomous Underwater Vehicle, *J. Atmos. Ocean. Tech.*, 16, 1533–1544, [https://doi.org/10.1175/1520-0426\(1999\)016<1533:TMFAAU>2.0.CO;2](https://doi.org/10.1175/1520-0426(1999)016<1533:TMFAAU>2.0.CO;2), 1999.
- Lueck, R. G.: Horizontal and vertical turbulence profilers, in: *Marine Turbulence: Theories, observations and models. Results of the CARTUM project*, edited by: Baumert, H. Z., Simpson, J. H., and Sündermann, J., 89–100, Cambridge University Press, Cambridge, UK, ISBN 978-05-2115-372-0, 2005.
- Lueck, R. G.: The statistics of turbulence measurements. Part 2: Shear spectra and a new spectral model, *J. Atmos. Ocean. Tech.*, in review, 2022.
- Lueck, R. G., Wolk, F., and Yamazaki, H.: Oceanic Velocity Microstructure Measurements in the 20th Century, *J. Oceanogr.*, 58, 153–174, <https://doi.org/10.1023/A:1015837020019>, 2002.
- McPhail, S., Templeton, R., Pebody, M., Roper, D., and Morrison, R.: Autosub Long Range AUV Missions Under the Filchner and Ronne Ice Shelves in the Weddell Sea, Antarctica – an Engineering Perspective, in: *OCEANS 2019 – Marseille*, 1–8, IEEE, <https://doi.org/10.1109/OCEANSE.2019.8867206>, 2019.
- Mostafapour, K., Nouri, N. M., and Zeinali, M.: The Effects of the Reynolds Number on the Hydrodynamics Characteristics of an AUV, *J. Appl. Fluid Mech.*, 11, 343–352, <https://doi.org/10.29252/jafm.11.02.28302>, 2018.
- Nasmyth, P. W.: *Oceanic turbulence*, PhD thesis, University of British Columbia, <https://doi.org/10.14288/1.0302459>, 1970.
- Nilsen, F., Fer, I., Baumann, T. M., Breivik, Ø., Czyz, C., Frank, L., Kalhagen, K., Koenig, Z., Kolås, E. H., Kral, S. T., Mabrouk, B. M. A., Mo-Bjørkelund, T., Muller, M., and Rabault, J.: Nansen Legacy Cruise PC-2: Winter Process Cruise, Nansen Legacy Report Series, University of Tromsø – The Arctic University of Norway, <https://doi.org/10.7557/nlr.6324>, 2021.
- Osborn, T. R. and Crawford, W. R.: An airfoil probe for measuring turbulent velocity fluctuations in water, in: *Air–Sea Interaction: Instruments and Methods*, edited by: Dobson, F., Hasse, L., and Davis, R., 369–386, Plenum Press, New York, ISBN 978-14-6159-182-5, 1980.
- OSI SAF: Global Sea Ice Concentration (netCDF) – DMSP, EUMETSAT [data set], https://doi.org/10.15770/EUM_SAF_OSI_NRT_2004, 2017.

- Palmer, M., Stephenson, G., Inall, M., Balfour, C., Düsterhus, A., and Green, J.: Turbulence and mixing by internal waves in the Celtic Sea determined from ocean glider microstructure measurements, *J. Marine Syst.*, 144, 57–69, <https://doi.org/10.1016/j.jmarsys.2014.11.005>, 2015.
- Panchev, S. and Kesich, D.: Energy spectrum of isotropic turbulence at large wavenumbers, *CR Acad. Bulg. Sci.*, 22, 627–630, 1969.
- Scheifele, B., Waterman, S., Merckelbach, L., and Carpenter, J. R.: Measuring the Dissipation Rate of Turbulent Kinetic Energy in Strongly Stratified, Low-Energy Environments: A Case Study From the Arctic Ocean, *J. Geophys. Res.-Oceans*, 123, 5459–5480, <https://doi.org/10.1029/2017JC013731>, 2018.
- Schultze, L. K. P., Merckelbach, L. M., and Carpenter, J. R.: Turbulence and Mixing in a Shallow Shelf Sea From Underwater Gliders, *J. Geophys. Res.-Oceans*, 122, 9092–9109, <https://doi.org/10.1002/2017JC012872>, 2017.
- Sousa, A., Madureira, L., Coelho, J., Pinto, J., Pereira, J., Borges Sousa, J., and Dias, P.: LAUV: The Man-Portable Autonomous Underwater Vehicle, *IFAC Proceedings Volumes*, 45, 268–274, <https://doi.org/10.3182/20120410-3-PT-4028.00045>, 2012.
- Spingys, C. P., Garabato, A. C. N., Legg, S., Polzin, K. L., Abrahamsen, E. P., Buckingham, C. E., Forryan, A., and Frajka-Williams, E. E.: Mixing and Transformation in a Deep Western Boundary Current: A Case Study, *J. Phys. Oceanogr.*, 51, 1205–1222, <https://doi.org/10.1175/JPO-D-20-0132.1>, 2021.
- Thorpe, S. A., Osborn, T. R., Jackson, J. F. E., Hall, A. J., and Lueck, R. G.: Measurements of Turbulence in the Upper-Ocean Mixing Layer Using Autosub, *J. Phys. Oceanogr.*, 33, 122–145, [https://doi.org/10.1175/1520-0485\(2003\)033<0122:MOTITU>2.0.CO;2](https://doi.org/10.1175/1520-0485(2003)033<0122:MOTITU>2.0.CO;2), 2003.
- Yamazaki, H. and Osborn, T.: Dissipation estimates for stratified turbulence, *J. Geophys. Res.-Oceans*, 95, 9739–9744, <https://doi.org/10.1029/JC095iC06p09739>, 1990.
- Yamazaki, H., Lueck, R. G., and Osborn, T.: A Comparison of Turbulence Data from a Submarine and a Vertical Profiler, *J. Phys. Oceanogr.*, 20, 1778–1786, [https://doi.org/10.1175/1520-0485\(1990\)020<1778:ACOTDF>2.0.CO;2](https://doi.org/10.1175/1520-0485(1990)020<1778:ACOTDF>2.0.CO;2), 1990.

Paper III

Circulation and hydrography in the northwestern Barents Sea: insights from recent observations and historical data (1950–2022)

Eivind H. Kolås, Till M. Baumann, Ragnheid Skogseth, Zoe Koenig and Ilker Fer
Journal of Geophysical Research: Oceans, in review



Paper IV

The Polar Front in the northwestern Barents Sea: structure, variability and mixing

Eivind H. Kolås, Ilker Fer and Till M. Baumann

Submitted to Ocean Science

IV

Bibliography

- Aagaard, K., Swift, J. H., and Carmack, E. C.: Thermohaline circulation in the Arctic Mediterranean Seas, *Journal of Geophysical Research*, 90, 4833–4846, <https://doi.org/10.1029/jc090ic03p04833>, 1985. 1.1, 2
- Aagaard, K., Foldvik, A., and Hillman, S. R.: The West Spitsbergen Current: Disposition and water mass transformation, *Journal of Geophysical Research*, 92, 3778, <https://doi.org/10.1029/jc092ic04p03778>, 1987. 2.1, 2.1
- Artana, C., Provost, C., Koenig, Z., Athanase, M., and Akgari, A.: Atlantic Water Inflow Through the Yermak Pass Branch: Evolution Since 2007, *Journal of Geophysical Research: Oceans*, 127, e2021JC018006, <https://doi.org/10.1029/2021JC018006>, 2022. 2.1, 2.1
- Atadzhanova, O., Zimin, A., Svergun, E., and Konik, A.: Submesoscale Eddy Structures and Frontal Dynamics in the Barents Sea, *Physical Oceanography*, 25, <https://doi.org/10.22449/1573-160X-2018-3-220-228>, 2018. 2.3
- Athanase, M., Provost, C., Artana, C., Pérez-Hernández, M. D., Sennéchaël, N., Bertosio, C., Garric, G., Lellouche, J.-M., and Prandi, P.: Changes in Atlantic Water Circulation Patterns and Volume Transports North of Svalbard Over the Last 12 Years (20082020), *Journal of Geophysical Research: Oceans*, 126, e2020JC016825, <https://doi.org/10.1029/2020JC016825>, 2021. 2.1, 2.1
- Barton, B. I., Lenn, Y.-D., and Lique, C.: Observed Atlantification of the Barents Sea Causes the Polar Front to Limit the Expansion of Winter Sea Ice, *Journal of Physical Oceanography*, 48, 1849–1866, <https://doi.org/10.1175/JPO-D-18-0003.1>, 2018. 2.2, 2.3
- Baumann, T. M. and Fer, I.: Trapped tidal currents generate freely propagating internal waves at the Arctic continental slope, *Scientific Reports*, 13, <https://doi.org/10.1038/s41598-023-41870-3>, 2023. 1.1
- Beszczynska-Möller, A., Fahrbach, E., Schauer, U., and Hansen, E.: Variability in Atlantic water temperature and transport at the entrance to the Arctic Ocean, 1997-2010, *ICES Journal of Marine Science*, 69, 852–863, <https://doi.org/10.1093/icesjms/fss056>, 2012. 1.1, 2, 2.1, 2.1

- Boyd, T. J. and D'Asaro, E. A.: Cooling of the West Spitsbergen Current: Wintertime Observations West of Svalbard, *Journal of Geophysical Research*, 99, 22 597–22 618, <https://doi.org/10.1029/94jc01824>, 1994. 1.1, 2, 2.1, 2.1, 3.2.6
- Brakstad, A., Gebbie, G., Våge, K., Jeansson, E., and Ólafsdóttir, S. R.: Formation and pathways of dense water in the Nordic Seas based on a regional inversion, *Progress in Oceanography*, 212, 102 981, <https://doi.org/10.1016/j.pocean.2023.102981>, 2023. 1.1
- Bretones, A., Nisancioglu, K. H., Jensen, M. F., Brakstad, A., and Yang, S.: Transient Increase in Arctic Deep-Water Formation and Ocean Circulation under Sea Ice Retreat, *Journal of Climate*, 35, 109–124, <https://doi.org/10.1175/JCLI-D-21-0152.1>, publisher: American Meteorological Society Section: *Journal of Climate*, 2022. 1.1
- Cannaby, H., Ingvaldsen, R., Reigstad, M., Søreide, J., Gerland, S., Ludvigsen, M., and Fransson, A.: Vessel mounted Acoustic Doppler Current Profiler data collected in the Barents Sea and adjacent Arctic Ocean by the Norwegian research icebreaker R/V Kronprins Haakon, during 7 individual surveys conducted for the Nansen Legacy project [Dataset], <https://doi.org/10.21335/NMDC-1175579976>, 2022. 3.1.5
- Carmack, E., Polyakov, I., Padman, L., Fer, I., Hunke, E., Hutchings, J., Jackson, J., Kelley, D., Kwok, R., Layton, C., Melling, H., Perovich, D., Persson, O., Ruddick, B., Timmermans, M.-L., Toole, J., Ross, T., Vavrus, S., and Winsor, P.: Toward Quantifying the Increasing Role of Oceanic Heat in Sea Ice Loss in the New Arctic, *Bulletin of the American Meteorological Society*, 96, 2079–2105, <https://doi.org/10.1175/BAMS-D-13-00177.1>, 2015. 1.1, 2
- Cassano, E. N., Cassano, J. J., Higgins, M. E., and Serreze, M. C.: Atmospheric impacts of an Arctic sea ice minimum as seen in the Community Atmosphere Model, *International Journal of Climatology*, 34, 766–779, <https://doi.org/10.1002/joc.3723>, 2014. 1.1
- Cokelet, E. D., Tervalon, N., and Bellingham, J. G.: Hydrography of the West Spitsbergen Current, Svalbard Branch: Autumn 2001, *Journal of Geophysical Research*, 113, 1–16, <https://doi.org/10.1029/2007jc004150>, 2008. 1.1, 2.1, 2.1, 2.1, 3.2.6
- Crews, L., Sundfjord, A., Albrechtsen, J., and Hattermann, T.: Mesoscale Eddy Activity and Transport in the Atlantic Water Inflow Region North of Svalbard, *Journal of Geophysical Research: Oceans*, 123, 201–215, <https://doi.org/10.1002/2017JC013198>, 2018. 2.1, 2.3
- Crews, L., Sundfjord, A., and Hattermann, T.: How the Yermak Pass Branch regulates Atlantic Water inflow to the Arctic Ocean, *Journal of Geophysical Research: Oceans*, <https://doi.org/10.1029/2018jc014476>, 2019. 2.1, 2.1

- Descôteaux, R., Ershova, E., Wangensteen, O. S., Præbel, K., Renaud, P. E., Cottier, F., and Bluhm, B. A.: Meroplankton Diversity, Seasonality and Life-History Traits Across the Barents Sea Polar Front Revealed by High-Throughput DNA Barcoding, *Frontiers in Marine Science*, 8, <https://doi.org/10.3389/fmars.2021.677732>, 2021. 2.3
- Eriksen, C., Osse, T., Light, R., Wen, T., Lehman, T., Sabin, P., Ballard, J., and Chiodi, A.: Seaglider: a long-range autonomous underwater vehicle for oceanographic research, *IEEE Journal of Oceanic Engineering*, 26, 424–436, <https://doi.org/10.1109/48.972073>, conference Name: IEEE Journal of Oceanic Engineering, 2001. 1.1
- Espinel-Velasco, N., Gawinski, C., Kohlbach, D., Pitusi, V., Graeve, M., and Hop, H.: Interactive effects of ocean acidification and temperature on oxygen uptake rates in *Calanus hyperboreus* nauplii, *Frontiers in Marine Science*, 10, <https://doi.org/https://doi.org/10.3389/fmars.2023.1240673>, 2023. 5.2
- Farrelly, B., Gammelsrød, T., Golmen, L. G., and Sjøberg, B.: Hydrographic conditions in the Fram Strait, summer 1982, *Polar Research*, 3, 227–238, <https://doi.org/10.3402/polar.v3i2.6954>, 1985. 2.1
- Fer, I. and Drinkwater, K.: Mixing in the Barents Sea Polar Front near Hopen in spring, *Journal of Marine Systems*, 130, 206–218, <https://doi.org/10.1016/j.jmarsys.2012.01.005>, 2014. 2.3
- Fer, I., Skogseth, R., and Geyer, F.: Internal Waves and Mixing in the Marginal Ice Zone near the Yermak Plateau, *Journal of Physical Oceanography*, 40, 1613–1630, <https://doi.org/10.1175/2010jpo4371.1>, 2010. 1.1, 2.1
- Fer, I., Peterson, A. K., and Ullgren, J. E.: Microstructure Measurements from an Underwater Glider in the Turbulent Faroe Bank Channel Overflow, *Journal of Atmospheric and Oceanic Technology*, 31, 1128–1150, <https://doi.org/10.1175/JTECH-D-13-00221.1>, 2014. 1.1, 3.1.2, 3.2.8
- Fer, I., Bosse, A., and Dugstad, J.: Norwegian Atlantic Slope Current along the Lofoten Escarpment, *Ocean Science*, 16, 685–701, <https://doi.org/10.5194/os-16-685-2020>, publisher: Copernicus GmbH, 2020a. 2
- Fer, I., Koenig, Z., Kozlov, I. E., Ostrowski, M., Rippeth, T. P., Padman, L., Bosse, A., and Kolås, E.: Tidally Forced Lee Waves Drive Turbulent Mixing Along the Arctic Ocean Margins, *Geophysical Research Letters*, 47, e2020GL088083, <https://doi.org/10.1029/2020GL088083>, 2020b. 2.1
- Fer, I., Baumann, T. M., Elliot, F., and Kolås, E. H.: Ocean microstructure measurements using an MSS profiler during the Nansen Legacy cruise, GOS2020113, October 2020 [Dataset], <https://doi.org/10.21335/NMDC-239170563>, 2023a. 3.1.3, 3.1.4

- Fer, I., Baumann, T. M., Hana, I., Koenig, Z., Randelhoff, A., Rieke, O., and Årvik, A.: Ocean microstructure measurements using an MSS profiler during the Nansen Legacy cruise, KB2022625, October 2022 [Dataset], <https://doi.org/10.21335/NMDC-1169583367>, 2023b. 3.1.3, 3.1.4
- Fer, I., Baumann, T. M., Kalhagen, K., Koenig, Z., and Kolås, E. H.: Ocean microstructure measurements using an MSS profiler during the Nansen Legacy cruise, KH2021702, February 2021 [Dataset], <https://doi.org/10.21335/NMDC-1939445412>, 2023c. 3.1.3, 3.1.4
- Fer, I., Baumann, T. M., Koenig, Z., Randelhoff, A., Rieke, O., Hana, I., and Årvik, A.: Ocean hydrography and current profiles from the Nansen Legacy Process Cruise to the Barents Sea, KB2022625, October 2022 [Dataset], <https://doi.org/10.21335/NMDC-943526062>, 2023d. 3.1.4
- Fer, I., Nilsen, F., Baumann, T. M., Kalhagen, K., Koenig, Z., and Kolås, E. H.: Ocean hydrography and current profiles from the Nansen Legacy Winter Process Cruise to the northern Barents Sea, KH2021702, February 2021 [Dataset], <https://doi.org/https://doi.org/10.21335/NMDC-1544015310>, 2023e. 3.1.4
- Fer, I., Peterson, A. K., and Nilsen, F.: Atlantic Water Boundary Current Along the Southern Yermak Plateau, Arctic Ocean, *Journal of Geophysical Research: Oceans*, 128, e2023JC019645, <https://doi.org/10.1029/2023JC019645>, 2023f. 1.1, 2.1, 2.1
- Fer, I., Skogseth, R., Astad, S., Baumann, T., Elliot, F., Falck, E., Gawinski, C., Kalhagen, K., and Kolås, E.: Ocean hydrography and current profiles from the Nansen Legacy cruise to the northern Barents Sea, GOS2020113, October 2020 [Dataset], <https://doi.org/10.21335/NMDC-1752779505>, 2023g. 3.1.4
- Firing, E. and Ranada, J.: Processing ADCP data with the CODAS software system version 3.1, Joint Institute for Marine and Atmospheric Research, University of Hawaii and National Oceanographic Data Center., Bremerhaven, PANGAEA, 1995. 3.1.5
- Fossum, T. O., Norgren, P., Fer, I., Nilsen, F., Koenig, Z. C., and Ludvigsen, M.: Adaptive Sampling of Surface Fronts in the Arctic Using an Autonomous Underwater Vehicle, *IEEE Journal of Oceanic Engineering*, 46, 1155–1164, <https://doi.org/10.1109/JOE.2021.3070912>, conference Name: IEEE Journal of Oceanic Engineering, 2021. 3.6
- Frajka-Williams, E., Eriksen, C. C., Rhines, P. B., and Harcourt, R. R.: Determining Vertical Water Velocities from Seaglider, *Journal of Atmospheric and Oceanic Technology*, 28, 1641–1656, <https://doi.org/10.1175/2011jtecho830.1>, 2011. 3.1.1
- Frajka-Williams, E., Brearley, J. A., Nash, J. D., and Whalen, C. B.: Chapter 14 - New technological frontiers in ocean mixing, in: *Ocean Mixing*, edited by Meredith, M. and Garabato,

- A. N., pp. 345–361, Elsevier, <https://doi.org/10.1016/B978-0-12-821512-8.00021-9>, 2022. 1.1
- Garau, B., Ruiz, S., Zhang, W. G., Pascual, A., Heslop, E., Kerfoot, J., and Tintoré, J.: Thermal Lag Correction on Slocum CTD Glider Data, *Journal of Atmospheric and Oceanic Technology*, 28, 1065–1071, <https://doi.org/10.1175/jtech-d-10-05030.1>, 2011. 3.1.1
- Gascard, J.-C., Richez, C., and Rouault, C.: New Insights on Large-Scale Oceanography in Fram Strait: The West Spitsbergen Current, in: *Arctic Oceanography: Marginal Ice Zones and Continental Shelves*, pp. 131–182, American Geophysical Union (AGU), <https://doi.org/10.1029/CE049p0131>, 1995. 1.1, 2.1
- Gawarkiewicz, G. and Plueddemann, A. J.: Topographic control of thermohaline frontal structure in the Barents Sea Polar Front on the south flank of Spitsbergen Bank, *Journal of Geophysical Research: Oceans*, 100, 4509–4524, <https://doi.org/10.1029/94JC02427>, 1995. 1.1, 2.2, 2.3
- Gerland, S., Ingvaldsen, R. B., Reigstad, M., Sundfjord, A., Bogstad, B., Chierici, M., Hop, H., Renaud, P. E., Smedsrud, L. H., Stige, L. C., Årthun, M., Berge, J., Bluhm, B. A., Borgå, K., Bratbak, G., Divine, D. V., Eldevik, T., Eriksen, E., Fer, I., Fransson, A., Gradinger, R., Granskog, M. A., Haug, T., Husum, K., Johnsen, G., Jonassen, M. O., Jørgensen, L. L., Kristiansen, S., Larsen, A., Lien, V. S., Lind, S., Lindstrøm, U., Mauritzen, C., Melsom, A., Mernild, S. H., Müller, M., Nilsen, F., Primicerio, R., Søreide, J. E., van der Meeren, G. I., and Wassmann, P.: Still Arctic? The changing Barents Sea, *Elementa: Science of the Anthropocene*, 11, 00088, <https://doi.org/10.1525/elementa.2022.00088>, 2023. 1.1, 2.2
- Goodman, L., Levine, E. R., and Lueck, R. G.: On Measuring the Terms of the Turbulent Kinetic Energy Budget from an AUV, *Journal of Atmospheric and Oceanic Technology*, 23, 977–990, <https://doi.org/10.1175/JTECH1889.1>, 2006. 3.2.8, 4
- Graham, A. G. C., Wählin, A., Hogan, K. A., Nitsche, F. O., Heywood, K. J., Totten, R. L., Smith, J. A., Hillenbrand, C.-D., Simkins, L. M., Anderson, J. B., Wellner, J. S., and Larter, R. D.: Rapid retreat of Thwaites Glacier in the pre-satellite era, *Nature Geoscience*, 15, 706–713, <https://doi.org/10.1038/s41561-022-01019-9>, number: 9 Publisher: Nature Publishing Group, 2022. 1.1
- Grassi, B., Redaelli, G., and Visconti, G.: Arctic Sea Ice Reduction and Extreme Climate Events over the Mediterranean Region, *Journal of Climate*, 26, 10101–10110, <https://doi.org/10.1175/JCLI-D-12-00697.1>, publisher: American Meteorological Society Section: *Journal of Climate*, 2013. 1.1

- Hattermann, T., Isachsen, P. E., von Appen, W.-J., Albrechtsen, J., and Sundfjord, A.: Eddy-driven recirculation of Atlantic Water in Fram Strait, *Geophysical Research Letters*, 43, 3406–3414, <https://doi.org/10.1002/2016gl068323>, 2016. 1.1, 2.1, 2.3
- Helland-Hansen, B. and Nansen, F.: The Norwegian Sea - Its physical oceanography based upon the Norwegian researches 1900-1904, *Rep. on Norw. Fish. and Marin. Invest.*, 11, 360, 1909. 1.1
- Hofmann, Z., von Appen, W.-J., and Wekerle, C.: Seasonal and Mesoscale Variability of the Two Atlantic Water Recirculation Pathways in Fram Strait, *Journal of Geophysical Research: Oceans*, 126, e2020JC017057, <https://doi.org/10.1029/2020JC017057>, 2021. 2.1
- Honda, M., Yamazaki, K., Tachibana, Y., and Takeuchi, K.: Influence of Okhotsk sea-ice extent on atmospheric circulation, *Geophysical Research Letters*, 23, 3595–3598, <https://doi.org/10.1029/96GL03474>, 1996. 1.1
- Ingvaldsen, R. B.: Width of the North Cape Current and location of the Polar Front in the western Barents Sea, *Geophysical Research Letters*, 32, <https://doi.org/10.1029/2005GL023440>, 2005. 2.3
- Ingvaldsen, R. B., Assmann, K. M., Primicerio, R., Fossheim, M., Polyakov, I. V., and Dolgov, A. V.: Physical manifestations and ecological implications of Arctic Atlantification, *Nature Reviews Earth & Environment*, 2, 874–889, <https://doi.org/10.1038/s43017-021-00228-x>, 2021. 1.1, 2.2, 5.2
- IOC, SCOR, and IAPSO: The international thermodynamic equation of seawater 2010: Calculations and use of thermodynamic properties, *Manuals and Guides 56*, Intergovernmental Oceanographic Commission, UNESCO, 2010. 3.1.4, 3.2.6
- Jakobsson, M., Mayer, L. A., Bringensparr, C., Castro, C. F., Mohammad, R., Johnson, P., Ketter, T., Accettella, D., Amblas, D., An, L., Arndt, J. E., Canals, M., Casamor, J. L., Chauché, N., Coakley, B., Danielson, S., Demarte, M., Dickson, M.-L., Dorschel, B., Dowdeswell, J. A., Dreutter, S., Fremand, A. C., Gallant, D., Hall, J. K., Hehemann, L., Hodnesdal, H., Hong, J., Ivaldi, R., Kane, E., Klauke, I., Krawczyk, D. W., Kristoffersen, Y., Kuipers, B. R., Millan, R., Masetti, G., Morlighem, M., Noormets, R., Prescott, M. M., Rebesco, M., Rignot, E., Semiletov, I., Tate, A. J., Travaglini, P., Velicogna, I., Weatherall, P., Weinrebe, W., Willis, J. K., Wood, M., Zarayskaya, Y., Zhang, T., Zimmermann, M., and Zinglensen, K. B.: The International Bathymetric Chart of the Arctic Ocean Version 4.0, *Scientific Data*, 7, 176, <https://doi.org/10.1038/s41597-020-0520-9>, 2020. 3.2.4
- Johannesen, E., Ingvaldsen, R. B., Bogstad, B., Dalpadado, P., Eriksen, E., Gjørseter, H., Knutsen, T., Skern-Mauritzen, M., and Stiansen, J. E.: Changes in Barents Sea ecosystem

- state, 19702009: climate fluctuations, human impact, and trophic interactions, *ICES Journal of Marine Science*, 69, 880–889, <https://doi.org/10.1093/icesjms/fss046>, 2012. 1.1
- Johannessen, O. M. and Foster, L. A.: A note on the topographically controlled Oceanic Polar Front in the Barents Sea, *Journal of Geophysical Research: Oceans*, 83, 4567–4571, <https://doi.org/10.1029/JC083iC09p04567>, 1978. 2.3
- Koenig, Z., Provost, C., Sennéchaël, N., Garric, G., and Gascard, J.-C.: The Yermak Pass Branch: A Major Pathway for the Atlantic Water North of Svalbard?, *Journal of Geophysical Research: Oceans*, 122, 9332–9349, <https://doi.org/10.1002/2017jc013271>, 2017. 1.1, 2.1, 2.1
- Koenig, Z., Fer, I., Kolås, E., Fossum, T. O., Norgren, P., and Ludvigsen, M.: Observations of Turbulence at a Near-Surface Temperature Front in the Arctic Ocean, *Journal of Geophysical Research: Oceans*, 125, e2019JC015 526, <https://doi.org/10.1029/2019JC015526>, 2020. 2.1
- Koenig, Z., Kolås, E. H., and Fer, I.: Structure and drivers of ocean mixing north of Svalbard in summer and fall 2018, *Ocean Science*, 17, 365–381, <https://doi.org/10.5194/os-17-365-2021>, 2021. 2.1
- Koenig, Z., Kalhagen, K., Kolås, E., Fer, I., Nilsen, F., and Cottier, F.: Atlantic Water Properties, Transport and Heat Loss From Mooring Observations North of Svalbard, *Journal of Geophysical Research: Oceans*, 127, e2022JC018 568, <https://doi.org/10.1029/2022JC018568>, 2022. 2.1, 2.1
- Koenig, Z., Fer, I., Chierici, M., Fransson, A., Jones, E., and Kolås, E. H.: Diffusive and advective cross-frontal fluxes of inorganic nutrients and dissolved inorganic carbon in the Barents Sea in autumn, *Progress in Oceanography*, 219, 103 161, <https://doi.org/10.1016/j.pocean.2023.103161>, 2023. 5.2
- Kolås, E. and Fer, I.: Hydrography, transport and mixing of the West Spitsbergen Current: the Svalbard Branch in summer 2015, *Ocean Science*, 14, 1603–1618, <https://doi.org/10.5194/os-14-1603-2018>, 2018. 1.1, 2.1, 2.1
- Kolås, E. and Fer, I.: Physical oceanography data from a Seaglider mission north of Svalbard, late fall 2018 [Dataset], <https://doi.org/10.21335/NMDC-1841837601>, 2020. 3.1.1
- Kolås, E. H., Koenig, Z., Fer, I., Nilsen, F., and Marnela, M.: Structure and Transport of Atlantic Water North of Svalbard From Observations in Summer and Fall 2018, *Journal of Geophysical Research: Oceans*, 125, e2020JC016 174, <https://doi.org/10.1029/2020JC016174>, 2020. 1.1, 3.2.3, 3.2.4, 4.1

- Kolås, E. H., Fer, I., Peterson, A., Brakstad, A., and Elliot, F.: Physical oceanography data from gliders in the Barents Sea, August 2019 - February 2021 [Dataset], <https://doi.org/10.21335/NMDC-381060465>, 2022a. 3.1.1
- Kolås, E. H., Mo-Bjørkelund, T., and Fer, I.: Technical note: Turbulence measurements from a light autonomous underwater vehicle, *Ocean Science*, 18, 389–400, <https://doi.org/10.5194/os-18-389-2022>, 2022b. 3.6
- Kolås, E. H., Baumann, T. M., Skogseth, R., Koenig, Z., and Fer, I.: Western Barents Sea Circulation and Hydrography, past and present, submitted to *Journal of Geophysical Research, Oceans*, <https://doi.org/10.22541/essoar.169203078.81082540/v1>, 2023. 4.2
- Large, W. G. and Pond, S.: Open ocean momentum flux measurements in moderate to strong winds, *Journal of physical oceanography*, 11, 324–336, 1981. 3.1.7
- Lewis, K. M., van Dijken, G. L., and Arrigo, K. R.: Changes in phytoplankton concentration now drive increased Arctic Ocean primary production, *Science*, 369, 198–202, <https://doi.org/10.1126/science.aay8380>, publisher: American Association for the Advancement of Science, 2020. 5.2
- Li, S. and McClimans, T. A.: The effects of winds over a barotropic retrograde slope current, *Continental Shelf Research*, 18, 457–485, [https://doi.org/10.1016/S0278-4343\(97\)00077-0](https://doi.org/10.1016/S0278-4343(97)00077-0), 1998. 2.2
- Lien, V. S., Schlichtholz, P., Skagseth, Ø., and Vikebø, F. B.: Wind-Driven Atlantic Water Flow as a Direct Mode for Reduced Barents Sea Ice Cover, *Journal of Climate*, 30, 803–812, <https://doi.org/10.1175/JCLI-D-16-0025.1>, 2017. 2.3
- Lind, S., Ingvaldsen, R. B., and Furevik, T.: Arctic warming hotspot in the northern Barents Sea linked to declining sea-ice import, *Nature Climate Change*, 8, 634–639, <https://doi.org/10.1038/s41558-018-0205-y>, 2018. 3.2.1
- Loeng, H.: Features of the physical oceanographic conditions of the Barents Sea, *Polar Research*, 10, 5–18, <https://doi.org/10.3402/polar.v10i1.6723>, number: 1, 1991. 1.1, 2.2, 2.3, 3.2.1
- Loeng, H., Ozhigin, V., and Ådlandsvik, B.: Water fluxes through the Barents Sea, *ICES Journal of Marine Science*, 54, 310–317, <https://doi.org/10.1006/jmsc.1996.0165>, 1997. 1.1, 2.2
- Lueck, R. G.: The Statistics of Oceanic Turbulence Measurements. Part I: Shear Variance and Dissipation Rates, *Journal of Atmospheric and Oceanic Technology*, 39, 1259–1271, <https://doi.org/10.1175/JTECH-D-21-0051.1>, 2022. 3.2.8

- Lueck, R. G., Wolk, F., and Yamazaki, H.: Oceanic Velocity Microstructure Measurements in the 20th Century, *Journal of Oceanography*, 58, 153–174, <https://doi.org/10.1023/A:1015837020019>, 2002. 3.2.8, 3.2.8
- Lundesgaard, Ø., Sundfjord, A., Lind, S., Nilsen, F., and Renner, A. H. H.: Import of Atlantic Water and sea ice controls the ocean environment in the northern Barents Sea, *Ocean Science*, 18, 1389–1418, <https://doi.org/10.5194/os-18-1389-2022>, publisher: Copernicus GmbH, 2022. 4
- Manley, T. O.: Branching of Atlantic Water within the Greenland-Spitsbergen Passage: An estimate of recirculation, *Journal of Geophysical Research*, 100, 20 627, <https://doi.org/10.1029/95jc01251>, 1995. 2.1, 2.1
- Marnela, M., Rudels, B., Houssais, M.-N., Beszczynska-Möller, A., and Eriksson, P. B.: Recirculation in the Fram Strait and transports of water in and north of the Fram Strait derived from CTD data, *Ocean Science*, 9, 499–519, <https://doi.org/10.5194/os-9-499-2013>, 2013. 2.1, 2.1
- McDougall, T. J.: Potential Enthalpy: A Conservative Oceanic Variable for Evaluating Heat Content and Heat Fluxes, *Journal of Physical Oceanography*, 33, 945–963, [https://doi.org/10.1175/1520-0485\(2003\)033<0945:PEACOV>2.0.CO;2](https://doi.org/10.1175/1520-0485(2003)033<0945:PEACOV>2.0.CO;2), publisher: American Meteorological Society, 2003. 3.2.6
- McDougall, T. J. and Barker, P. M.: Getting started with TEOS-10 and the Gibbs Seawater (GSW) Oceanographic Toolbox, 2011. 3.1.4, 3.2.4
- McPhail, S., Templeton, R., Pebody, M., Roper, D., and Morrison, R.: Autosub Long Range AUV Missions Under the Filchner and Ronne Ice Shelves in the Weddell Sea, Antarctica - an Engineering Perspective, in: OCEANS 2019 - Marseille, pp. 1–8, <https://doi.org/10.1109/OCEANSE.2019.8867206>, 2019. 1.1
- McWilliams, J. C.: The Nature and Consequences of Oceanic Eddies, in: Ocean Modeling in an Eddying Regime, pp. 5–15, American Geophysical Union (AGU), <https://doi.org/10.1029/177GM03>, 2008. 2.3
- Meincke, J., Rudels, B., and Friedrich, H. J.: The Arctic OceanNordic Seas thermohaline system, *ICES Journal of Marine Science*, 54, 283–299, <https://doi.org/10.1006/jmsc.1997.0229>, 1997. 1.1
- Menze, S., Ingvaldsen, R. B., Haugan, P., Fer, I., Sundfjord, A., Beszczynska-Moeller, A., and Falk-Petersen, S.: Atlantic Water Pathways Along the North-Western Svalbard Shelf Mapped Using Vessel-Mounted Current Profilers, *Journal of Geophysical Research: Oceans*, 124, 1699–1716, <https://doi.org/10.1029/2018jc014299>, 2019. 2.1

- Meyer, A., Fer, I., Sundfjord, A., and Peterson, A. K.: Mixing rates and vertical heat fluxes north of Svalbard from Arctic winter to spring, *Journal of Geophysical Research: Oceans*, 122, 4569–4586, <https://doi.org/10.1002/2016jc012441>, 2017a. 2.1
- Meyer, A., Sundfjord, A., Fer, I., Provost, C., Robineau, N. V., Koenig, Z., Onarheim, I. H., Smedsrud, L. H., Duarte, P., Dodd, P. A., Graham, R. M., Schmidtko, S., and Kauko, H. M.: Winter to summer oceanographic observations in the Arctic Ocean north of Svalbard, *Journal of Geophysical Research: Oceans*, 122, 6218–6237, <https://doi.org/10.1002/2016jc012391>, 2017b. 2.1
- Midttun, L.: Formation of dense bottom water in the Barents Sea, *Deep Sea Research Part A. Oceanographic Research Papers*, 32, 1233–1241, [https://doi.org/10.1016/0198-0149\(85\)90006-8](https://doi.org/10.1016/0198-0149(85)90006-8), 1985. 1.1
- Mohamed, B., Nilsen, F., and Skogseth, R.: Interannual and Decadal Variability of Sea Surface Temperature and Sea Ice Concentration in the Barents Sea, *Remote Sensing*, 14, 4413, <https://doi.org/10.3390/rs14174413>, 2022. 1.1, 2.2
- Mori, M., Watanabe, M., Shiogama, H., Inoue, J., and Kimoto, M.: Robust Arctic sea-ice influence on the frequent Eurasian cold winters in past decades, *Nature Geoscience*, 7, 869–873, <https://doi.org/10.1038/ngeo2277>, number: 12 Publisher: Nature Publishing Group, 2014. 1.1
- Nasmyth, P. W.: Oceanic turbulence, Ph.D. thesis, University of British Columbia, <https://doi.org/10.14288/1.0302459>, 1970. 3.2.8
- Nilsen, F., Ersdal, E. A., and Skogseth, R.: Wind-Driven Variability in the Spitsbergen Polar Current and the Svalbard Branch Across the Yermak Plateau, *Journal of Geophysical Research: Oceans*, 126, e2020JC016734, <https://doi.org/10.1029/2020JC016734>, 2021. 2.1
- Onarheim, I. H., Smedsrud, L. H., Ingvaldsen, R. B., and Nilsen, F.: Loss of sea ice during winter north of Svalbard, *Tellus A: Dynamic Meteorology and Oceanography*, 66, 23 933–23 941, <https://doi.org/10.3402/tellusa.v66.23933>, 2014. 1.1, 2.1
- Onarheim, I. H. and Årthun, M.: Toward an ice-free Barents Sea, *Geophysical Research Letters*, 44, 8387–8395, <https://doi.org/10.1002/2017GL074304>, 2017. 1.1
- Orvik, K. A.: Long-Term Moored Current and Temperature Measurements of the Atlantic Inflow Into the Nordic Seas in the Norwegian Atlantic Current; 19952020, *Geophysical Research Letters*, 49, e2021GL096427, <https://doi.org/10.1029/2021GL096427>, 2022. 2
- Orvik, K. A. and Niiler, P.: Major pathways of Atlantic water in the northern North Atlantic and Nordic Seas toward Arctic, *Geophysical Research Letters*, 29, 2–1–2–4, <https://doi.org/10.1029/2002GL015002>, 2002. 2

- Oziel, L., Sirven, J., and Gascard, J.-C.: The Barents Sea frontal zones and water masses variability (19802011), *Ocean Science*, 12, 169–184, <https://doi.org/10.5194/os-12-169-2016>, 2016. 1.1, 2.2, 2.3, 3.2.7
- Padman, L. and Erofeeva, S.: A barotropic inverse tidal model for the Arctic Ocean, *Geophysical Research Letters*, 31, <https://doi.org/10.1029/2003gl019003>, 2004. 3.2.2
- Parsons, A. R., Bourke, R. H., Muench, R. D., Chiu, C.-S., Lynch, J. F., Miller, J. H., Plueddemann, A. J., and Pawlowicz, R.: The Barents Sea Polar Front in summer, *Journal of Geophysical Research: Oceans*, 101, 14 201–14 221, <https://doi.org/10.1029/96JC00119>, 1996. 2.2, 2.3
- Perkin, R. G. and Lewis, E. L.: Mixing in the West Spitsbergen Current, *Journal of Physical Oceanography*, 14, 1315–1325, [https://doi.org/10.1175/1520-0485\(1984\)014<1315:mitwsc>2.0.co;2](https://doi.org/10.1175/1520-0485(1984)014<1315:mitwsc>2.0.co;2), 1984. 2.1, 2.1
- Pickart, R. S. and Smethie, W. M.: Temporal evolution of the deep western boundary current where it enters the sub-tropical domain, *Deep Sea Research Part I: Oceanographic Research Papers*, 45, 1053–1083, [https://doi.org/10.1016/s0967-0637\(97\)00084-8](https://doi.org/10.1016/s0967-0637(97)00084-8), 1998. 3.2.4
- Polyakov, I. V., Pnyushkov, A. V., Alkire, M. B., Ashik, I. M., Baumann, T. M., Carmack, E. C., Goszczko, I., Guthrie, J., Ivanov, V. V., Kanzow, T., Krishfield, R., Kwok, R., Sundfjord, A., Morison, J., Rember, R., and Yulin, A.: Greater role for Atlantic inflows on sea-ice loss in the Eurasian Basin of the Arctic Ocean, *Science*, 356, 285–291, <https://doi.org/10.1126/science.aai8204>, 2017. 1.1, 2
- Polyakov, I. V., Ingvaldsen, R. B., Pnyushkov, A. V., Bhatt, U. S., Francis, J. A., Janout, M., Kwok, R., and Skagseth, Ø.: Fluctuating Atlantic inflows modulate Arctic atlantification, *Science*, 381, 972–979, <https://doi.org/10.1126/science.adh5158>, publisher: American Association for the Advancement of Science, 2023. 1.1, 2
- Porter, M., Henley, S. F., Orkney, A., Bouman, H. A., Hwang, B., Dumont, E., Venables, E. J., and Cottier, F.: A Polar Surface Eddy Obscured by Thermal Stratification, *Geophysical Research Letters*, 47, e2019GL086 281, <https://doi.org/10.1029/2019GL086281>, 2020. 2.3
- Pérez-Hernández, M. D., Pickart, R. S., Pavlov, V., Våge, K., Ingvaldsen, R., Sundfjord, A., Renner, A. H. H., Torres, D. J., and Erofeeva, S. Y.: The Atlantic Water boundary current north of Svalbard in late summer, *Journal of Geophysical Research: Oceans*, 122, 2269–2290, <https://doi.org/10.1002/2016jc012486>, 2017. 1.1, 2.1, 2.1, 2.1
- Pérez-Hernández, M. D., Pickart, R. S., Torres, D. J., Bahr, F., Sundfjord, A., Ingvaldsen, R., Renner, A. H. H., Beszczynska-Möller, A., von Appen, W.-J., and Pavlov, V.: Structure, transport and seasonality of the Atlantic Water Boundary Current north of Svalbard: Results

- from a year-long mooring array, *Journal of Geophysical Research: Oceans*, <https://doi.org/10.1029/2018jc014759>, 2019. 1.1, 2.1, 2.1
- Quadfasel, D., Rudels, B., and Kurz, K.: Outflow of dense water from a Svalbard fjord into the Fram Strait, *Deep Sea Research Part A. Oceanographic Research Papers*, 35, 1143–1150, [https://doi.org/10.1016/0198-0149\(88\)90006-4](https://doi.org/10.1016/0198-0149(88)90006-4), 1988. 1.1
- Reigstad, M., Wassmann, P., Wexels Riser, C., Øygarden, S., and Rey, F.: Variations in hydrography, nutrients and chlorophyll a in the marginal ice-zone and the central Barents Sea, *Journal of Marine Systems*, 38, 9–29, [https://doi.org/10.1016/S0924-7963\(02\)00167-7](https://doi.org/10.1016/S0924-7963(02)00167-7), 2002. 1.1
- Reistad, M., Breivik, Ø., Haakenstad, H., Aarnes, O. J., Furevik, B. R., and Bidlot, J.-R.: A high-resolution hindcast of wind and waves for the North Sea, the Norwegian Sea, and the Barents Sea, *Journal of Geophysical Research*, 116, <https://doi.org/10.1029/2010jc006402>, 2011. 3.1.7
- Rodionov, V. B.: On the mesoscale structure of the frontal zones in the Nordic seas, *Journal of Marine Systems*, 3, 127–139, [https://doi.org/10.1016/0924-7963\(92\)90034-6](https://doi.org/10.1016/0924-7963(92)90034-6), 1992. 2.3
- Rudels, B., Muench, R. D., Gunn, J., Schauer, U., and Friedrich, H. J.: Evolution of the Arctic Ocean boundary current north of the Siberian shelves, *Journal of Marine Systems*, 25, 77–99, [https://doi.org/10.1016/S0924-7963\(00\)00009-9](https://doi.org/10.1016/S0924-7963(00)00009-9), 2000. 2.1
- Rudels, B., Björk, G., Nilsson, J., Winsor, P., Lake, I., and Nohr, C.: The interaction between waters from the Arctic Ocean and the Nordic Seas north of Fram Strait and along the East Greenland Current: results from the Arctic Ocean-02 Oden expedition, *Journal of Marine Systems*, 55, 1–30, <https://doi.org/10.1016/j.jmarsys.2004.06.008>, 2005. 3.2.1
- Rudels, B., Korhonen, M., Schauer, U., Pisarev, S., Rabe, B., and Wisotzki, A.: Circulation and transformation of Atlantic water in the Eurasian Basin and the contribution of the Fram Strait inflow branch to the Arctic Ocean heat budget, *Progress in Oceanography*, 132, 128–152, <https://doi.org/10.1016/j.pocean.2014.04.003>, 2015. 2
- Saloranta, T. M. and Haugan, P. M.: Northward cooling and freshening of the warm core of the West Spitsbergen Current, *Polar Research*, 23, 79–88, <https://doi.org/10.1111/j.1751-8369.2004.tb00131.x>, 2004. 2.1, 2.1
- Schauer, U. and Beszczynska-Möller, A.: Problems with estimation and interpretation of oceanic heat transport – conceptual remarks for the case of Fram Strait in the Arctic Ocean, *Ocean Science*, 5, 487–494, <https://doi.org/10.5194/os-5-487-2009>, 2009. 3.2.6
- Schlichtholz, P. and Houssais, M.-N.: An overview of the beta - S correlations in Fram Strait based on the MIZEX 84 data, *Oceanologia*, 44, 243–272, 2002. 3.2.1, 3.2

- Schofield, O., Kohut, J., Aragon, D., Creed, L., Graver, J., Haldeman, C., Kerfoot, J., Roarty, H., Jones, C., Webb, D., and Glenn, S.: Slocum Gliders: Robust and ready, *Journal of Field Robotics*, 24, 473–485, <https://doi.org/10.1002/rob.20200>, 2007. 1.1
- Seaglider: Seaglider Quality Control Manual, Tech. rep., School of Oceanography and Applied Physics Laboratory University of Washington, 2012. 3.1.1
- Sirevaag, A. and Fer, I.: Early Spring Oceanic Heat Fluxes and Mixing Observed from Drift Stations North of Svalbard, *Journal of Physical Oceanography*, 39, 3049–3069, <https://doi.org/10.1175/2009jpo4172.1>, 2009. 2.1
- Skagseth, Ø.: Recirculation of Atlantic Water in the western Barents Sea, *Geophysical Research Letters*, 35, <https://doi.org/10.1029/2008GL033785>, 2008. 2.2
- Skagseth, Ø., Furevik, T., Ingvaldsen, R., Loeng, H., Mork, K. A., Orvik, K. A., and Ozhigin, V.: Volume and Heat Transports to the Arctic Ocean Via the Norwegian and Barents Seas, in: *ArcticSubarctic Ocean Fluxes: Defining the Role of the Northern Seas in Climate*, edited by Dickson, R. R., Meincke, J., and Rhines, P., pp. 45–64, Springer Netherlands, Dordrecht, https://doi.org/10.1007/978-1-4020-6774-7_3, 2008. 1.1, 2.2
- Skagseth, Ø., Eldevik, T., Årthun, M., Asbjørnsen, H., Lien, V. S., and Smedsrud, L. H.: Reduced efficiency of the Barents Sea cooling machine, *Nature Climate Change*, 10, 661–666, <https://doi.org/10.1038/s41558-020-0772-6>, 2020. 2.3
- Skogseth, R., Ellingsen, P., Berge, J., Cottier, F., Falk-Petersen, S., Ivanov, B., Nilsen, F., Søreide, J., and Vader, A.: UNIS hydrographic database, Norwegian Polar Institute, <https://doi.org/10.21334/unis-hydrography>, 2019. 3.1.6
- Smedsrud, L. H., Ingvaldsen, R., Nilsen, J. E. Ø., and Skagseth, Ø.: Heat in the Barents Sea: transport, storage, and surface fluxes, *Ocean Science*, 6, 219–234, <https://doi.org/10.5194/os-6-219-2010>, 2010. 1.1, 2.2
- Smith, W. H. F. and Wessel, P.: Gridding with continuous curvature splines in tension, *GEOPHYSICS*, 55, 293–305, <https://doi.org/10.1190/1.1442837>, 1990. 3.2.4
- Sousa, A., Madureira, L., Coelho, J., Pinto, J., Pereira, J., Borges Sousa, J., and Dias, P.: LAUV: The Man-Portable Autonomous Underwater Vehicle, *IFAC Proceedings Volumes*, 45, 268–274, <https://doi.org/10.3182/20120410-3-PT-4028.00045>, 2012. 3.1.1
- Sundfjord, A., Fer, I., Kasajima, Y., and Svendsen, H.: Observations of turbulent mixing and hydrography in the marginal ice zone of the Barents Sea, *Journal of Geophysical Research: Oceans*, 112, <https://doi.org/10.1029/2006JC003524>, 2007. 2.3

- Sundfjord, A., Assmann, K. M., Lundesgaard, Ø., Renner, A. H. H., Lind, S., and Ingvaldsen, R. B.: Suggested water mass definitions for the central and northern Barents Sea, and the adjacent Nansen Basin: Workshop Report, The Nansen Legacy Report Series, 8, <https://doi.org/10.7557/nlrs.5707>, 2020. 3.2.1, 3.2
- Swift, J. H. and Aagaard, K.: Seasonal transitions and water mass formation in the Iceland and Greenland seas, *Deep Sea Research Part A. Oceanographic Research Papers*, 28, 1107–1129, [https://doi.org/10.1016/0198-0149\(81\)90050-9](https://doi.org/10.1016/0198-0149(81)90050-9), 1981. 3.2.1, 3.2
- Testor, P., de Young, B., Rudnick, D. L., Glenn, S., Hayes, D., Lee, C. M., Pattiaratchi, C., Hill, K., Heslop, E., Turpin, V., Alenius, P., Barrera, C., Barth, J. A., Beaird, N., Bécu, G., Bosse, A., Bourrin, F., Brearley, J. A., Chao, Y., Chen, S., Chiggiato, J., Coppola, L., Crout, R., Cummings, J., Curry, B., Curry, R., Davis, R., Desai, K., DiMarco, S., Edwards, C., Fielding, S., Fer, I., Frajka-Williams, E., Gildor, H., Goni, G., Gutierrez, D., Haugan, P., Hebert, D., Heiderich, J., Henson, S., Heywood, K., Hogan, P., Houpert, L., Huh, S., E. Inall, M., Ishii, M., Ito, S.-i., Itoh, S., Jan, S., Kaiser, J., Karstensen, J., Kirkpatrick, B., Klymak, J., Kohut, J., Krahnmann, G., Krug, M., McClatchie, S., Marin, F., Mauri, E., Mehra, A., P. Meredith, M., Meunier, T., Miles, T., Morell, J. M., Mortier, L., Nicholson, S., O’Callaghan, J., O’Conchubhair, D., Oke, P., Pallàs-Sanz, E., Palmer, M., Park, J., Perivoliotis, L., Poulain, P.-M., Perry, R., Queste, B., Rainville, L., Rehm, E., Roughan, M., Rome, N., Ross, T., Ruiz, S., Saba, G., Schaeffer, A., Schönau, M., Schroeder, K., Shimizu, Y., Sloyan, B. M., Smeed, D., Snowden, D., Song, Y., Swart, S., Tenreiro, M., Thompson, A., Tintore, J., Todd, R. E., Toro, C., Venables, H., Wagawa, T., Waterman, S., Watlington, R. A., and Wilson, D.: OceanGliders: A Component of the Integrated GOOS, *Frontiers in Marine Science*, 6, <https://doi.org/10.3389/fmars.2019.00422>, 2019. 1.1
- Timmermans, M.-L. and Marshall, J.: Understanding Arctic Ocean Circulation: A Review of Ocean Dynamics in a Changing Climate, *Journal of Geophysical Research: Oceans*, 125, e2018JC014378, <https://doi.org/10.1029/2018JC014378>, 2020. 1.1
- Troupin, C., Beltran, J. P., Heslop, E., Torner, M., Garau, B., Allen, J., Ruiz, S., and Tintoré, J.: A toolbox for glider data processing and management, *Methods in Oceanography*, 13-14, 13–23, <https://doi.org/10.1016/j.mio.2016.01.001>, 2015. 3.1.1
- Uppala, S., Kållberg, P., Simmons, A., Andreae, U., Da Costa Bechtold, V., Fiorino, M., Gibson, J., Haseler, J., Hernandez, A., Kelly, G., Li, X., Onogi, K., Saarinen, S., Sokka, N., Allan, R., Andersson, E., Arpe, K., Balmaseda, M., Van Der Berg, L., Beljaars, A., Bidlot, J., Bormann, N., Caires, S., Chevallier, F., Dethof, A., Dragosavac, M., Fisher, M., Fuentes, M., Hagemann, Hoskins, B., Isaksen, L., Janssen, P., Jenne, R., McNally, A., Mahfouf, J.-F., Morcrette, J.-J., Rayner, N., Saunders, R., Simon, P., Sterl, A., Trenberth, K., Untch, A., Vasiljevic, D., Viterbo, P., and Woolen, J.: The ERA-40 re-analysis, *Quarterly*

- Journal of the Royal Meteorological Society: A journal of the atmospheric sciences, applied meteorology and physical oceanography, 131, 2961–3012, 2005. 3.1.7
- Vihma, T., Pirazzini, R., Fer, I., Renfrew, I. A., Sedlar, J., Tjernström, M., Lüpkes, C., Nygård, T., Notz, D., Weiss, J., Marsan, D., Cheng, B., Birnbaum, G., Gerland, S., Chechin, D., and Gascard, J. C.: Advances in understanding and parameterization of small-scale physical processes in the marine Arctic climate system: a review, *Atmospheric Chemistry and Physics*, 14, 9403–9450, <https://doi.org/10.5194/acp-14-9403-2014>, 2014. 2
- Visbeck, M.: Deep Velocity Profiling Using Lowered Acoustic Doppler Current Profilers: Bottom Track and Inverse Solutions, *Journal of Atmospheric and Oceanic Technology*, 19, 794–807, [https://doi.org/10.1175/1520-0426\(2002\)019<0794:dvpula>2.0.co;2](https://doi.org/10.1175/1520-0426(2002)019<0794:dvpula>2.0.co;2), 2002. 3.1.5
- von Appen, W.-J., Schauer, U., Hattermann, T., and Beszczynska-Möller, A.: Seasonal Cycle of Mesoscale Instability of the West Spitsbergen Current, *Journal of Physical Oceanography*, 46, 1231–1254, <https://doi.org/10.1175/jpo-d-15-0184.1>, 2016. 2.1, 2.3
- von Appen, W.-J., Baumann, T. M., Janout, M., Koldunov, N., Lenn, Y.-D., Pickart, R. S., Scott, R. B., and Wang, Q.: Eddies and the Distribution of Eddy Kinetic Energy in the Arctic Ocean, *Oceanography*, 35, 42–51, URL <https://www.jstor.org/stable/27182695>, publisher: Oceanography Society, 2022. 1.1
- Våge, K., Pickart, R. S., Pavlov, V., Lin, P., Torres, D. J., Ingvaldsen, R., Sundfjord, A., and Proshutinsky, A.: The Atlantic Water boundary current in the Nansen Basin: Transport and mechanisms of lateral exchange, *Journal of Geophysical Research: Oceans*, 121, 6946–6960, <https://doi.org/10.1002/2016jc011715>, 2016. 1.1, 2.1, 2.1, 2.1, 2.3
- Våge, S., Basedow, S. L., Tande, K. S., and Zhou, M.: Physical structure of the Barents Sea Polar Front near Storbanken in August 2007, *Journal of Marine Systems*, 130, 256–262, <https://doi.org/10.1016/j.jmarsys.2011.11.019>, 2014. 2.2, 2.3
- Walczowski, W.: Frontal structures in the West Spitsbergen Current margins, *Ocean Science*, 9, 957–975, <https://doi.org/10.5194/os-9-957-2013>, publisher: Copernicus GmbH, 2013. 2.1
- Årthun, M., Ingvaldsen, R., Smedsrud, L., and Schrum, C.: Dense water formation and circulation in the Barents Sea, *Deep Sea Research Part I: Oceanographic Research Papers*, 58, 801–817, <https://doi.org/10.1016/j.dsr.2011.06.001>, 2011. 1.1, 2.3
- Årthun, M., Eldevik, T., Smedsrud, L. H., Skagseth, Ø., and Ingvaldsen, R. B.: Quantifying the Influence of Atlantic Heat on Barents Sea Ice Variability and Retreat, *Journal of Climate*, 25, 4736–4743, <https://doi.org/10.1175/JCLI-D-11-00466.1>, 2012. 1.1, 2.2



Graphic design: Communication Division, UIB / Print: Skjipes Kommunikasjon AS



uib.no

ISBN: 9788230847282 (print)
9788230867976 (PDF)